The Hong Kong Polytechnic University

Department of Electrical Engineering

Advanced Fibre Bragg Grating and Microfibre Bragg Grating Fabrication Techniques

CHUNG KIT MAN

A thesis submitted in partial fulfillment of the requirements for the degree of Doctor of Philosophy

March 2012

CERTIFICATE OF ORIGINALITY

I hereby declare that this thesis is my own work and that, to the best of my knowledge and belief, it reproduces no material previously published or written nor material which has been accepted for the award of any other degree or diploma, except where due acknowledgement has been made in the text.

(Signed)______________________________

(Name of student)___CHUNG KIT MAN_____

Abstract

Fibre Bragg gratings (FBGs) have become a very important technology for communication systems and fibre optic sensing. Typically, FBGs are less than 10-mm long and are fabricated using fused silica uniform phase masks which become more expensive for longer length or non-uniform pitch. Generally, interference UV laser beams are employed to make long or complex FBGs, and this technique introduces critical precision and control issues. The fabrications of advanced gratings with complex designs and in new type of optical fibres are challenging research topics. The availability of long complex gratings paves a way for meeting the needs of demanding applications such as gratings employed for dispersion-compensation of high bit-rate transmission.

In this work, we demonstrate an advanced fibre Bragg grating fabrication system that enables the writing of long complex gratings in optical fibres with virtually any apodisation profile, local phase and Bragg wavelength using a novel optical design in which the incident angles of two UV beams onto an optical fibre can be adjusted simultaneously by moving just one optical components, instead of two optics employed in earlier configurations, to vary the grating pitch. The operation principle is based on the translate-and-write method which used a high-precision translation stage to move the interference beams along the length of an optical fibre to realize long gratings in a well-controlled environment. The key advantage of the grating fabrication system is that different kinds of complex gratings can be fabricated by controlling the linear movements of two translation stages. A 90-mm

long uniform grating and 50-mm long chirped FBG with chirp rate of 0.15-nm/mm using the non-chirped phase mask are demonstrated.

In addition to the study of advanced grating fabrication technique, we also focus on the inscription of fibre Bragg gratings written in optical fibres with a cladding diameter of several ten's of microns. Fabrication of microfibres was investigated using sophisticated tapering method. We also proposed a simple but practical technique to filter out the higher order modes reflected from the FBG written in microfibres via a linear taper region while the fundamental mode re-couples to the core. By using this technique, reflection from the microfibre Bragg grating (MFBG) can be effectively single mode, simplifying the demultiplexing and demodulation processes. We demonstrate that effectively a single reflection peak is obtained from an FBG written in multi-mode microfiber.

The characteristics of MFBG are investigated. MFBG exhibits high sensitivity to contact force and an MFBG-based force sensor was also constructed and tested to investigate their suitability for use as an invasive surgery device. Performance of the MFBG based contact force sensor packaged in a conforming elastomer material compares favourably to one of the best-performing commercial contact force sensors in catheterization applications. The proposed sensor features extremely high sensitivity up to 1.37-mN, miniature size (2.4-mm) that meets standard specification, excellent linearity, low hysteresis, and magnetic resonance imaging compatibility.

Acknowledgments

I am deeply indebted to my mother, Lam Kai Ying and wish to express my thanks for supporting me throughout all my studies at University.

I offer my sincerest gratitude to my supervisor, Prof. Hwa-Yaw Tam, who has supported me throughout my Ph.D. student with his patience and knowledge while allowing me the room to work in my own way.

I would like to show my gratitude to my colleagues and note especially Prof. Chao Lu, Mr. Zhengyong Liu and Dr. Ming-Leung Vincent for their kindly collaborations, Dr. Alan Pak Tao Lau, Dr. Shun Yee Michael Liu, for their valuable discussion and suggestion.

Finally, I greatly appreciate the financial support of the entire project from the Research Grants Council of the Hong Kong SAR Government.

Table of Contents

Chapter 1

Introduction

1.1 Motivation and Contribution

In 2009, Prof. Charles K. Kao was awarded half of Novel Prize in Physics for the groundbreaking achievements concerning the transmission of light in optical fibre for communication. Optical fibre has been regarded as one of the most important invention in this century and has revolutionized telecommunication since it was developed. The success of the Internet is based on the tremendous fast data transmission over the use of optical fibre. Optical fibre has a great deal of advantages, including small size and weight, low transmission loss, enormous bandwidths, immunity to cross talk, electrical isolation, signal security, ruggedness and flexibility, low cost, and reliability. The many unique features of optical fibres lead to the fact that they are not limited to telecommunications and their application extends to many other areas. Optical fibre sensing is one of the fields that optical fibre has revolutionised.

Optical fibre sensors are broadly classified into extrinsic and intrinsic sensors. Optical sensors based on Fibre Bragg grating (FBG) are intrinsic. FBGs can reflect a particular wavelength and transmit the rest. The reflected wavelength can be used as sensing measurands.

FBGs are being employed successfully in a wide range of applications. The fabrication of fibre Bragg gratings that features high flexible grating profile designs and microfibre Bragg gratings are two interesting research topics that have the potential to enhance the capability of FBG sensors. In this project, a novel fibre Bragg gratings fabrication system with the capability to write long, chirped, apodised and phase shifted grating was proposed and demonstrated experimentally. Successful fabrication of FBGs in microfibre was also demonstrated. The characterisations of micrfibre Bragg gratings and their potential use in contact force sensing application for catheters were also investigated in this project.

The main contributions of this project may be summarized as follows:

1. A novel practical fiber Bragg grating (FBG) fabrication setup was demonstrated. With high performance linear stages, piezoelectric translation (PZT) stages, and a highly stable continuous wave laser, the FBG fabrication system enables writing of long FBGs by a continuous translate–and-write process and allows implementation of arbitrary chirp and apodization. A key innovation is that the local Bragg wavelength is controlled by a simple movement of the phase mask by a PZT in the direction perpendicular to its surface. The focus position of the two writing beams is not changed during the Bragg wavelength change, an intrinsic feature of the design, ensuring simplicity, robustness and stability. Apodization can be achieved by vibrating the phase mask in the direction parallel to its surface by a PZT. Phase steps can also be inserted in FBGs at any desired location by stepping the same PZT. An isolated environment was built to ensure minimum wind current and temperature variation during the long FBG writing time. A long uniform FBG and a linearly chirped FBG are written to demonstrate the performance of the setup.

2. Fabrication of small-diameter optical fibres using a glass-processing machine from Vytran. Optical fibres with diameters from about 1 micron to 50 microns were successfully fabricated. A novel technique to obtain effectively single mode in reflection from a fiber Bragg grating (FBG) written in multi-mode microfibers. The capability of designing FBG in microfibers reflecting just the fundamental mode instead of multiple modes, simplifying demultiplexing and demodulation, is highly desirable. It was demonstrated that the taper length of a microfiber can be effectively used to control the mode re-coupling conditions. The reflection spectra from FBGs written in microfibers with different lengths are investigated.
3. Characterisation of Microfiber Bragg gratings (MFBGs). Recent sensing applications exploiting various features including sensitivity of ambient refractive index, strain and force/tension, and temperature were reviewed.
4. Fabrication and characterisation of a novel miniaturized highly sensitive contact force sensor based on a MFBG embedded in a comforting elastomer material. The sensor features extremely high sensitivity of 1.37-mN and excellent linearity up to contact force of 0.65-N. The performance meets all the essential specifications as minimally invasive surgery devices for catheter application. In addition, the sensor is easy to fabricate and thus potentially low-cost.

1.2 Thesis outline

This thesis documents the research work that was performed during the study of advanced fibre Bragg gratings fabrication and microfibre Bragg gratings for sensing applications. The works to be described in this thesis are organized as follows:

In chapter 2, an overview of fibre Bragg gratings is reviewed. The photosensitivity, theory and fabrication techniques are covered.

In chapter 3, the work on the advanced fibre Bragg gratings fabrication system is reported. The working principle, software control, writing environment isolation, optical alignments and experiment results are covered.

In chapter 4, microfiber is introduced. The grating written in the microfibre will also be described. In addition, a simple but effective technique that retrieve single mode in reflection from a multi-mode microfibre Bragg grating is demonstrated.

In chapter 5, the sensitivities to the ambient refractive index, temperature, tension and strain of the microfibre Bragg gratings are studied. The strain distribution of the microfibre in different portions is also analysed.

In chapter 6, a highly sensitive compact contact force sensor based on microfibre Bragg grating for minimally invasive surgery application is proposed. The performances comparing with the ideal specification and one of the best-performed commercial contact force sensors for the catheter application are measured.

Finally, chapter 7 draws the conclusions and gives some directions for further research work on the subject.

1.3 Publications Arose from the Project

The publications arose within the period of the research study for the degree of Ph.D. include:

Journal articles:

[1] **K. M. Chung**, L. Dong, C. Lu, and H. Y. Tam, “Novel fiber Bragg grating fabrication system for long gratings with independent apodisation and with local phase and wavelength control,” *Optics Express*, vol. 19, no. 13, pp. 12664–12672, 2011.

[2] M. L. V. Tse, **K. M. Chung**, L. Dong, B.K. Thomas, L.B. Fu, K.C.D. Cheng, C. Lu, and H.Y. Tam, “Observation of symmetrical reflection sidebands in a silica suspended-core fiber Bragg grating,” *Optics Express*, vol. 18, no. 16, pp. 17373–17381, Aug. 2010.

[3] **K.M. Chung**, Z. Liu, C. Lu, H.-Y Tam, “Highly sensitive compact force sensor based on microfiber Bragg grating,” *IEEE Photonics Technology lett.,* vol. 24, no. 8, pp. 700-702, Apr. 2012.

[4] **K.M. Chung**, Z. Liu, C. Lu, H.-Y Tam, “Single reflective mode fiber Bragg grating in multi-mode microfiber,” *IEEE Photonics Journal*, vol. 4, no. 2, pp. 437-442, Apr. 2012.

[5] N .Bai, E. Ip, Y.-K Huang, E. Mateo, F. Yaman, M.-J Li, S. Bickham, S. Ten, J. Liñares, C. Montero, V. Moreno, X. Prieto, V. Tse, **K. M. Chung**, A. P. T. Lau, H.-Y. Tam, C. Lu, Y. Luo, G.-D. Peng, G. Li, and T. Wang, “Mode-division

multiplexed transmission with inline few-mode fiber amplifier," *Optics Express*, vol. 20, no. 3, pp. 2668–2680, 2012.

[6] C. Wu, Z. Liu, **K. M. Chung**, M. L. V. Tse, F. Y. M. Chan, A. P. T. Lau, C. Lu, and H-. Y. Tam, "Strong LP_{01} and LP_{11} mutual coupling conversion in a two-mode fiber Bragg grating," *IEEE Photonics Journal*, accepted for publication.

Conference Papers:

[1] E. Ip, N. Bai, Y. -K. Huang, E. Mateo, F. Yaman, M.-J. Li, S. Bickham, S. Ten, J. Liñares, C. Montero, V. Moreno, X. Prieto, V. Tse, **K. M. Chung**, A. Lau, H. -Y. Tam, C. Lu, Y. Luo, G. -D. Peng and G. Li, "88x3x112-Gb/s WDM Transmission over 50-km of Three-Mode Fiber with Inline Multimode Fiber Amplifier," *37th European Conference and Exposition on Optical Communications*, paper Th.13.C.2, Sep. 2011. (Post-deadline paper)

[2] **K.M. Chung**, M.L.V. Tse, and L. Dong, K.C.D Cheng and H.Y. Tam, "Observation of symmetrical reflection sidebands in a silica suspended-core fibre Bragg grating," *15th OptoElectronics and Communications Conference*, Paper 9C4-2, Sapporo, Japan, 5-9 July, 2010.

[3] **K.M. Chung**, Z. Liu, C. Lu, H. -Y Tam, "Contact force sensor based on microfiber Bragg grating," *Conference on Optical Fiber Communication 2012* (OFC'12), Paper JW2A.29.

[4] **K.M. Chung**, Z. Liu, C. Lu, H. -Y Tam, “Effective single reflection peak from large diameter microfiber Bragg gratings,” *Conference on Optical Fiber Communication 2012* (OFC’12), Paper JTh2A.4.

Chapter 2

Background review

2.1 Introduction

A fibre Bragg grating (FBG) is a length of optical fibre in which the refractive index of its core is modulated either periodically for uniform FBGs or aperidically for non-uniform FBGs. FBGs operating around the 1550 nm telecommunication window have a period of around 535-nm. FBGs function as a passive filter, reflect particular wavelengths of guided light and transmit the others.

The first grating was accidentally discovered by Hill et al. in 1978 [1]. In their experiment, an argon-ion laser with wavelength of 488-nm was butt coupled to a germanium-doped silica fibre. They observed that the light was reflected from the fibre. This phenomena was due to the refractive index of the core was modulated periodically as a result of a standing-wave interference pattern caused by the forward propagation mode and the reflection from the far end of the fibre. The so-called 'Hill' grating demonstrated the photosensitivity phenomenon of optical fibre.

More than a decade after the publication of the 'Hill' grating, Meltz et al. reported the first holographic approach of the fabrication of fibre Bragg grating (FBG) in 1989 [2]. They experimentally demonstrated a setup to make FBG though the side of the cladding with two intersecting ultraviolet (UV) beams. It was a significant development because this allows the fabrication of FBGs with different periods rather than just the period of multiples of the wavelength of the writing beam.

In 1993, an FBG fabrication technique using phase masks was developed [3], [4]. The standard phase mask technique is simple and is the most commonly used method nowadays. The phase mask splits the writing beam into two beams and interfered at the photosensitive core of the optical fibre. The fringe period solely depends on the pitch of the phase mask. This standard phase mask technique is a low-cost approach for mass production of good quality FBGs.

2.2 Fundamental of Fibre Bragg gratings

2.2.1 Photosensitivity

1550-nm uniform FBGs are in-fibre devices that have up to hundreds of thousands of periodic change of refractive index of the core with period of half a micron while the refractive index of the cladding remains unchange. To create a large number of small periodic changes, one practical approach to fabricate FBGs is by using interference formed by light. The interference fringe is then imprinted onto the fibre core. To use light for imprinting the fringe to the fibre core, it requires that the core of fibre has to be sensitive to the writing beams and its refractive index is thus changed while the cladding is transparent (insensitive) to the writing beams.

Thanks to the discovery of photosensitivity [1], fibre Bragg gratings can be fabricated in optical fibres using a laser. Photosensitivity describes a phenomenon in which permanent change in refractive index occurred due to the interaction of the material with photons of an appropriate energy. It was observed that the refractive index change in the photosensitive core of an optical fibre is proportional to the intensity of the irradiating UV light [5]. The underlying chemistry and physics giving rise to the refractive index changes remain poorly understood [6]. It was believed to be related to the color centers formed by the doped germanium in the optical fibre [7]. The UV photo excitation of oxygen-vacancy-defect states in Ge-siO_2 fibre forms paramagnetic GeE' centers that contribute to the index change [8]. It was also evident that the densification of the glass material is also correlated with the index change [9].

Photosensitive optical fibre is broadly classified into two types. The first type is that the optical fibre itself is inherently photosensitive in the core and this fibre is typically designed for the purpose of writing gratings. A number of optical fibres doped with different dopants such as tin-codoped germanosilicate, boron codoped germanosilicate fibres germanium free silicon oxynitride fibre, ternary SiO_2 : SnO_2 : Na_2O optical glass fibers, for increasing the photosensitivity were investigated [10-13]. The other type of photosensitive fibre originated from the weakly-photosensitive standard telecommunication optical fibres of which the photosensitivity can be increased by loading hydrogen.

Photosensitisation of optical fibres can be achieved by soaking the fibres in hydrogen at high pressure of about 100 bars. This process was first reported by Lemaire et al [14], in 1993 which described the treatment of a low GeO_2 doped single-mode optical fibre with hydrogen-loaded for over 12 days at 21˚C. The hydrogen loading process was then characterised by T. Erdogan [15]. After hydrogen-loading, the fibre's photosensitivity was increased dramatically. The significance of the hydrogen loading process is that it permits the use of low-cost standard single-mode optical fibre, e.g. SMF-28 from Corning Inc., for writing FBGs.

After fabrication, both the reflectivity and reflection wavelength of FBGs will change unless they are treated. Their Bragg wavelength drifts to shorter wavelength and the reflectivity is decreased. In general, annealing is needed to stabilize the gratings. The annealing process accelerated the aging of the FBGs by heating the FBGs at a higher temperature at a short time to remove the fast decay so that they decay much slower at the operating temperature.

Annealing the FBGs at temperature above 100˚C for about one day is sufficient for stabilizing FBGs used in typical temperature up to 80°C during their normal operation life [16-18]. Higher annealing temperature must be used for gratings operated at higher temperature. This method is particular important for hydrogen loaded FBGs.

2.3 Interference setup

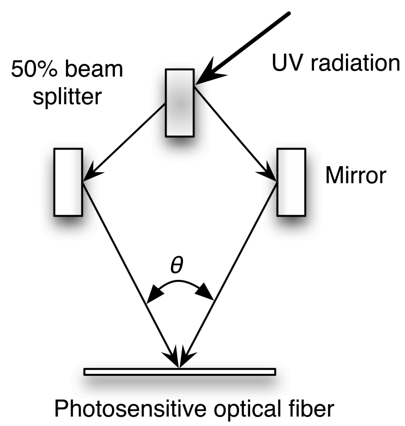

Fig. 2.1 An illustration of the interferometric setup proposed in [2].

The holography method of writing FBGs from the side of an optical fibre was illustrated [2]. The UV beam from the laser is divided into two at a beam splitter and then brought together at a mutual angle of θ, by the reflections caused by the mirrors. The optical fibre was held at the intersection of the beams. This work successfully demonstrated that a spatial interference method could be used for writing gratings. Using the interferometer configuration, the Bragg wavelength, λ_B, can be obtained by the expression:

$$\lambda_B = \frac{n_{eff}\lambda_{uv}}{\sin\left(\frac{\theta}{2}\right)}, \tag{2.3.1}$$

where λ_{uv} is the wavelength of the UV laser, n_{eff} is the effective refractive index and θ is the mutual angle of the UV beams in the air. The expression can be derived starting with considering the wave number at the interference. When the UV beam come across the optical fibre, the wave number of the UV beam is given by:

$$k = \frac{2\pi n_{uv}}{\lambda_{uv}}, \tag{2.3.2}$$

where the n_{uv} is the core refractive index at the wavelength of the writing beams (UV). The pitch of the interference can be obtained by knowing that the wave number along the longitudinal axis of the optical fibre. Figure 2.2 illustrates wave number of a writing beam at the incident angle of $\theta/2$ perpendicular to the fibre.

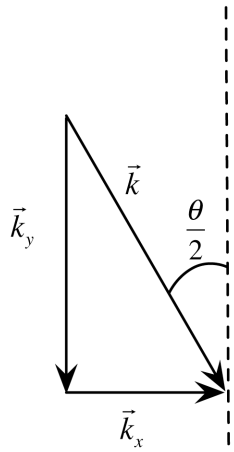

Fig. 2.2 A vector illustration of wave number of a writing beam.

By dividing $\vec{k}$, into $\vec{k}_x$ and $\vec{k}_y$, $\vec{k}_x$ is then given by:

$$k_x = \frac{2\pi}{\lambda_{uv}} n_{uv} \sin\frac{\theta_{core}}{2}, \tag{2.3.3}$$

where θ_{core} is the mutual angle at the core. Since the beams are intersected, the pitch, Λ, of constructive interference can be related as follow:

$$\begin{aligned} [k_x - (-k_x)]\Lambda &= 2\pi \\ 2k_x\Lambda &= 2\pi \end{aligned} \tag{2.3.4}$$

By substituting Eq. (2.3.2) into (2.3.3), we have,

$$\begin{aligned} \frac{2}{\lambda_{uv}} n_{uv}\Lambda \sin\frac{\theta_{core}}{2} &= 1 \\ \Lambda &= \frac{\lambda_{uv}}{2n_{av}\sin\frac{\theta_{core}}{2}}. \end{aligned} \tag{2.3.5}$$

By Snell's law, we can have the relationship between the θ and θ_{core} as follows:

$$\sin\frac{\theta_{core}}{2} = \frac{\sin\frac{\theta}{2}}{n_{av}} \tag{2.3.6}$$

By substituting the Eq. (2.3.5) into (2.3.4), we have

$$\Lambda = \frac{\lambda_{uv}}{2\sin\frac{\theta}{2}}. \tag{2.3.7}$$

The Bragg wavelength of grating is given by:

$$\lambda_B = 2n_{eff}\Lambda. \tag{2.3.8}$$

Since the period of constructive interference of the two intersecting beams is the same of the grating pitch, we put Eq. (2.3.8) into (2.3.7) and we can obtain Eq. (2.3.1).

It is worth noting that Eq. (2.3.7) implies that the period of the fringe generated by the intersecting beams is independent of any parameters of optical fibre, for example, refractive index. The period of the interference is a function of the wavelength of the UV laser and the mutual angle.

2.4 Phase mask setup

The interferometric approach provides an important technique for writing FBGs from the side of the fibre. However, the holographic interference method is challenging as it requires alignment of optical components with very high precision and stability. Any movements in optical paths potentially cause vibrations and therefore introduces phase error during the writing process. There is a need for a reliable and thus low cost for mass production of the FBGs. The use of phase mask can minimize the phase error during vibration because the fibre and phase mask can be designed on the same mechanical setup to reduce relative movement between the fibre and the phase mask.

The phase mask technique emerged as a highly reliable method for FBG fabrications. The phase mask is a self-aligning interferometer that reliably produces a highly repeatable spatially modulated interference field, which can be imprinted in photosensitive optical fibres [19].

The phase mask approach is attractive not only because it is highly reliable, but it also relaxes the tolerances on the writing setup and permits the realization of long gratings [20, 21]. Owing to these advantages, the technique is commonly used for commercial production of FBGs.

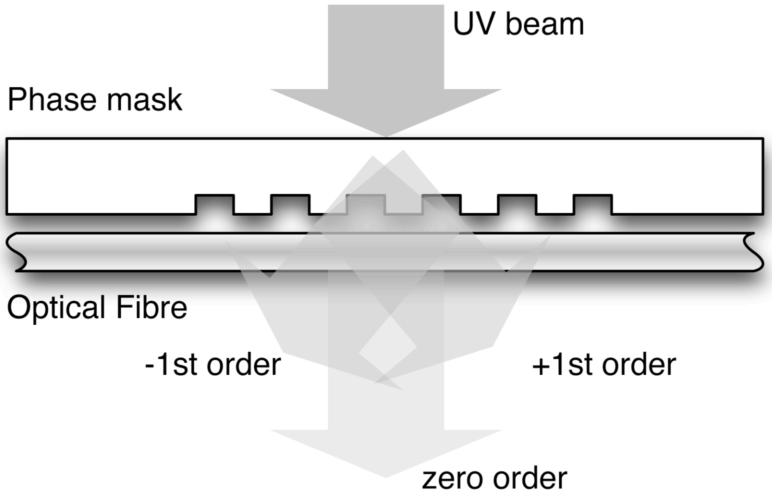

Fig. 2.3 An illustration of first order diffractions when a UV beam perpendicularly passes though a phase mask.

Figure 2.3 shows a typical phase mask tachnique for writing FBGs. The writing beam first passes though the phase mask perpendicularly and meanwhile the photosensitive optical fibre is placed just behind the mask - typically less than 100 μm from the mask. The fringe created by the ±1st orders is long enough to overlap the fibre core. The closer the distance between the fibre and the phase mask, the wider will be the width of the interference area in the fibre core. However, the fibre is not recommended to touch the phase mask to prevent contamination of the phase mask. The writing beam can burn off any coating residuals on the fibre after stripping or any dust on the surface of the fibre. Burning the dust could damage the phase mask.

The phase mask is the key component in the standard phase mask technique for FBG fabrication. It is made of UV transparent fused silica. Gooves are etched onto the fused silica with precise controlled mark-space ratio as well as depth. The Bragg wavelength of the FBG is determined by the mark-space width. The depth must be controlled precisely to reduce the 0^{th} order of the UV beam to write FBGs efficiently. To minimized the 0^{th} order, the depth, d, must be etched to a value given by $d(n_{uv} - 1) = \lambda_{uv}/2$, where n_{uv} is the refractive-index of fused silica at the UV laser writing wavelength, λ_{uv} [7]. At λ_{uv} of 244 nm, d is 262 nm. Phase masks are expensive because of the required high precision and tight tolerance. However, with proper handling, a phase mask can be used to make thousands of FBGs. Phase masks are normally fabricated by one of the two methods: (1) by exposure of a photoresist over-coated silica maskplate to an electron beam to form the pattern [22, 23], or (2) by holographic exposure [24].

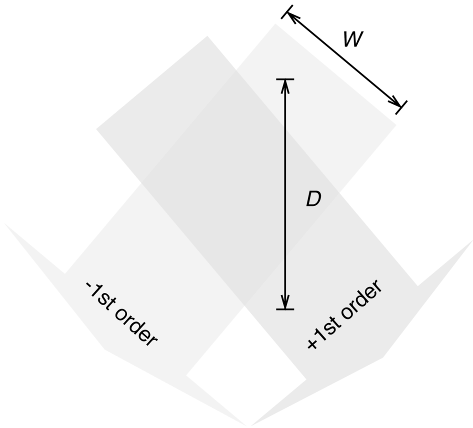

Fig. 2.4 An illustration of the overlap of two interfering UV writing beams.

Figure 2.4 shows the interference of two UV writing laser beam. The fringe pattern occurred in the overlapping region. The depth, *D,* of the fringe pattern for the interferometer is given by [7]:

$$D = \frac{W}{\tan\left(\frac{\theta}{2}\right)}, \tag{2.4.1}$$

where *W* is width of the laser beams (assuming the beams have the same width), and θ is the mutual angle of the two interfering beams. Figure 2.5 illustrates the fringe pattern using a phase mask. The depth, *d*, of the fringe is only half of that in the interference technique, and expressed as:

$$d = \frac{D}{2} = \frac{W}{2\tan\left(\frac{\theta}{2}\right)}. \tag{2.4.2}$$

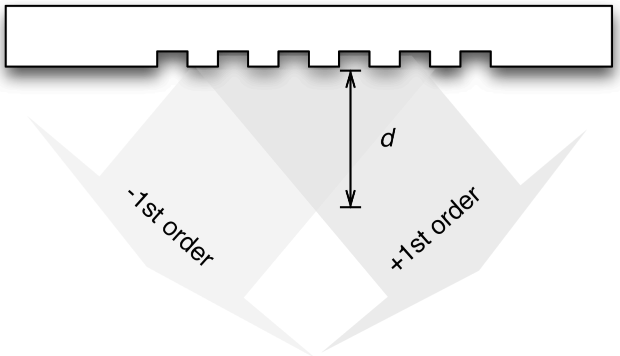

Fig. 2.5 An illustration of the overlap of the two interfering beams diffracted by a phase mask.

The UV writing beam is normally focused to a width of about 0.1 mm (W) during FBG fabrication to increase the laser intensity. And $\theta/2$ is about 10° for writing 1550 nm FBG, giving d ~ 0.5 mm. Therefore, it is important to position the fibre as close as possible to the phase mask during the FBG fabrication process.

2.5 Theory of fibre Bragg gratings

In this section, the modeling of fibre Bragg gratings will be discussed. The refractive index modulation of a fibre grating can be expressed as [7]:

$$\Delta n = \Delta n_{dc} + \Delta n_{ac} \cos[\tfrac{2\pi z}{\Lambda} + \varphi(z)], \qquad (2.5.1)$$

where Δn_{dc} is the averaged index change, Δn_{ac} is maximum amplitude of the refractive index modulation, Λ is the grating period, $\varphi(z)$ represents the chirp rate of the grating and z indicates the longitudinal position of the grating. To understand phase matching coupling condition, we can first understand how the guided mode interact with the grating.

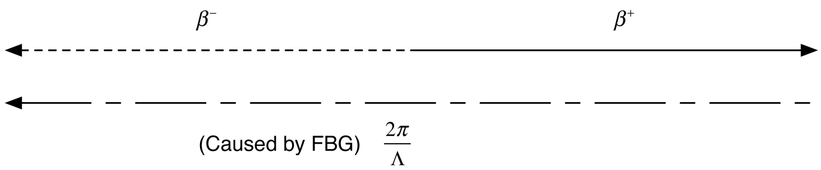

Fig. 2.6 An illustration of mode coupling of a fibre Bragg gratings written in a single mode optical fibre.

Figure 2.6 shows an illustration of mode coupling of a fibre Bragg gratings written in a single mode optical fibre. For a single mode optical fibre, β can be denoted as the propagation constant of the fundamental mode and it is a parameter that represents a measure of velocity of the mode it propagates in the longitudinal axis and "+" sign represents the mode propagates forward. When β^+ at a particular wavelength, pass though an FBG, it is coupled to backward, i.e. β^-. Effectively, the FBG is a structure that has a property that couples β^+ to its counter-propagation mode, β^- at Bragg wavelength. For the rest of wavelengths, there is no coupling. The grating structure in a sense provides an "amplitude" to couple the light at the Bragg wavelength. The magnitude of the FBG can be given as $\frac{2\pi}{\Lambda}$. β is expressed as:

$$\beta = \frac{2\pi n_{eff}}{\lambda_B}, \tag{2.5.2}$$

where n_{eff} is effective refractive index and λ_B is the Bragg wavelength. The coupling condition for -1st order of the grating can be described as [25]:

$$\beta^- = \beta^+ + (-\tfrac{2\pi}{\Lambda}). \tag{2.5.3}$$

By substituting Eq. (2.4.2) into Eq. (2.4.3), we have

$$\begin{gathered} -\frac{2\pi n_{eff}}{\lambda_B} = \frac{2\pi n_{eff}}{\lambda_B} - \frac{2\pi}{\Lambda} \\ \lambda_B = 2n_{eff}\Lambda. \end{gathered} \tag{2.5.4}$$

λ_B is a Bragg wavelength satisfying the phase match condition. The phase match condition can be found by Eq. (2.5.4). The exact solution of an FBG relating the input field and output field can be obtained by considering the mode fields of the fibre.

2.5.1 Coupled-mode equation

There are many techniques have been reported for simulating fibre Bragg gratings. [7], [25-33] Coupled mode theory is the rudiment of the modeling of fibre Bragg grating and most of the work are based on coupled mode equations [34-36]. In the ideal-mode approximation to coupled-mode theory, the transverse component of the electric field can be modeled a superposition of the modes labeled *j*, such that [25]

$$\vec{E}_t(x,y,z,t) = \sum_j [A_j(z)\exp(i\beta jz) + B_j(z)\exp(-i\beta jz)] \cdot \vec{e}_{jt}(x,y)\exp(-iwt) \quad (2.5.6)$$

where $A_j(z)$ and $B_j(z)$ are slowly varying amplitudes of the j^{th} mode propagating in $+z$ and $-z$, respectively. The transverse mode fields $\vec{e}_{jt}(x,y)$ might describe the bound-core or radiation LP modes, as given in [37]. While the modes are orthogonal in an ideal optical fibre and hence, do not exchange energy, the presence of a dielectric perturbation causes the modes to be coupled such a way that the amplitudes A_j and B_j of the j^{th} mode evolve along the z axis according to the equations [25]:

$$\frac{dA_j}{dz} = i\sum_k A_k(K_{kj}^t + K_{kj}^z)\exp(i(\beta_k - \beta_j)z] + i\sum_k B_k(K_{kj}^t - K_{kj}^z)\exp(-i(\beta_k + \beta_j)z] \quad (2.5.7)$$

$$\frac{dB_j}{dz} = -i\sum_k A_k(K_{kj}^t - K_{kj}^z)\exp(i(\beta_k + \beta_j)z] - i\sum_k B_k(K_{kj}^t + K_{kj}^z)\exp(-i(\beta_k - \beta_j)z] \quad (2.5.8)$$

where $K_{kj}^t(z)$ is the transverse coupling coefficient between the j^{th} and k^{th} mode given by

$$K_{kj}^t(z) = \tfrac{\omega}{4}\iint_\infty dx\,dy\,\Delta\varepsilon(x,y,z)\cdot\vec{e}_{kt}(x,y)\cdot\vec{e}_{jt}^{\,*}(x,y) \quad (2.5.9)$$

where $\Delta\varepsilon$ is the perturbation to the permittivity, approximately $\Delta\varepsilon \cong 2n\delta n$ for $\delta n \ll n$. The longitudinal coefficient $K_{kj}(z)$ in Eq. (2.5.7) and (2.5.8) is analogous to $K_{kj}^{t}(z)$, but generally $K_{kj}^{z}(z) \ll K_{kj}^{t}(z)$ for fibre modes, and therefore this coefficient is generally neglected. For fibre Bragg gratings, our aim is to find out how the change in refractive index relates to the coupling between the modes. We first define the coefficients [25] for the impact of Δn_{dc} and Δn_{ac} in Eq. (2.5.1)

$$\sigma_{kj}(z) = \tfrac{\omega n_{co}}{2}\overline{\sigma n}_{co} \iint\limits_{core} dx\,dy \cdot \vec{e}_{kt}(x,y) \cdot \vec{e}_{jt}^{\,*}(x,y) \tag{2.5.10}$$

$$\kappa_{kj}(z) = \tfrac{\upsilon}{2}\sigma_{kj}(z) \tag{2.5.11}$$

where σ is a "dc" (period-averaged) coupling coefficient and κ is an "AC" coupling coefficient, then the general coupling due to the modulation in refractive index can be written as:

$$K_{kj}^{t}(z) = \sigma_{kj}(z) + 2\kappa_{kj}(z)\cos[\tfrac{2\pi}{\Lambda}z + \varphi(z)]. \tag{2.5.12}$$

By making synchronous approximation reported in [38], the coupled mode equations in a Bragg grating were simplified to two equations [25]:

$$\frac{dR}{dz} = i\hat{\sigma}R(z) + i\kappa S(z) \tag{2.5.13}$$

$$\frac{dS}{dz} = -i\hat{\sigma}S(z) + i\kappa^{*}S(z) \tag{2.5.14}$$

where the amplitudes R and S are $R(z) = A(z)\exp(i\delta z - \varphi/2)$ and $S(z) = B(z)\exp(-i\delta z + \varphi/2)$, κ is the "AC" coupling coefficient from Eq. (2.5.11) and $\hat{\sigma}$ is a "dc" self-coupling coefficient defined as [25]

$$\hat{\sigma} = \delta + \sigma - \tfrac{1}{2}\tfrac{d\varphi}{dz}, \tag{2.5.15}$$

where the detuning factor δ, which is a function the wavelengths, determines the phase matching condition and is obtained by [25]:

$$\begin{aligned} \delta &= \beta - \frac{\pi}{\Lambda} \\ &= \beta - \beta_D \\ &= 2\pi n_{eff}\left(\frac{1}{\lambda} - \frac{1}{\lambda_D}\right), \end{aligned} \tag{2.5.16}$$

where $\lambda_D = 2n_{eff}\Lambda$ is the design wavelength for the Bragg grating with the pitch, Λ. When λ equals to the design wavelength, $\delta = 0$. The term $(½)d\varphi/dz$ in Eq. (2.5.15) describes possible chirp of the grating period.

For a reflection grating, we have [25]

$$\sigma = \frac{2\pi}{\lambda}\overline{\delta n_{eff}} \tag{2.5.17}$$

$$\kappa = \kappa^* = \frac{\pi}{\lambda}\upsilon(z)\overline{\delta n_{eff}} \tag{2.5.18}$$

$$-\frac{1}{2}\frac{d\varphi}{dz} = \frac{4\pi n_{eff} z}{\lambda_D^2}\frac{d\lambda_D}{dz} \tag{2.5.19}$$

For a uniform grating along z, $\overline{\delta n_{eff}}$ is a constant and $v(z)$ is the visibility of the "AC" refractive index modulation, it is mainly used to model the apodisation profile along the z axis.

2.5.2 Transfer matrix

We have got the parameters to simulate a uniform fibre Bragg grating using the coupled-mode equations. To simulate a nonuniform grating such as apodised, chirped and phase shifted grating, a method called transfer matrix can be used. It is a technique to put the characteristics of a grating into a transfer function as a matrix form that relates the input and output fields. The relation can be written in the form of [25]:

$$\begin{pmatrix} R(-\frac{L}{2}) \\ S(-\frac{L}{2}) \end{pmatrix} = \mathbf{T} \begin{pmatrix} R(\frac{L}{2}) \\ S(\frac{L}{2}) \end{pmatrix} \tag{2.5.20}$$

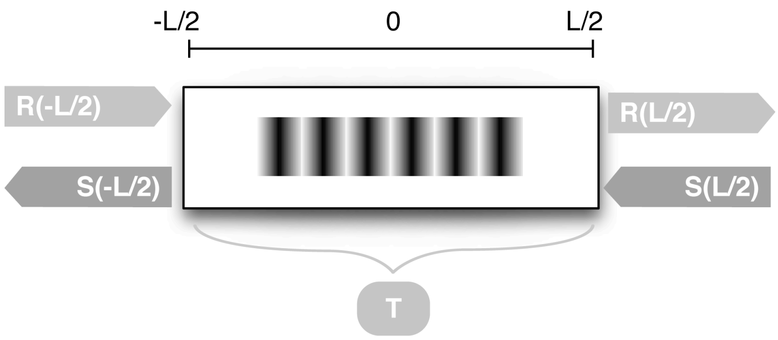

Fig. 2.7 A model of transfer matrix for a uniform grating.

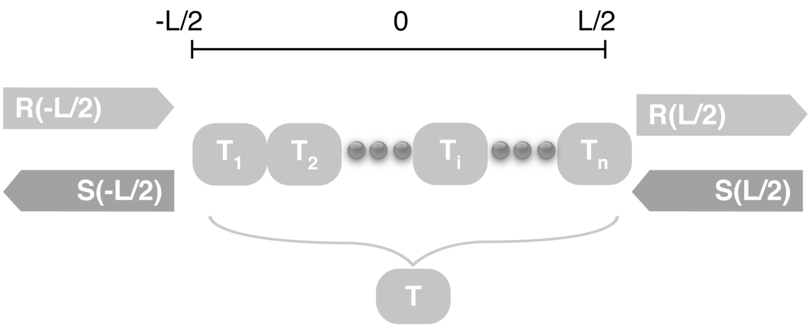

Fig. 2.8 A model of transfer matrix for a nonuniform grating.

Figure 2.7 illustrates a diagram that relates a uniform grating as a transfer matrix, **T**, to the input and output fields. Transfer matrix provides a framework to simulate a grating. By characterizing a nonuniform grating into many segments of different uniform gratings, the resulted spectra response can be obtained. Figure 2.8 indicates how transfer matrix is used to model a nonuniform grating by using a number of $\mathbf{T}_i$ representing a uniform grating. The model then become:

$$\begin{pmatrix} R(-\frac{L}{2}) \\ S(-\frac{L}{2}) \end{pmatrix} = \mathbf{T}_1 \cdot \mathbf{T}_2 \cdots \mathbf{T}_i \cdots \mathbf{T}_n \begin{pmatrix} R(\frac{L}{2}) \\ S(\frac{L}{2}) \end{pmatrix}, \tag{2.5.21}$$

where $\mathbf{T} = \mathbf{T}_1 \cdot \mathbf{T}_2 \cdots \mathbf{T}_i \cdots \mathbf{T}_n$. In each input and output field, the transfer matrix, $\mathbf{T}_i$, satisfy the condition as a transfer function, i.e.,

$$\begin{pmatrix} R_i \\ S_i \end{pmatrix} = \mathbf{T}_i \begin{pmatrix} R_{i-1} \\ S_{i-1} \end{pmatrix}. \tag{2.5.22}$$

Using the coupled-mode equations Eq. (2.5.13) and (2.5.14), the transfer matrix elements can be defined as [25]:

$$\mathbf{T}_i = \begin{pmatrix} \cosh(\Delta z\gamma) - i\frac{\hat{\sigma}}{\gamma}\sinh(\Delta z\gamma) & -i\frac{\kappa}{\gamma}\sinh(\Delta z\gamma) \\ i\frac{\kappa}{\gamma}\sinh(\Delta z\gamma) & \cosh(\Delta z\gamma) - i\frac{\hat{\sigma}}{\gamma}\sinh(\Delta z\gamma) \end{pmatrix}, \tag{2.5.23}$$

where the parameter, Δz, is the length of the uniform grating segments. For any uniform gratings, Δz cannot be too small; otherwise the coupled mode equations are not valid al [31]. Typically, 100 sections are good enough for simulation a nonuniform or chirped grating [25]. The parameter, γ is of the form:

$$\gamma = \sqrt{\kappa^2 - \hat{\sigma}^2}. \tag{2.5.24}$$

where κ and $\hat{\sigma}$ are defined in Eq. (2.5.15) and (2.5.18), respectively. To simulate a phase shifted grating, $\mathbf{T}_\theta$ can be inserted into the corresponding transfer matrices, and is of the form:

$$\mathbf{T}_\theta = \begin{pmatrix} \exp(\frac{-i\varphi}{2}) & 0 \\ 0 & \exp(\frac{i\varphi}{2}) \end{pmatrix}. \tag{2.5.25}$$

2.5.3Boundary conditions

To numerically calculate the transmission and reflection field of an FBG, we need define the boundary conditions. There were two different sets of boundary conditions reported in literature [7], [25]. Both conditions also lead to the same solution. According to [25], for a Bragg grating of length of L, taking R(L/2)=1 and S(L/2)=0 and integrating backward from z =L/2 to z =-L/2, we thus obtain R(-L/2) and S(-L/2).

$$\begin{pmatrix} R(-\frac{L}{2}) \\ S(-\frac{L}{2}) \end{pmatrix} = \begin{pmatrix} T_a & T_b \\ T_c & T_d \end{pmatrix} \begin{pmatrix} 1 \\ 0 \end{pmatrix}, \text{ from [25]} \tag{2.5.26}$$

$$\begin{pmatrix} R(-\frac{L}{2}) \\ S(-\frac{L}{2}) \end{pmatrix} = \begin{pmatrix} T_a \\ T_c \end{pmatrix}. \tag{2.5.27}$$

The propagation field should be normalized to the input transmission field of the grating. Therefore, the reflected field is given by:

$$\frac{S\left(\frac{-L}{2}\right)}{R(\frac{-L}{2})} = \frac{T_c}{T_a}, \tag{2.5.28}$$

and the transmission field is then given by:

$$\frac{R\left(\frac{L}{2}\right)}{R(\frac{-L}{2})} = \frac{1}{T_a}. \tag{2.5.29}$$

Using the other set of boundary values defined by [7], we set the input field amplitude *R(-L/2)* is normalized to unity and the reflected field amplitude at the output of the grating *S(L/2)* is zero. Since there is no perturbation beyond the end of the gratings, we have

$$\begin{aligned}\begin{pmatrix} 1 \\ S(-\tfrac{L}{2}) \end{pmatrix} &= \begin{pmatrix} T_a & T_b \\ T_c & T_d \end{pmatrix}\begin{pmatrix} R(\tfrac{L}{2}) \\ 0 \end{pmatrix}, \\ &= \begin{pmatrix} T_a R(\tfrac{L}{2}) \\ T_c R(\tfrac{L}{2}) \end{pmatrix}\end{aligned} \quad \text{from [7].} \qquad (2.5.30)$$

So, the boundary conditions become,

$$\begin{pmatrix} R(\tfrac{-L}{2}) & R(\tfrac{L}{2}) \\ S(\tfrac{-L}{2}) & S(\tfrac{L}{2}) \end{pmatrix} = \begin{pmatrix} 1 & \tfrac{1}{T_a} \\ \tfrac{T_c}{T_a} & 0 \end{pmatrix}. \qquad (2.5.31)$$

The reflected and transmission fields are

$$\frac{S\left(\tfrac{-L}{2}\right)}{R(\tfrac{-L}{2})} = \frac{T_c}{T_a}, \qquad (2.5.32)$$

and

$$\frac{R\left(\tfrac{L}{2}\right)}{R(\tfrac{-L}{2})} = \frac{1}{T_a}. \qquad (2.5.33)$$

We can still obtain the same solution as shown in Eq. (2.5.28) and (2.5.29). The resulted reflection and transmission amplitude are then:

$$\text{Reflection amplitude} = \frac{\operatorname{Re}\left(T_c\right)^2}{\operatorname{Re}\left(T_a\right)^2} \qquad (2.5.34)$$

$$\text{Transmission amplitude} = \frac{1}{\operatorname{Re}\left(T_a\right)^2} \qquad (2.5.35)$$

2.6 Simulated FBGs

In this section, a number of simulation results of the spectra of fibre Bragg gratings will be presented. In this work, all the simulations are calculated using transfer matrix coded by the author from scratch in the software platform Labview™. The parameters if unspecified generally are set to as follows:

The grating length was set to be 10-cm.

1. Δz was 100 times of the pitch length.

2. n_{eff} is 1.4483

3. Λ is 535.11-nm

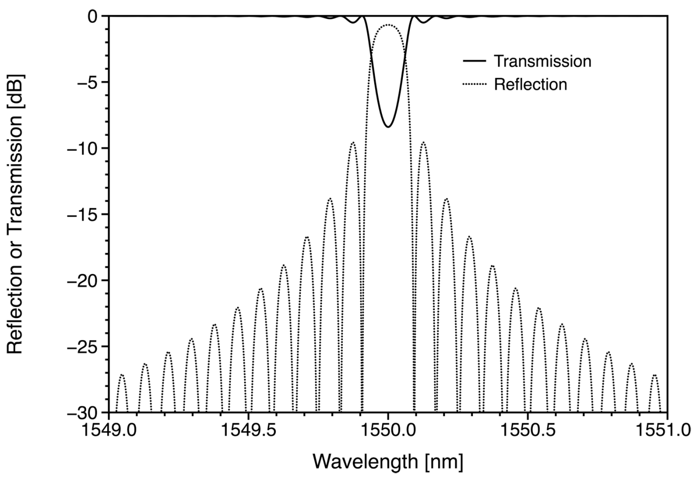

Fig. 2.9 Simulated spectra of a uniform fibre Bragg grating.

Figure 2.9 shows the simulated spectra of a uniform FBG. The averaged induced Δn_{eff} is $8\text{x}10^{-5}$ along the grating.

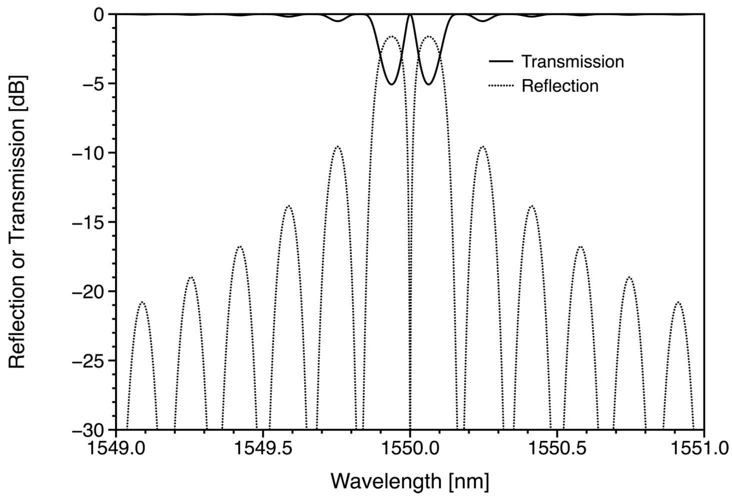

Fig. 2.10 Simulated spectra of a π-phase shifted fibre Bragg grating.

Figure 2.10 shows the simulated spectra of a π-phase shifted FBG. The π-phase shift transfer matrix was inserted in the middle of the grating (5-cm position) and Δneff was remained the same as the uniform grating, i.e. $8x10^{-5}$. It is clear that there is a very narrow band of transmission located exactly at the Bragg wavelength because of the inserted phase shift.

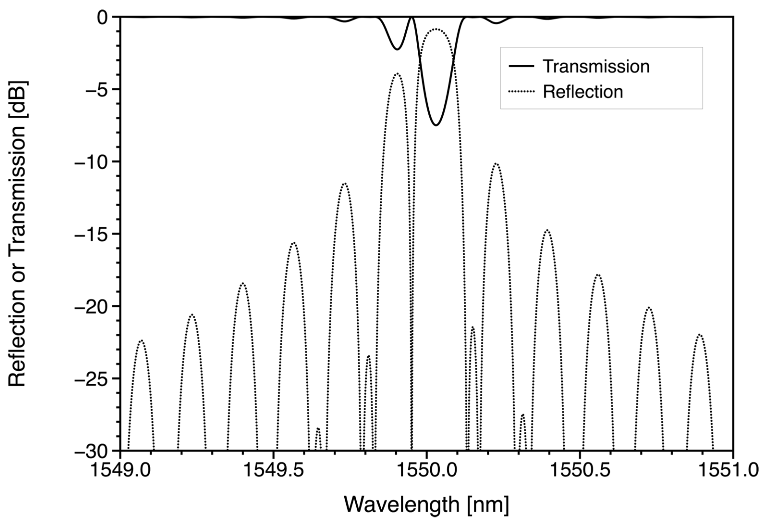

Fig. 2.11 simulated spectra of a π/2-phase shifted fibre Bragg grating.

Two fibre Bragg gratings with π/2 and 3π/2 phase shift inserted in the middle of the gratings are demonstrated in Fig. 2.11 and 2.12, respectively. The locations of the narrow transmission bands are shifted as a function of the phase shift degree. The phase shifted grating written in doped fibre is often adapted as a fibre laser together because it provides a very narrow transmission band.

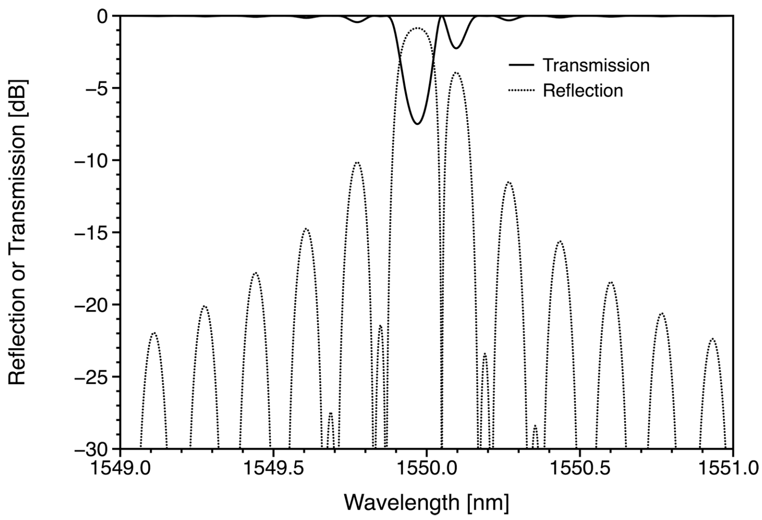

Fig. 2.12 simulated spectra of a 3π/2-phase shifted fibre Bragg grating.

FBGs have unwanted side lobes next to the Bragg wavelength. To suppress them, apodisation of the grating profile is needed. The side lobes of the grating was a result of the abrupt change of the refractive indices at both ends of the grating. From the mathematic viewpoint, the Fourier transform of a uniform grating profile (rectangular) function yields the "sinc" function, with its associated side lobes structure apparent in the spectrum. In the weak, grating, the reflection spectra of an FBG, can be approximated as the Fourier transform of the grating profile. Since, the Fourier transform of the a uniform grating is a "sinc" function, it results that the spectrum have a lot of side lobes located next to both sides of the Bragg wavelength. In contrast, for the transformation of a Gaussian function, it results in no side lobe. Therefore, if the grating profile is a Gaussian or closed to Gaussian function, the reflection spectrum of a grating should have no side lobe or the side lobe is suppressed. An apodisation window is normally used for shaping the envelope of the refractive index modulation.

Hill and Matsuhara [39, 40] reported that apodisation of a periodic wave-guide structure suppresses the side lobes before the discovery of FBG. The use of apodisation profiles in the "AC" grating profile is a well-known technique for suppressing the unwanted side lobes. Figure 2.13 and 2.14 shows a hamming apodised profile and its spectra simulation result. It is worthy noting that shaping the envelope of periodic refractive index modulation (AC) as a Gaussian-like results in shaping the averaged refractive index (DC) in the same shape. Simply changing the refractive index modulation amplitude changes the local Bragg wavelength as well, because of the "unflattening" of n_{dc}.

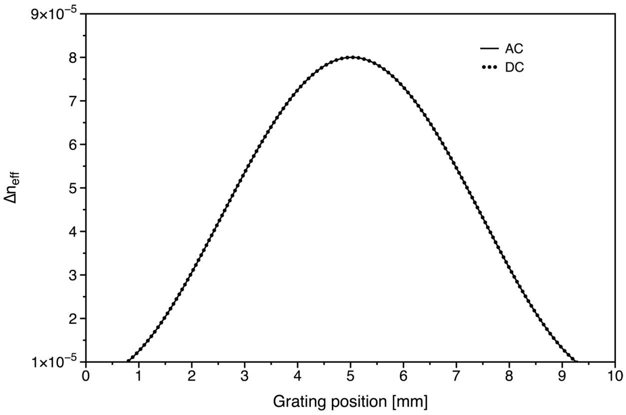

Fig. 2.13 Grating profile of an apodised fibre Bragg grating with hamming window.

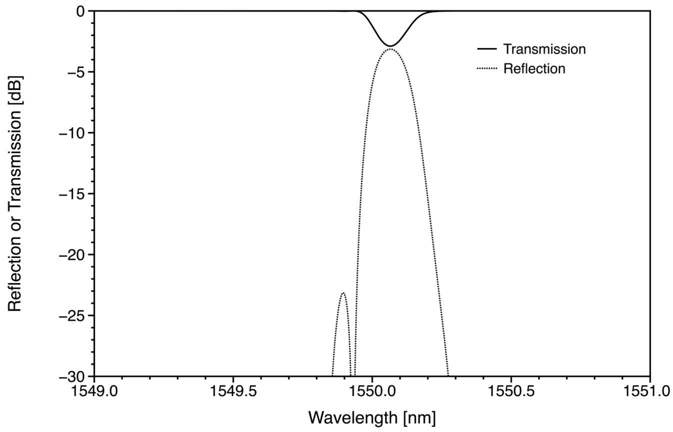

Fig. 2.14 Spectra of an apodised fibre Bragg grating with hamming window.

It is resulting that a slightly stronger side peak appears on the shorter wavelength of the Bragg wavelength. The reason is that the local Bragg wavelengths along the grating caused by the non-uniform n_{eff} form a distributed Fabry-Perot interferometer [41], which causes structure to appear on the shorter wavelength of the reflection spectrum of the grating, although side-lobe amplitudes are reduced. To avoid this complication, the n_{dc} should be kept constant along the grating profile meanwhile the "AC" maintain the shape of the apodisation. Figure 2.15 shows an apodised FBG with flatten n_{dc} while the modulation n_{ac} is enveloped in a hamming profile. The spectra of the grating is shown in Fig. 2.16. The side lobe at the shorter wavelength is suppressed.

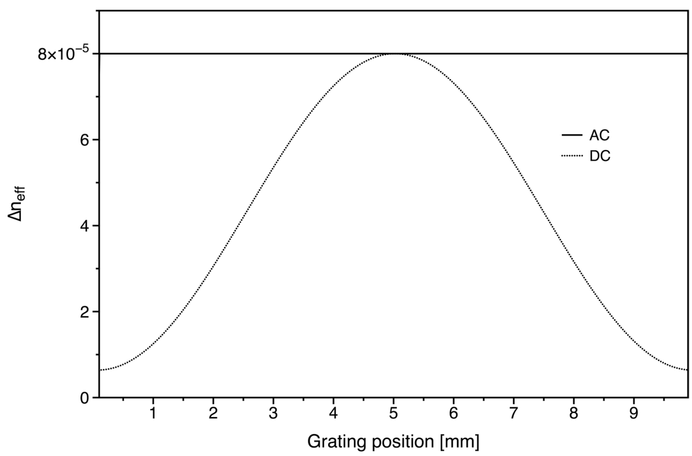

Fig. 2.15 Grating profile of an apodised fibre Bragg grating with hamming window.

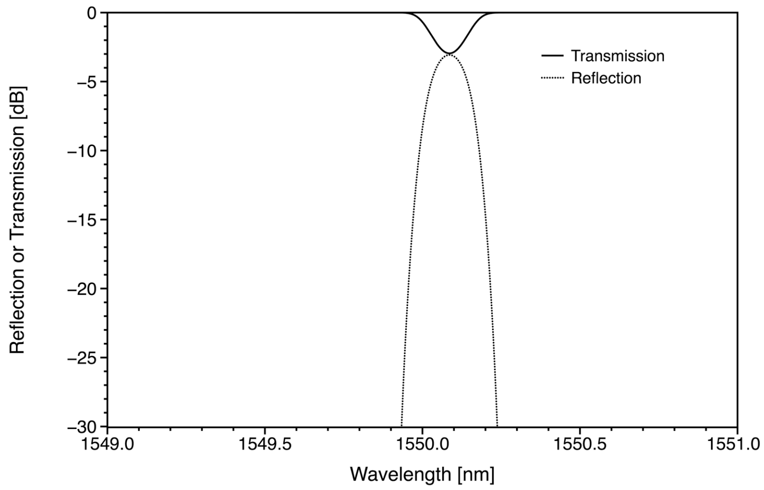

Fig. 2.16 Spectra of an apodised fibre Bragg grating with hamming window.

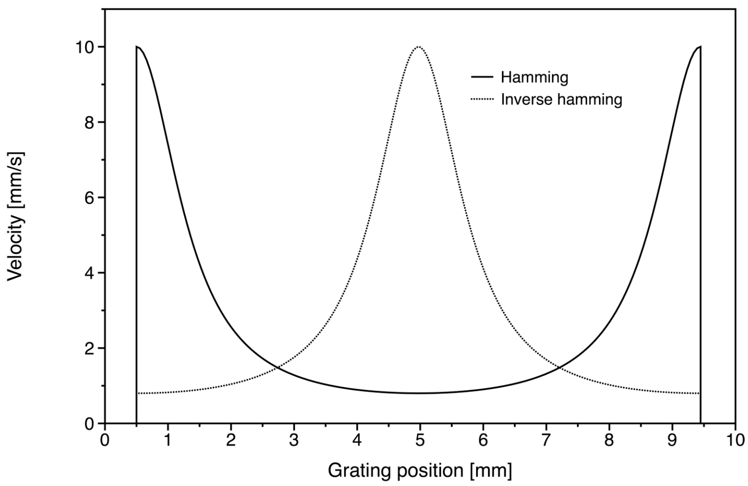

Fig. 2.17 Scanning profile of an apodised fibre Bragg grating with hamming window.

The apodisation with DC flattening can be realized by scanning UV beams twice with different profiles [42, 43]. The simulation results of the hamming scanning profile and its inverse profile are shown in Fig. 2.17. The scanning profile is used to simulate that a laser beam with 1-mm width is used to scan 9-mm along the photosensitive fibre core. The UV dose along the grating is inversely proportional to the velocity at its positions. An inverse hamming profile is used to flatten the n_{dc} and therefore the local Bragg wavelength along the grating can be coherent.

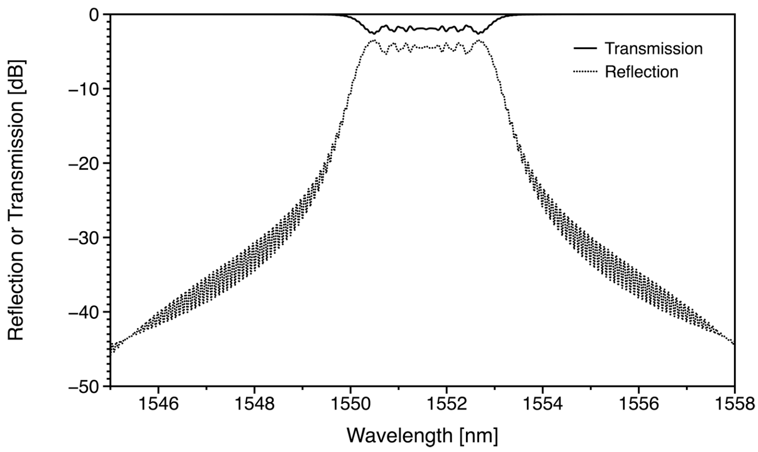

Fig. 2.18 Spectra of a uniform linear chirped fibre Bragg grating.

Chirped fibre Bragg grating contains non-uniform period along their length. Chirp in gratings may have many different forms. The chirp usually be linear, i.e., the period varies linearly with length of the grating [44]. Figure 2.18 shows the simulation result of a uniform chirped FBG with a linear chirp rate of 1-nm/mm and Δn of 2×10^{-4}. It is worth noting that the reflection of the uniform chirped grating is much lower than that of the uniform grating at the same refractive index modulation. The local Bragg wavelength along the grating is linearly shifting towards longer wavelength because of the positive chirp rate. As a result, the grating's spectra have two characteristics. First, the spectra are broader. The other is that there are some ripples in the spectra. This is due to the Fabry Pérot interference inside the grating. The ripples can be minimized by apodising the chirped grating. Figure 2.19 and 2.20 show the chirped grating with apodisation and the grating profile, respectively. The result proves that the spectrum shape is optimized, but the penalty is that the reflection is also weak as the effective length of the grating is shortened and the average refractive index modulation is also decreased.

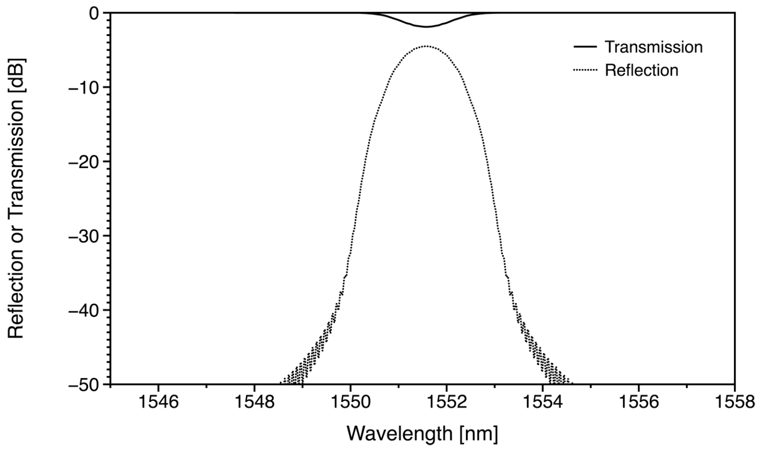

Fig. 2.19 Spectra of an apodised linear chirped fibre Bragg grating.

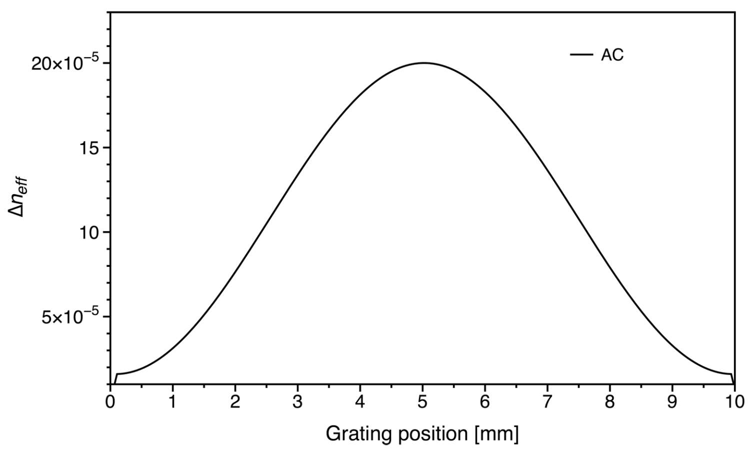

Fig. 2.20 Hamming profile for the apodised linear chirped fibre Bragg gratings.

2.7 Chapter summary

In this chapter, the fundamental theories of fibre Bragg gratings have been reviewed. The discussions of the fabrications of FBGs using interference and standard phase mask technique followed by a brief introduction of photosensitivity were also presented. The coupled mode theory and transfer matrix technique were studied. The spectra response of a number of simulated FBGs including uniform, phase shifted, apodised and chirped were analysed.

Reference

[1] K. O. Hill, Y. Fujii, D. C. Johnson, and B. S. Kawasaki, "Photosensitivity in Optical Fiber Waveguides - Application to Reflection Filter Fabrication," *Applied Physics Letters*, vol. 32, no. 10, pp. 647–649, 1978.

[2] G. Meltz, W. W. Morey, and W. H. Glenn, "Formation of Bragg Gratings in Optical Fibers by a Transverse Holographic Method," *Optics Letters*, vol. 14, no. 15, pp. 823–825, Aug. 1989.

[3] K. O. Hill, B. Malo, F. Bilodeau, D. C. Johnson, and J. Albert, "Bragg gratings fabricated in monomode photosensitive optical fiber by UV exposure through a phase mask," *Applied Physics Letters*, vol. 62, no. 10, p. 1035, 1993.

[4] D. Z. Anderson, V. Mizrahi, T. Erdogan, and A. E. White, "Production of in-fibre gratings using a diffractive optical element," *Electronics Letters*, vol. 29, no. 6, pp. 566–568, 1993.

[5] V. Mizrahi, S. LaRochelle, G. Stegeman, and J. Sipe, "Physics of photosensitive-grating formation in optical fibers," *Physical Review A*, vol. 43, no. 1, pp. 433–438, Jan. 1991.

[6] J. Canning, "Photosensitization and Photostabilization of Laser-Induced Index Changes in Optical Fibers", *Optical Fiber Technology*, vol. 6, pp. 275–289, 2000.

[7] R. Kashyap, *Fiber Bragg Gratings*. Academic Pr, 2009.

[8] T.-E. Tsai, G. M. Williams, and E. J. Friebele, "Index structure of fiber Bragg gratings in Ge–SiO_2 fibers," *Optics Letters*, vol. 22, no. 4, pp. 224–226, 1997.

[9] B. Poumellec, "UV induced densification during Bragg grating inscription in Ge:SiO_2 preforms," *Optical Materials*, vol. 4, no. 4, pp. 441–449, Mar. 1995.

[10] L. Dong, J. L. Cruz, L. Reekie, M. G. Xu, and D. N. Payne, "Enhanced photosensitivity in tin-codoped germanosilicate optical fibers," *IEEE Photonics Technology Letters*, vol. 7, no. 9, pp. 1048–1050, 1995.

[11] D. L. Williams, B. J. Ainslie, J. R. Armitage, R. Kashyap, and R. Campbell, "Enhanced UV photosensitivity in boron codoped germanosilicate fibres," *Electronics Letters*, vol. 29, no. 1, 1993.

[12] E. M. Dianov, K. M. Golant, R. R. Khrapko, Kurkov, "Grating formation in a germanium free silicon oxynitride fibre," *Electronics Letters*, vol. 33, no. 3, pp. 236–238, 1997.

[13] G. Brambilla, V. Pruneri, L. Reekie, C. Contardi, D. Milanese, and M. Ferraris, "Bragg gratings in ternary SiO_2 : SnO_2 : Na_2O optical glass fibers," *Optics Letters*, vol. 25, no. 16, pp. 1153–1155, 2000.

[14] P. Lemaire, R. Atkins, and V. Mizrahi, "High pressure H_2 loading as a technique for achieving ultrahigh UV photosensitivity and thermal sensitivity in

GeO_2 doped optical fibres," *Electronics Letters*, vol. 29, no. 13, pp. 1191–1193, 1993.

[15] T. Erdogan and V. Mizrahi, "Characterization of UV-induced birefringence in photosensitive Ge-doped silica optical fibers," *Journal of the Optical Society of America B-Optical Physics*, vol. 11, no. 10, pp. 2100–2105, 1994.

[16] S. Baker, H. Rourke, V. Baker, and D. Goodchild, "Thermal decay of fiber Bragg gratings written in boron and germanium codoped silica fiber," *Journal of Lightwave Technology*, vol. 15, no. 8, pp. 1470–1477, 1997.

[17] L. Dong and W. F. Liu, "Thermal decay of fiber Bragg gratings of positive and negative index changes formed at 193 nm in a boron-codoped germanosilicate fiber," *Applied Optics*, vol. 36, no. 31, p. 8222, 1997.

[18] Y. Shen et al., "Thermal decay characteristics of strong fiber Bragg gratings showing high-temperature sustainability," *Journal of the Optical Society of America B-Optical Physics*, vol. 24, no. 3, p. 430, 2007.

[19] S. J. Mihailov et al., "Fiber Bragg gratings made with a phase mask and 800-nm femtosecond radiation," *Optics letters*, vol. 28, no. 12, pp. 995–997, 2003.

[20] H. N. Rourke, S. R. Baker, K. C. Byron, R. S. Baulcomb, S. M. Ojha, and S. Clements, "Fabrication and characterisation of long, narrowband fibre gratings by phase mask scanning," *Electronics Letters*, vol. 30, no. 16, p. 1341, 1994.

[21] J. Martin and F. Ouellette, "Novel writing technique of long and highly reflective in-fibre gratings," *Electronics Letters*, vol. 30, no. 10, p. 811, 1994.

[22] A. Othonos and K. Kalli, *Fiber Bragg gratings*. Artech House Publishers, 1999, p. 422.

[23] K. O. Hill and G. Meltz, “Fiber Bragg grating technology fundamentals and overview,” *Journal of Lightwave Technology*, vol. 15, no. 8, pp. 1263–1276, Aug. 1997.

[24] C. R. Giles, “Lightwave applications of fiber Bragg gratings,” *Journal of Lightwave Technology*, vol. 15, no. 8, pp. 1391–1404, 1997.

[25] T. Erdogan, “Fiber grating spectra,” *Journal of Lightwave Technology*, vol. 15, no. 8, pp. 1277–1294, Aug. 1997.

[26] E. Peral and J. Capmany, “Generalized Bloch wave analysis for fiber and waveguide gratings,” *Journal of Lightwave Technology*, vol. 15, no. 8, pp. 1295–1302, 1997.

[27] E. Peral, J. Capmany, and J. Marti, “Iterative solution to the Gel'Fand-Levitan-Marchenko coupled equations and application to synthesis of fiber gratings,” *IEEE Journal of Quantum Electronics*, vol. 32, no. 12, pp. 2078–2084, 1996.

[28] S. Radic, N. George, and G. P. Agrawal, “Analysis of nonuniform nonlinear distributed feedback structures: generalized transfer matrix method,” *IEEE Journal of Quantum Electronics*, vol. 31, no. 7, pp. 1326–1336, Jul. 1995.

[29] K. A. Winick, “Effective-index method and coupled-mode theory for almost-periodic waveguide gratings: a comparison,” *Applied Optics*, vol. 31, no. 6, pp. 757–764, 1992.

[30] P. Verly, J. Dobrowolski, and W. Wild, “Synthesis of high rejection filters with the Fourier transform method,” *Applied Optics*, vol. 28, no. 14, pp. 2864–2875, 1989.

[31] M. Yamada and K. Sakuda, “Analysis of almost-periodic distributed feedback slab waveguides via a fundamental matrix approach,” *Applied Optics*, vol. 26, no. 16, pp. 3474–3478, 1987.

[32] L. A. Weller-Brophy and D. G. Hall, “Analysis of waveguide gratings: application of Rouard’s method,” *Journal of the Optical Society of America a-Optics Image Science and Vision*, vol. 2, no. 6, p. 863, 1985.

[33] M. Matsuhara, K. O. Hill, and A. Watanabe, “Optical-waveguide filters: Synthesis,” *Journal of the Optical Society of America*, vol. 65, no. 7, pp. 804–809, 1975.

[34] M. Born and E. Wolf, *Principles of Optics*. Cambridge Univ Pr, 2000.

[35] A. Yariv, “Coupled-mode theory for guided-wave optics,” *Quantum Electronics*, vol. 9, no. 9, pp. 919–933, 1973.

[36] H. Haus, “Coupled-mode theory,” in *Proceedings of the IEEE*, 1991.

[37] D. Marcuse, *Theory of dielectric optical waveguides*. Academic Press, 1991.

[38] H. Kogelnik, *Theory of optical waveguides*. Guided-Wave Optoelectronics, 1990.

[39] K. O. Hill, “Aperiodic Distributed-Parameter Waveguides for Integrated Optics,” *Applied Optics*, vol. 13, no. 8, pp. 1853–1856, 1974.

[40] M. Matsuhara and K. O. Hill, "Optical-Waveguide Band-Rejection Filters: Design," *Applied Optics*, vol. 13, no. 12, p. 2886, 1974.

[41] V. Mizrahi and J. E. Sipe, "Optical properties of photosensitive fiber phase gratings," *Journal of Lightwave Technology*, vol. 11, no. 10, pp. 1513–1517, 1993.

[42] B. Malo, S. Theriault, D. C. Johnson, F. Bilodeau, J. Albert, and K. O. Hill, "Apodized in-fibre Bragg grating reflectors photoimprinted using a phase mask," *Electronics Letters*, vol. 31, no. 3, pp. 223–225, 1995.

[43] T. Komukai, K. Tamura, and M. Nakazawa, "An efficient 0.04-nm apodized fiber Bragg grating and its application to narrow-band spectral filtering," *IEEE Photonics Technology Letters*, vol. 9, no. 7, pp. 934–936, Jul. 1997.

[44] K. C. Byron, K. Sugden, T. Bricheno, and I. Bennion, "Fabrication of chirped Bragg gratings in photosensitive fibre," *Electronics Letters*, vol. 29, no. 18, pp. 1659–1660, 1993

Chapter 3

Novel fibre Bragg grating fabrication system

3.1 Introduction

The discovery of fibre photosensitivity by Hill et al. in 1978 [1] followed by Meltz's demonstration of writing gratings at any wavelengths around the 1550 nm wavelength through fibre cladding in 1989 [2], spurred the rapid development of FBG technology. Various types of FBG fabrication techniques have been developed [3-11] and FBGs are becoming critical elements in sensors and optical communication systems [7], [8]. High quality FBGs are immensely useful in a variety of applications. In principle, FBGs with complicated designs are capable of providing optical filters that meet complex spectral and dispersion requirements. Complicated grating structures cannot be fabricated using the standard phase mask technique [9-11] and required sophisticated two-beam interferometer grating fabrication approach [3-6]. Design software based on inverse scattering approaches are well developed [12-16]. With these new complicated grating design tools, a practical effective FBG fabrication setup capable of varying both apodisation and local grating phase is acheivable.

About 10 years ago Liu et al. demonstrated an approach to write arbitrary FBG using a translate-and-write configuration [4,17]. The setup employed an air-bearing translation stage with very stable velocity characteristics with the aid of laser encoder. By synchronizing the shutter and translation stage with a pre-generated grating profile, high performance arbitrary FBGs can be written using a translate-and-write method. The pre-generated grating profile for signaling the shutter on/off switching ensures that the on and off time synchronize to the highly accurate translation stage running at its optimum constant velocity. The writing beam can be able to scan along an optical fibre over hundreds of times with minimal errors.

In 2008, Gagne et al. reported another interferometer scheme with push-pull electro-optic modulation to write fibre Bragg gratings [5]. In their technique, two electro-optical phase modulators were placed in the two optical paths. Interference patterns are formed in the core of the moving fibre. The setup requires synchronization of the phase modulator and the motor, which translates along the fibre. Phase of the fringe pattern, and consequently the corresponding phase in the FBG, at any fibre position can be controlled by a pair of phase modulators and a motor. No moving part in the optical setup is the key feature that minimizes moving errors in this configuration.

Another approach to fabricate sohphisticated FBGs such as high-channel count linear chirped FBG for dispersion-compensation of the entire C-band was proposed by Li et al. who used a novel diffraction pre-compensated phase mask [18]. A special tailor-made phase mask with complicated profile was used. The advantages of this technique are: (1) FBG fabrication is simplified by transferring the main challenges to phase mask design and (2) better reproducible FBGs. However, this approach is not flexible in that different phase masks are needed for different FBGs.

The aforementioned techniques have been applied to make FBGs for many new applications requiring more sophisticated FBG designs, such as multichannel dispersion compensators, multichannel fibre lasers and distributed feedback fibre lasers.

In this chapter, we propose a novel fibre Bragg grating (FBG) fabrication setup. The FBG fabrication system comprised of an interferometric setup and a phase mask. The optical design aims to provide all the controls of grating parameters by only controlling three linear translation stages of very high position accuracy and nanometer resolution. The system is capable of writing long FBGs using a translate-and-write process and allows sophisticated FBGs with arbitrary chirp and apodisation to be fabricated. The local Bragg wavelength is determined by the movement of the phase mask controlled by a PZT in the direction perpendicular to its surface (Y-axis). The focusing points of the two interference beams remains unchanged at various positions of the phase mask. This is a unique feature of the proposed design, providing robustness and stability because separate adjustments of the two UV writing beams are avoided. Grating apodisation is achieved by moving the phase mask in the direction parallel to its surface (X-axis) using a PZT. Phase steps can also be implemented by stepping the X-axis controller. Compared to the standard phase mask writing technique where the fibre has to be placed close to the phase mask, this novel design allows more focused beam on the fibre and, consequently, faster writing. A long uniform FBG and a linearly chirped FBG are written to demonstrate the capability of the novel FBG fabrication technique.

3.2 Operation principle

Figure 3.1 shows a schematic diagram of the proposed FBG fabrication setup. A computer installed with the software Labview™ controls all the equipment used in this setup, except the Argon ion laser. Synchronization of the controls of the translation stages and shutter is pre-programmed in the software to realize various kinds of gratings.

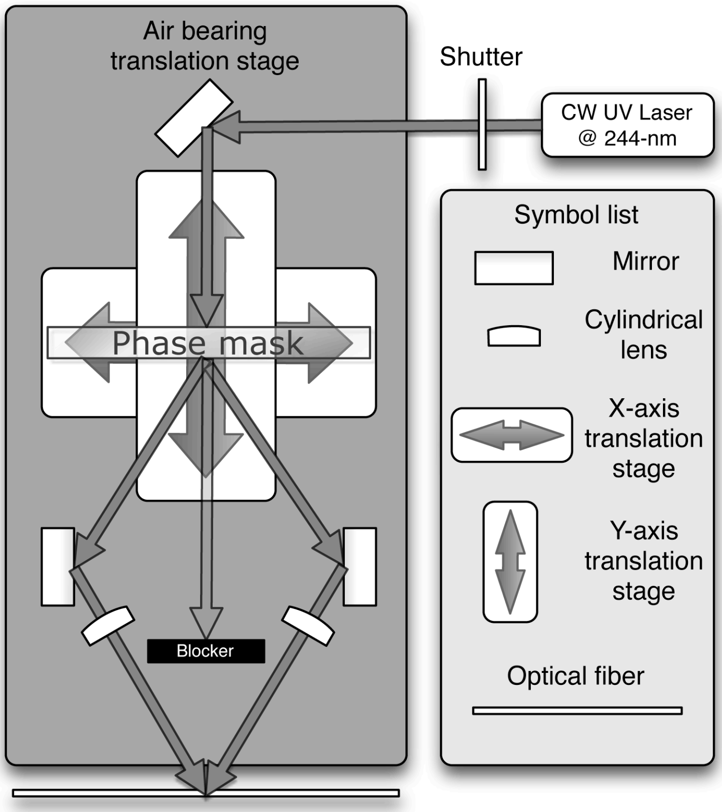

Fig. 3.1 A schematic diagram of the proposed FBG fabrication setup.

A continuous wave (CW) Argon ion laser (INNOVA Sabre MOTOFRED from Coherence Inc.) operating at the wavelength of 244-nm with 4-mm coherent length is used as a writing beam. The spot size of the beam is ~1-mm. The laser power is very stable with better than ±1% power variation. The laser power is specified at

500-mW. A phase mask with a pitch of 1070.6-nm made by holographic pattern technique from Ibsen is used for splitting the writing beam into two beams with half mutual angle of ~ 13.2° in air. The phase mask is mounted on top of two high precision piezoelectric transducers (PZTs) from Physik Instrumente. The two PZTs are used for controlling the X-axis and Y-axis positions of the phase mask. The X-axis and Y-axis PZTs have 0.03-nm and 2.5-nm resolution and maximum range of travel of 12-μm and 1500-μm, respectively. The two linear translation stages are controlled by a state-of-the-art controller, which offers integrated, low-noise power amplifier and improves the positioning accuracy to 0.001% of its travel range. The X-axis PZT controls the apodisation profile or the phase shift of the grating; meanwhile the Y-axis PZT together with a pair of mirrors and cylindrical lenses control the chirp rate or tune the peak wavelength.

The blocker is for blocking the zero-order UV beam from the phase mask. Typically, the zero order of the phase mask is ~1%. The two mirrors then reflect the ±1 order diffractions of the laser beam to the cylindrical lenses. The points of incidence of the ±1 order beams hitting the mirrors change when the phase mask is moved by the Y-axis PZT. Subsequently, the beams incidence on the cylindrical lenses slightly displaced parallel to their optical axes. The fibre is placed at the focus of the two cylindrical lenses. The mutual angle of the two beams at the fibre is changed if the beams hit different parts of the cylindrical lenses, but the beam focused position on the fibre is not changed. To fabricate a non-chirped FBG, the beams pass through the lenses are maintained at a fixed mutual angle.

3.3 Operation

In this setup, an FBG is fabricated by a so-called translate-and-write method. In the simplest case, a uniform grating of different lengths can be written by moving the air-bearing translation stage by multiples of the phase mask's grating pitch, Λ. When the shutter is off, the air-bearing translation stage moves the interferometer to the next desired position. After allowing sometime for stabilization, typically 700~1300-ms, the shutter is switched on and the translation stage holds its position to write the grating. The proportional amount of time used for writing exposure with this approach is extremely high compare to other translation-and-write methods, and can be controlled by the exposure time on each writing position.

The principle of operation is straight forward. However, the implementation of this approach is extremely challenging in practice. It is very difficult for the air-bearing translation stage to hold its position with nanometer accuracy during the FBG writing period. That is the main reason that other methods use constant velocity while synchronizing the shutter for the purpose of minimizing the stitching errors during writing [5], [17]. Keeping the position of the stage with an accuracy as small as ± ~3-nm is impossible without proper environmental isolation and fine-tuning of the air-bearing translation stage. The accuracy of the air-bearing translation stage is heavily relied on the interferometer encoder, which is used for measuring the distance of the translation stage. Using the 0.3-nm resolution air-bearing translation state, it could in theory provide sufficient positional accuracy for writing gratings with negligible stitching error. Any disturbance to the optical path of the interferometer encoder, however, contributes to instability for holding the position. We improved the stability by isolating the environment to minimize disruption to the setup. Environmental control is the key to keep the air-bearing translation stage working at optimum condition. Proper PID tuning and airflow rate supply to the translation stage also help in stabilizing the stage. After tuning, the stage can stabilize at a position within ± 1-nm for 90% of time within one hour, meanwhile error falls in the range of ±3-nm for the remaining 10% of the time. To isolate the writing environment instead of the entire room, we designed and made a shelf shown in Fig. 3.2. to cover the whole setup. The shelf can be lifted up using two compressed air cylinders. The frames are made by aluminum alloy. Acrylics used for UV protection are inserted in the frame. The whole shelf ensures that the environment is sealed completely during it is writing.

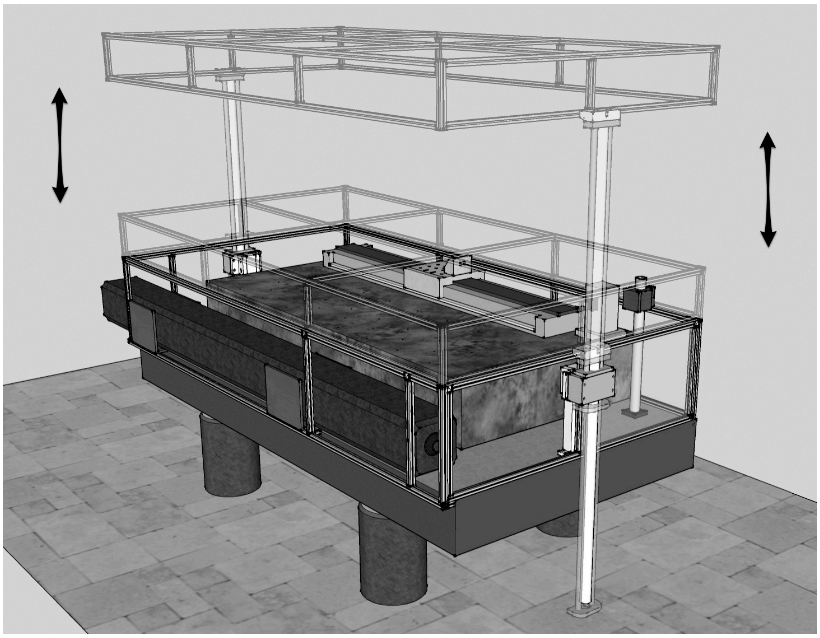

Fig. 3.2. An illustration of the shelf for isolation of the writing environment.

The ultra high stability allows a simple, direct and efficient fundamental approach to write high flexible designed FBGs.

In general, to write high quality FBGs, a CW laser is preferred [17]. There are a number of reasons for using a CW laser over a pulse laser. The power stability of pulse lasers is usually worse than that of CW lasers. The fluctuation of output power of a typical pulse laser is usually larger than 3% from pulse to pulse. This causes a large amplitude fluctuation along the grating. Another problem of pulse lasers is the pulse jittering. It results in serious phase errors in the grating. In addition, the peak power of pulse laser is much higher and it significantly reduces the mechanical strength of the fibre [19]. A high mechanical strength is crucial for most FBG sensing applications.

However, using CW laser as writing beam is challenging. Any undesired vibrations in the setup during writing to fibre accumulate the phase error. In normal case, the period of the grating is ~535-nm for a grating in C-band. If there is a relative movement corresponding to π phase shift (267.5-nm) in the grating, the grating can be completely erased. The positional error within ±3-nm is acceptable. In our setup, over 99% of the time (measured over 20 hours), the error is within ±3-nm centered at the given position.

The proposed setup not only presents an easier and more efficient way to fabricate FBGs, but also offers flexibility in phase control, which allows arbitrary FBG fabrication, including phase-shift gratings, apodised gratings, and chirped gratings.

The X-axis PZT and a small incremental adjustment of the air-bearing translation stage control the local phase in the grating. In the ideal case, the local phase of the grating during fabrication depends only on the position of the phase mask. This assumes that there is no vibration, no temperature difference among the components that affects the optical paths between the phase mask and the fibre, and no air current moving in the optical paths. The pitch of the phase mask, Λ_{pm} is fixed. The local phase of the grating can be controlled by the position of the phase mask. For example, by moving the X-axis PZT with half of Λ_{pm}, i.e. 535.3-nm in our case, a π phase shift can be produced. A phase shift can also be added by moving the air-bearing translation stage. The advantage of using the PZT instead of the air-bearing translation stage is that its step response time is fast. With the ability to change phase along the grating, apodised FBGs can be fabricated.

3.4 Chirp rate control

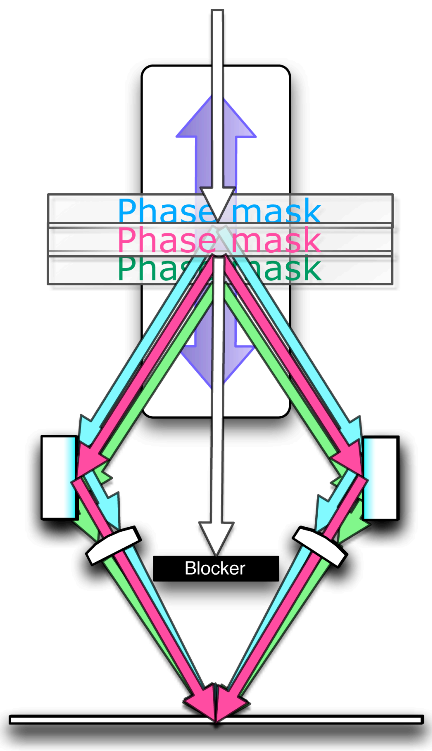

Fig. 3.3 An illustration of the principle of the grating's pitch changed by the mutual angle of the interference beams. The different colours indicate the different positions of the phase mask.

One of the major benefits of this setup is the ability to control the chirp rate of the grating with a simple Y-axis control. The operation principle is illustrated in Fig 3.3. The fibre is placed in the focus point of the two beams. The pitch of the grating, Λ, inside the core is determined by the mutual angles of the two beams and is described by

$$\Lambda = \frac{\lambda_{uv}}{2\sin\frac{\theta_{air}}{2}}, \tag{3.2.1}$$

where λ_{uv} is the wavelength of the UV writing beam, and θ_{air} is the mutual angle of the interference beams. The Bragg wavelength is proportional to the effective refractive index and the pitch, Λ. By tuning the Bragg wavelength slightly during the fabrication, chirp rate can be changed as long as the focal plane of the interference does not change.

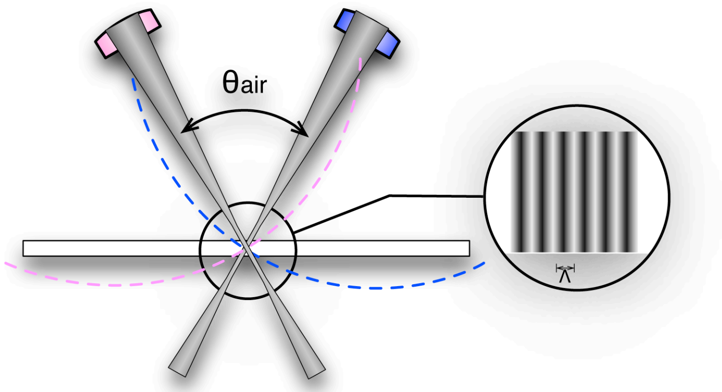

Fig. 3.4 Detailed illustration about the lenses and beams. The intersection of the dash lines shows the focus for the writing beams.

Three cases (shown in purple, green and blue) with the phase mask at three different vertical positions are illustrated in Fig. 3.3. The purple arrow shows the path that passes though the centre of the cylindrical lens, and the green and blue represent the extreme cases, corresponding to the minimum and maximum wavelengths, respectively. Figure 3.4 illustrate the writing beams after passing though the two cylindrical lenses. The relationship of the Bragg wavelength is given by:

$$\lambda_B = \frac{n_{eff}\lambda_{uv}}{\sin\frac{\theta_{air}}{2}}. \tag{3.2.2}$$

The smaller the mutual angle, the larger the wavelength can be obtained. The cylindrical lenses are placed in such a way that the beams are focused at the core of the fibre. The beams focused on the same spot even when they are displaced from the optical axis of the cylindrical lenses. It allows the change of λ_B, or, in the other words, change in chirp rate during the writing process without the need of re-positioning the fibre vertically. The illustration and calculated results are shown in Fig.3.4. In the design, the θ_{air} allows the maximum changes of ~±0.06˚, providing ~11.5-nm of wavelength tuning range. Fig. 3.5 (c) illustrates the schematic diagram of the control principle of the Bragg wavelength. The focal length of the cylindrical lenses was 270-mm. The corresponding calculated maximum deviation of half mutual angle is ~0.1˚.

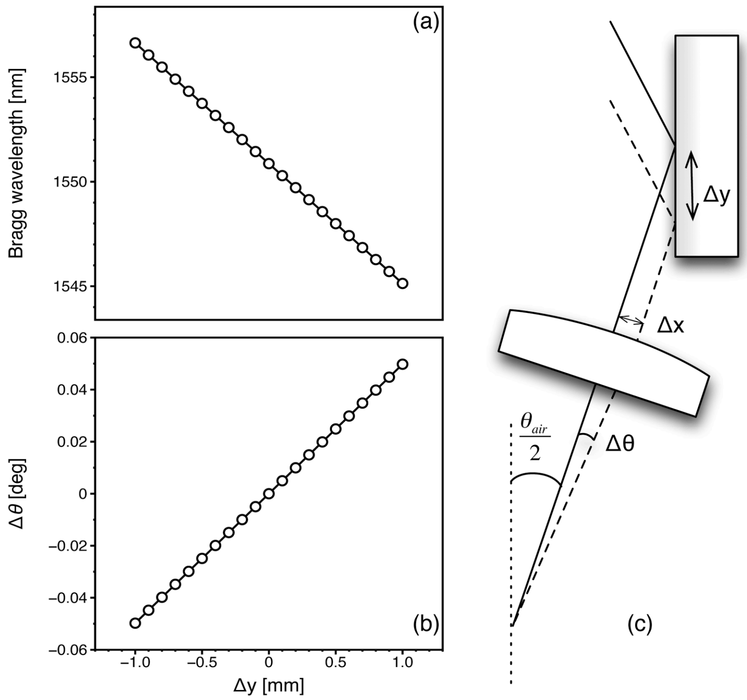

Fig. 3.5 (a) Bragg wavelength against the change of vertical position of the phase mask, Δy. (b) $\Delta\theta$ against Δy (c) illustration of controlling Bragg wavelength.

The operation principle for making phase shift and chirped FBG has been introduced. The two parameters can be controlled and tuned independently. However, the overall performance relies heavily on the accuracy of the alignments of the components. In our setup, the positions of the two mirrors are fixed.

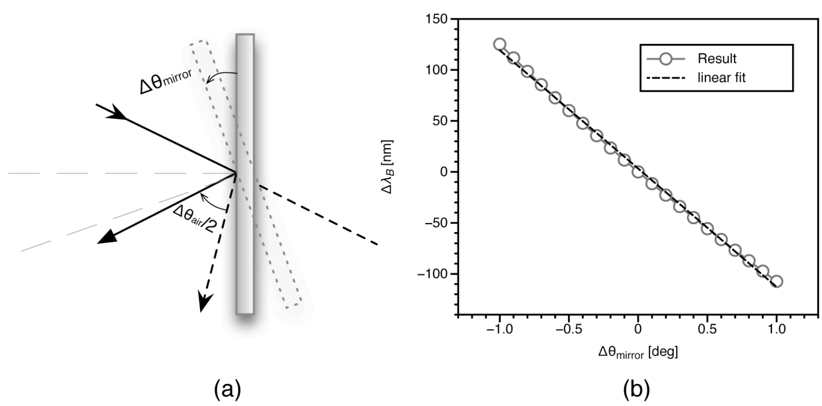

Fig. 3.6 (a) Illustration of the deviation of angles of the mirrors and the change of the half mutual angle of the interference. (b) Deviation of Bragg wavelength against the deviation of the angle of the mirror.

The Bragg wavelength of the grating is very sensitive to the angles of deviations of the mirrors. Fig. 3.6(a) illustrates the situation when the mirrors accidentally moved slightly. The sensitivity is about 116-nm per degree, assuming the angles changes symmetrically. Since the alignment is sensitive, the mirrors have to be mounted solidly and no adjustable mount is used. In addition, highly stable environment is also required. Fig. 3.7 shows the position error.

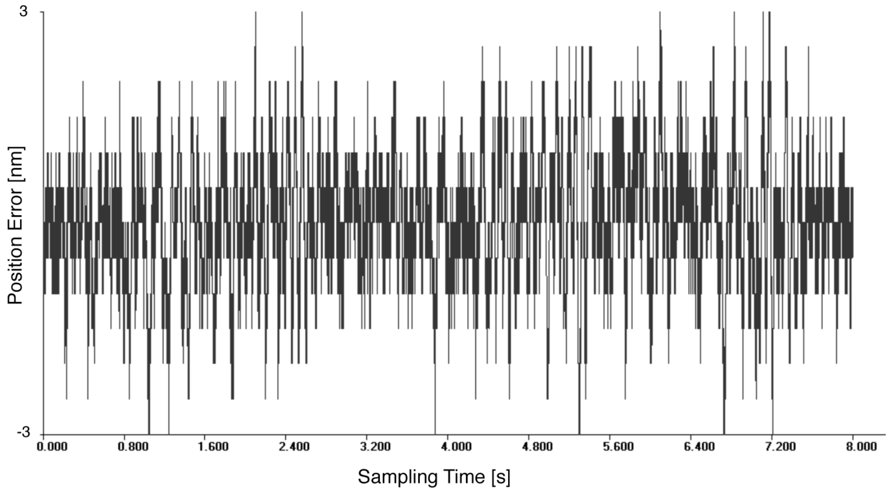

Fig. 3.7. The position error of the air bearing translation stage.

The error was measured by the software package, NScope, which is used for tuning the control parameters of the translation stage from Aerotech. The units of Y-axis and X-axis are nanometers and seconds, respectively. The position error was sampled at 1 kHz for 8 seconds. In order to examine its stability, the position error was measured with a laser interferometer encoder (Renishaw's Model RL10). Stability over long duration was also measured. 80.56%, 99.31%, and 99.56% of the error fell in the range of ≤±1-nm, ≤±3-nm and <±5-nm, respectively. The raw data was sampled at 1-kHz and measured over 20 hours. Greater than 99% of the time, the air-bearing stage stays at its position with its stability better than to ±3-nm which allows sufficient stability for writing long and highly complex FBGs.

3.3 Software control

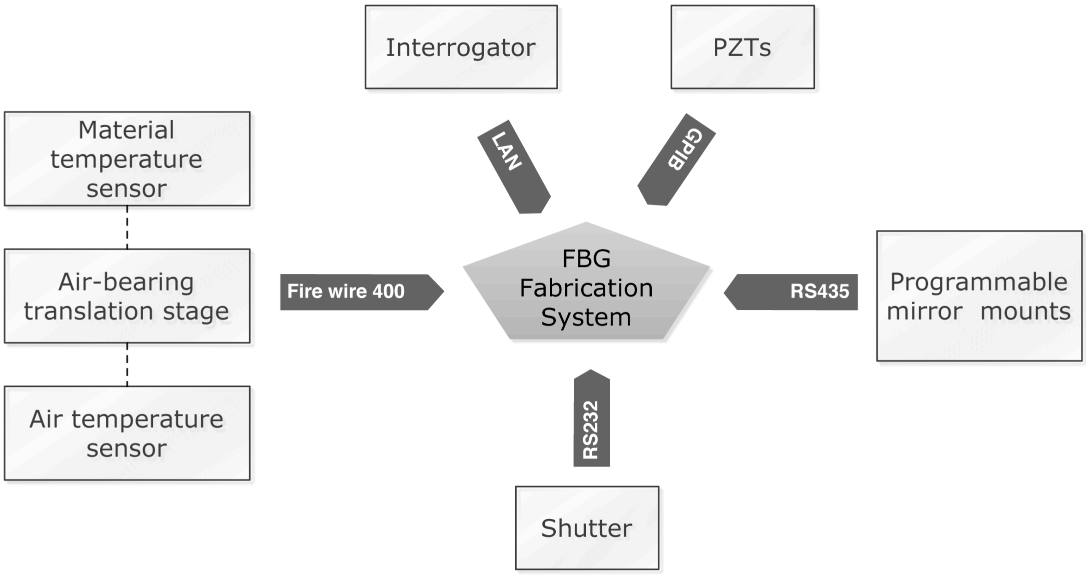

Fig. 3.8 Hardware connected to the fibre Bragg grating fabrication system that is controlled by Labview™. The arrows indicate the interfaces connected to the computer from the hardware.

The software developed in this project is the brain of the novel fibre Bragg grating fabrication system. It integrates and synchronizes all the hardware to perform a task, i.e. to fabricate FBGs of arbitrary spectral characteristics. Figure 3.8 shows all the hardware connected to the fabrication system. The hardware are integrated using Labview™. The main advantage using Labview is that it allows relatively easy software control of instruments with a graphical interface. Components or instruments from various companies used different interfaces (connection bus). Most of them require software drivers to recognize them and communicate with them. A lot of companies offer Labview compatible drivers and Labview library as a tool package to control the hardware products. This simplifies the software program development time.

3.3.1 The main workflow

In order to fabricate gratings as designed, various steps need to be performed during the grating fabrication process.

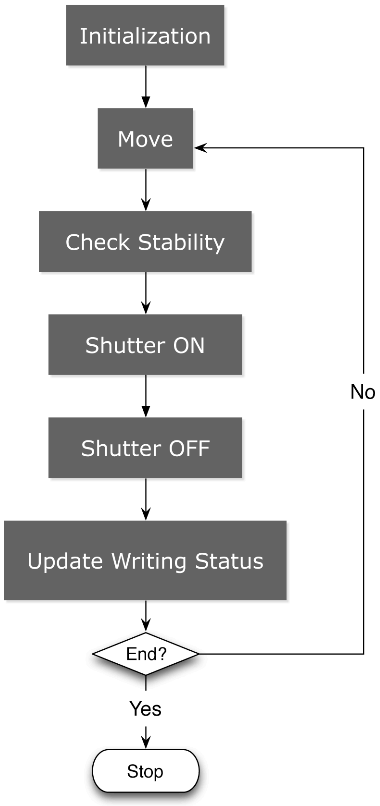

Fig. 3.9 The overall workflow for writing an arbitrary fibre Bragg grating.

Figure 3.9 shows the workflow of the software to run the writing tasks. The main program first initializes the hardware settings and the designated grating profile. The program then enters to the Move module. Its main task is to move the air-bear translation stage and the PZTs to the desired position(s). When the stage(s) reach the target position, it checks whether the stages are stabilized at the position for a certain period of time. If it is stabilized, the shutter switches on for the desired exposure time and then off. After that, the status is updated and if the writing is not finished, the iteration starts over from module "Move" again until the writing is complete.

In the initialization phase, there are two main parts. First, it initializes the settings of all the external hardware if needed. Second, it generates the grating profile and then converts it to the position arrays for the translation stage's movement.

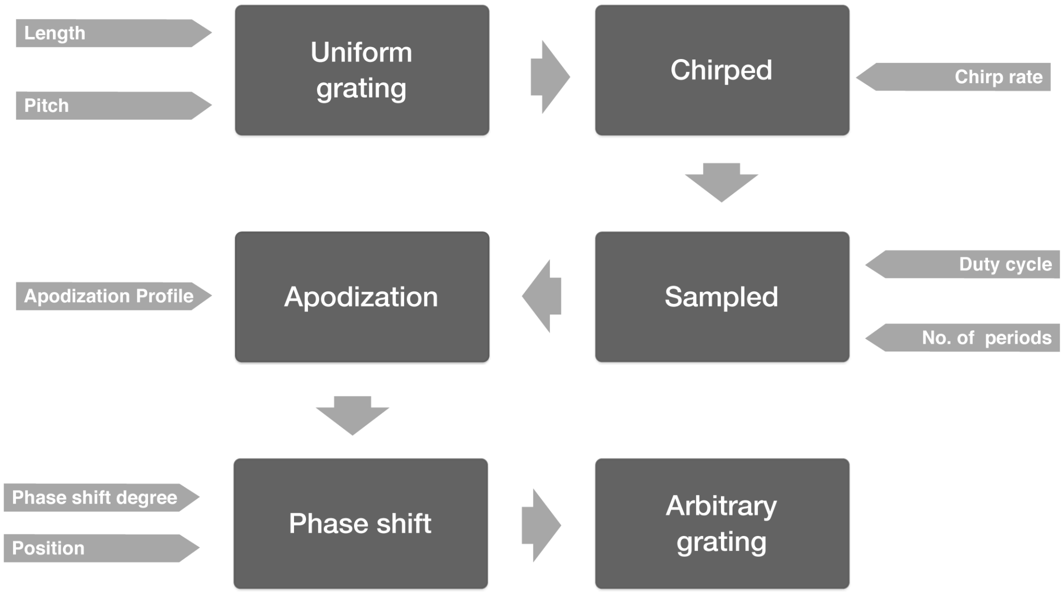

Fig. 3.10 The workflow for generating the design grating profile for writing and simulation.

Figure 3.10 shows the workflow for generating the grating profile. An arbitrary grating consists of a uniform profile as a framework, chirped characteristics, sampled profile, apodisation profile and the phase shift information. In each phase, the parameters input to the module and output to become two arrays. The first array stores the positions and the second stores the designed refractive index modulation at its corresponding position. The arrays are modified correspondingly at each phase by inputting the design parameters. The input design parameters are illustrated by the gray arrows. The rounded rectangular box represents the module for the part to generate the grating profile.

After passing though the initialisation module, the grating profile is generated and enters the "Move" module. This module converts the grating profile to the position commands, which are for the translation stages to move. This approach is clear and well organized and so easy to implement. Some modules are coded for conversion purposes. They are written for converting

- the design phase shift to the target position according to the design wavelength,
- apodisation amplitude to the required phase shift,
- the sampling grating's (structure grating's) duty cycle to the "true" or "false" writing commands,
- and the chirp rate to the incremental or decremental positions for the pitch at the corresponding

Some tasks running in background are to acquire information to monitor the system operation.

3.3.2 Background modules

There are two modules that get the positions of the air bearing translation stage and PZTs every 1-ms and one module is to get the spectrum from the interrogator every second. The sampling rates are the highest that can be achieved with the PZTs and interrogator and the modules always running in the background. When the main program needs the information, the system will send the query to get the information it need. The background modules are set to a lower priority to operate.

There is a software code that analyses the stability of the system by inputting the feedback of the laser interferometric encoder and the temperature information. The computer used has a quad-core CPU and over clocked to 3.5-GHz from 2.66-GHz. The code for the main task used to write gratings are designed to run only by the primary core which is not occupied by any other tasks. It ensures that the main task is always running at the highest priority and not interrupted. For the tasks running in the background or any other tasks that have lower priority was assigned to the cores that are not handling the main task.

There are some modules that are not always running but the main program will call them when needed. They are:

a. mirrors alignments

b. grating profile generation

c. initialization process

d. testing modules for each part to function

e. transfer matrix simulation

3.4 Results

3.4.1 Long FBG

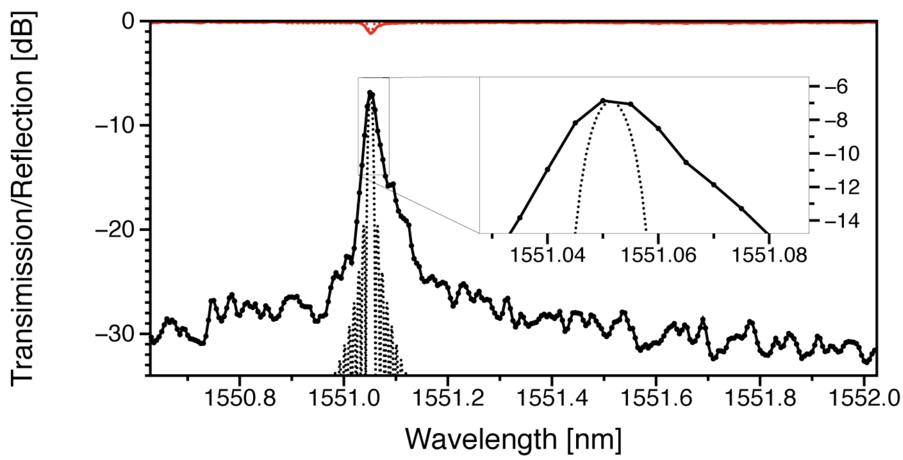

Fig. 3.11 Spectra of a 90-mm long uniform fibre Bragg grating.

Figure 3.11 shows the transmission and reflection spectrum of a 90-mm long uniform FBG. The peak wavelength is 1551.05-nm with ≤15-pm of -3-dB bandwidth. The spectrum of the grating was measured by an MOI interrogator (model SM-125) with the resolution of 5-pm. The laser power was 60-mW with ~1-mm beam spot size. The designed grating period, Λ, was 535.155-nm. The dash lines show the simulated spectra. The FBG was fabricated by simple translate-and-write method. When the air-bearing stage was holding at the initial position, the shutter opened and the laser beams focused at the core of the fibre for three seconds of exposure time. The translation stage then move to 100 times of its pitch, i.e. ~53.5-µm, and then hold its position for a few hundreds of milliseconds in order to ensure the vibration is minimal during seeking for new location, and the shutter was switched on again at this new position. The grating was scanned once for a travel length of 90-mm.

The fabrication of long length FBG has been a challenging problem for most FBG fabrication techniques. The standard phase mask technique is the most commonly used for writing gratings. The length of the phase mask limits the grating length. There are two sophisticated techniques for making phase masks. With the phase mask made by the electron beam technique, there are phase errors where e-beam fields are stitched together. The resultant grating suffers large stitching errors. Phase masks made by holographic exposure are much better in minimizing phase errors. However, the cost for such long phase mask is very high especially when they have to be made for each grating wavelength.

There are three difficulties for fabricating long FBGs. Two main problems are nanoscopic scale vibrations and temperature fluctuations during the long period of fabrication time. These two issues can be minimized by the isolation of the environment for the whole writing facilities. Furthermore, optical alignments and mechanical designs are very critical. The whole setup including the air-bearing translation stage and the fibre holder platform is mounted on a 1.5-ton granite. Under the granite, there are four rubber spacers to absorb vibration from the ground. The granite is placed on top of Tuned-Damped Field smart table (Newport ST-U2 Series). The table measures the high frequency vibration and actively cancels the noise with a built-in damper. Stitching error depends strongly on vibrations at any part of the system in an interferometer setup like ours. The alignment of the optical path also plays a critical role.

3.4.2 Chirped grating

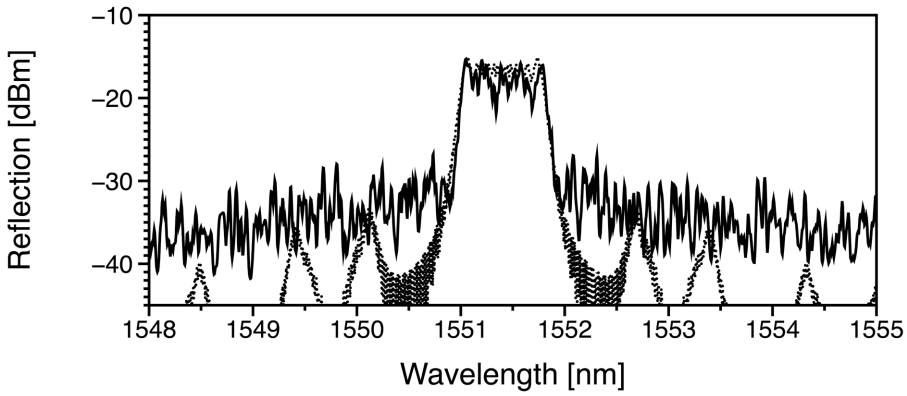

Fig. 3.12. Reflection spectrum of a 50-mm long chirped grating. The dash line is the simulated result.

The result of a 50-mm long linear chirped grating is demonstrated in Fig. 3.12. The dash line shows the simulated result. The chirped rate was 0.15-nm/mm. The exposure time was 3 seconds for one step. One translation step was 20 times of its pitch. This step changes along the fibre as local Bragg wavelength is adjusted by the Y-axis stage.

3.5 Chapter Summary

A novel FBG fabrication setup is proposed. The system combines state-of-the-art equipment including laser, PZTs and air-bearing translation stages, with simplicity of independent controls of local Bragg wavelength, phase and apodisation for the fabrication of FBGs of arbitrary spectral characterisitics. The working principle and the software implementation of the system are described. Some important challenges and their solutions are discussed. This chapter reports two grating results. The fabrication of a 90-mm long FBG with -3dB bandwidth of less than 15-pm and a 50-mm long chirped FBG with 0.15-nm/mm chirped rates were demonstrated. With the new ability to control phase, apodisation and local Bragg wavelength, a variety of sophisticated FBGs can be fabricated, potentially opening up many new applications which required FBGs with complicated spectral characterisitcs that are difficult to fabricated.

Reference

[1] K. O. Hill, Y. Fujii, D. C. Johnson, and B. S. Kawasaki, "Photosensitivity in Optical Fiber Waveguides - Application to Reflection Filter Fabrication," *Applied Physics Letters*, vol. 32, no. 10, pp. 647–649, 1978.

[2] G. Meltz, W. W. Morey, and W. H. Glenn, "Formation of Bragg Gratings in Optical Fibers by a Transverse Holographic Method," *Opt. Lett.*, vol. 14, no. 15, pp. 823–825, Aug. 1989.

[3] G. D. Marshall, R. J. Williams, N. Jovanovic, M. J. Steel, and M. J. Withford, “Point-by-point written fiber-Bragg gratings and their application in complex grating designs,” *Optics Express*, vol. 18, no. 19, pp. 19844–19859, Sep. 2010.

[4] Y. S. Liu, L. Dong, J. J. Pan, and C. Gu, “Strong phase-controlled fiber Bragg gratings for dispersion compensation,” *Opt. Lett.*, vol. 28, no. 10, pp. 786–788, May. 2003.

[5] M. Gagné, L. Bojor, R. Maciejko, and R. Kashyap, “Novel custom fiber Bragg grating fabrication technique based on push-pull phase shifting interferometry,” *Optics Express*, vol. 16, no. 26, p. 21550, 2008.

[6] M. Ibsen, M. K. Durkin, M. J. Cole, and R. I. Laming, “Sinc-sampled fiber Bragg gratings for identical multiple wavelength operation,” *IEEE Photonics Technology Letters*, vol. 10, no. 6, pp. 842–844, Jun. 1998.

[7] A. Othonos and K. Kalli, *Fiber Bragg gratings*. Artech House Publishers, 1999.

[8] R. Kashyap, *Fiber Bragg Gratings*. Academic Press, 2009.

[9] D. Z. Anderson, V. Mizrahi, T. Erdogan, and A. E. White, “Production of in-fibre gratings using a diffractive optical element,” *Electronics Letters*, vol. 29, no. 6, pp. 566–568, 1993.

[10] Y. Qiu, Y. L. Sheng, and C. Beaulieu, “Optimal phase mask for fiber Bragg grating fabrication,” *Journal of Lightwave Technology*, vol. 17, no. 11, pp. 2366–2370, Nov. 1999.

[11] P. Dyer, R. Farley, and R. Giedl, “Analysis of Grating Formation with Excimer-Laser Irradiated Phase Masks,” *Optics Communications*, vol. 115, pp. 327–334, 1995.

[12] L. Poladian, “Simple grating synthesis algorithm,” *Optics Letters*, vol. 25, no. 11, pp. 787–789, Jun. 2000.

[13] J. Skaar, L. G. Wang, and T. Erdogan, “On the synthesis of fiber Bragg gratings by layer peeling,” *IEEE Journal of Quantum Electronics*, vol. 37, no. 2, pp. 165–173, Feb. 2001.

[14] H. P. Li and Y. L. Sheng, “Direct design of multichannel fiber Bragg grating with discrete layer-peeling algorithm,” *IEEE Photonics Technology Letters*, vol. 15, no. 9, pp. 1252–1254, Sep. 2003.

[15] L. Dong and S. Fortier, “Formulation of time-domain algorithm for fiber Bragg grating simulation and reconstruction,” *Quantum Electronics, IEEE Journal of*, vol. 40, no. 8, pp. 1087–1098, Aug. 2004.

[16] R. Feced, M. N. Zervas, and M. A. Muriel, “An efficient inverse scattering algorithm for the design of nonuniform fiber Bragg gratings,” *IEEE Journal of Quantum Electronics*, vol. 35, no. 8, pp. 1105–1115, Aug. 1999.

[17] Y. Liu, J. J. Pan, and C. Gu, “Novel fiber Bragg grating fabrication method with high-precision phase control,” *Optical Engineering*, vol. 43, no. 8, pp. 1916–1922, Aug. 2004.

[18] H. P. Li, M. Li, Y. L. Sheng, and J. E. Rothenberg, “Advances in the design and fabrication of high-channel-count fiber Bragg gratings,” *Journal of Lightwave Technology*, vol. 25, no. 9, pp. 2739–2750, Sep. 2007.

[19] M. Nakamura et al., “Evolution of optical fiber temperature during fiber Bragg grating fabrication using KrF excimer laser,” *Japanese Journal of Applied Physics Part 1-Regular Papers Short Notes & Review Papers*, vol. 43, no. 1, pp. 147–151, Jan. 2004.

Chapter 4

Microfibre Bragg grating

4.1 Introduction

Fibre Bragg grating can be imprinted in any photosensitive fibre optical fibres. By combining the characteristics of the grating and the optical waveguide, it may have unique features that can improve the current technology or find some new applications. Microfibre is a new class of optical fibre that is fabricated by a tapering.

Tapering of optical fibres is a very important process to fabricate some crucial optical fibre devices such as directional couplers. Various tapering techniques were intensively studied in the late 1980s and the early 1990s [1-5]. In 2003, Tong et al employed a novel tapering technique to fabricate nanowires from standard single mode optical fibres tapered down to a few hundreds nanometers [6], [7]. The core diameter of the fibre is so small that the optical propagation field spreads out to the cladding and is thus guided by the silica and air. The evolution of modes in microfibres in the diameters ranged from 8 to 35-μm was reported by Fielding et al [8] to study the mode patterns for different microfibre diameters and demonstrated experimentally that the optical guiding becomes multimode.

Recently, fibre Bragg gratings (FBGs) inscribed in microfibres using different lasers have been reported [9-12]. Microfibre Bragg gratings (MFBGs) fabricated by femtosecond laser pulses [9], KrF excimer laser [10] and 193-nm laser [11] were investigated for RI sensing, and liquid level variation sensing [12]. It is important to note that MFBGs exhibit multiple peaks [9-11] as the diameters of the microfibre was too large to ensure single mode propagation. The multi-mode characteristic is not desirable for demodulation and demultiplexing and thus limits its application.

In this preject, we report a technique to re-couple the fundamental mode reflected from a MFBG and couple the higher order LP_{0M} modes to the claddings via the fibre taper with an appropriate length. To the best of our knowledge, this is the first demonstrated technique to obtain effectively single reflection peak from an FBG written in a multi-mode microfibre. The main advantage of using such MFBGs is that the fibre diameter (30-μm in our work) is much larger than the single mode microfibre (typically ~1-μm) and thus easier to handle and fabricate.

4.2 Fabrication of microfibre

In the literature, microfibre or optical fibre nanowires are made by stretching a heated fibre, forming a structure comprising a uniform waist with microns or nanometers diameter and both ends connected to the transition regions. So far, three different techniques have been used.

1. The flame-brushing technique [1-3], [13],
2. The modified flame-brushing technique [14], [15].
3. Glass processing machine with tungsten filament (this work).

The flame-brushing technique is commonly used for making fibre tapers and couplers [1-3], [13]. A small flame heats an optical fibre that is being stretched from both ends. The heated area experiences a diameter decrease because of mass conservation. Controlling the stretching rate, the shape of the tapering region and the waist can be well defined.

The second fabrication method is a modified version of the flame-brushing technique in which the flame is replaced by a different heat source. Two types of heat source have been used: a sapphire capillary tube heated by a CO2 laser beam [14], and a graphite micro-heater [15].

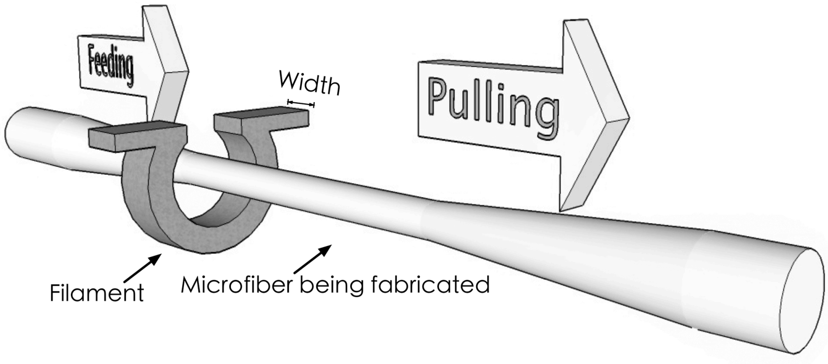

Fig. 4.1 An illustration of a tapering method for fabricating microfibre.

In our work, the microfibre was fabricated by a glass-processing machine made by Vytran (model GPX- 3400). An illustration of the tapering method of pulling conventional optical fibre into microfibre is shown in Fig. 4.1. The optical fibre with diameter of 125-μm is fed into the filament at the velocity of v_f and pulled from the opposite side of the filament at the velocity of v_p. Since the volume of the fibre entering and existing from the heating element remains constant, the diameter of the pulled fibre can be determined by the following relationship:

$$v_f = \frac{d_d^2}{d_f^2} \times v_p \tag{4.1}$$

where d_f and d_p are the diameters of the feeding and pulled fibre. In our experiment, v_p was set to a constant speed of 1-mm/s with initial delay of 0.1 second to allow the fibre to be heated up by the filament. By varying the feeding speed, tapers with the desired diameters can be made. The heating filament is made of tungsten and its operation temperature is greater than 1900˚C at an input electrical power of 29-W. The upside down Ω shape of the heating filament facilitates a uniform heating zone around the fibre being pulled. The interior loop diameter and width of the heating element are 0.035 and 0.025 inch, respectively. The fibre was placed at the center of the loop. During the pulling process, zero tension was applied and argon gas was supplied to the heating filament region at the flow rate of 0.65 L/min to prevent oxidation of the heating filament. Tungsten has a melting point of 3422°C but oxidizes at 400 to 500°C. The taper region was designed to be linear. Using this method, we could make microfibres with different taper and waist lengths, and diameter smaller than 1-μm.

4.3 Fibre Bragg grating inscription

A microfibre with a waist diameter of 30-μm and taper and waist lengths of 25-mm and 20-mm, respectively, was fabricated for our experiment. In order to enhance the taper's photosensitivity for FBG inscription, the optical fibre was hydrogen loaded at 25˚C for over 60 hours. A bend-insensitive G.657B optical fibre from Silitec which has high germanium concentration than SMF28 fibre, was used. Since the photosensitive core diameter (~2-μm) is very small, hydrogen diffuses out very fast [16], so the FBG inscription has to be made within 4-hour after the optical fibre was withdrawn from the hydrogen chamber. Fibre Bragg grating (FBG) was inscribed at the center of the taper waist as shown in Fig. 4.2.

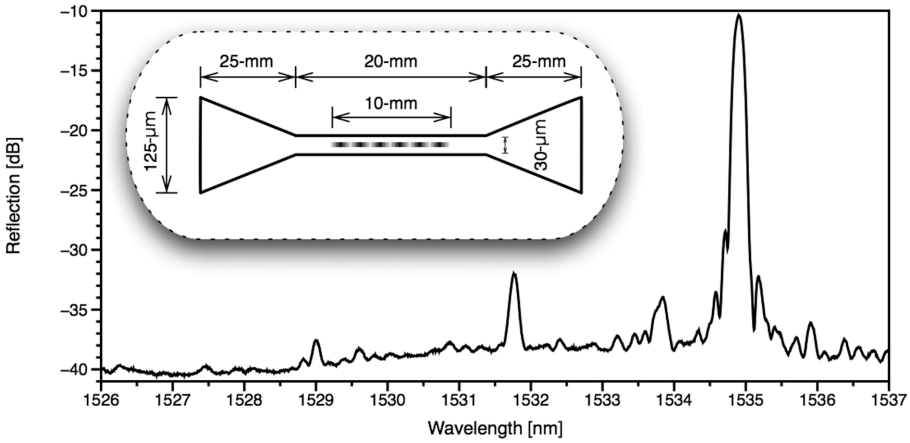

Fig. 4.2 Reflection spectrum of an effectively single reflective mode FBG written in the taper waist of a 30-μm microfibre. The inset shows the dimensions of the microfibre with an FBG inscribed at the waist center.

The FBG was fabricated using standard phase mask technique with a 1061.5-nm pitch phase mask. A KrF laser with wavelength of 248-nm and 2-mm beam width was used as the writing beam. The pulse energy and pulse rate of the laser were 13-mJ and 200-Hz, respectively. The reflection spectrum of an FBG written in the taper is shown in Fig. 4.2. The dimensions of the taper are also shown in the inset of Fig. 4.2. The length of the apodised FBG is 10-mm long. The apodisation profile was achieved by scanning the writing beam along 8- mm at the taper waist using a hamming profile with maximum velocity of 5-mm/s. The grating spectrum was measured by an interrogator (model SM-125 from Micron Optic, Inc.) which has a 5-pm resolution. The peak wavelength and 3-dB bandwidth of the FBG are 1534.895-nm and 0.135-nm, respectively. The reflection of the MFBG was slightly less than 10%. The reflections of the other modes are significantly weaker than the main peak and have only 0.1% or - 30-dB reflection. Reflections of the higher order modes are at least 20-dB smaller than the fundamental mode, making it an effectively single mode FBG. The dynamic range of most commercial FBG interrogators for sensing applications are not enough to demodulate the reflection signal with 30-dB signal loss. In other words, our MFBG are effectively single reflective mode.

4.4 Multi-mode characteristic of microfibre

To analyze the FBG in the microfibre, we consider the V-number of the microfibre. For conventional optical fibre, the V-number is obtained by the following equation:

$$V = \frac{2\pi a}{\lambda}\sqrt{n_1^2 - n_2^2}, \tag{4.2}$$

where a is the core radius, and n_1 and n_2 are the refractive indices of the core and cladding, respectively. The waist of the taper has a diameter of 30-μm. Since the core diameter, ~2-μm, is significantly smaller than the mode field diameter, the optical field is no longer bounded by the core but rather by the 30-μm cladding [7]. Using a = 15-μm and n_1 = 1.444 and n_2 = 1, the V-number was calculated to be ~64. Therefore, the FBG written in the microfibre supports many modes. It should be noted that the LP mode approximation cannot be applied here because the microfiber is no longer "weakly guiding" as n_1-n_2 is 0.44 and thus not significantly smaller than 1.

The coupling between the different modes of an FBG written on a multimode optical fibre was reported [17]. There are two conditions that have to be satisfied for the mode coupling in an FBG. First, the overlay of coupling coefficient has to be large enough. Since the diameter of the FBG is very small, small amount of power in the modes HE_{1M} & EH_{1M} are guided within the core while TE and TM modes almost have zero power in the core. As a result, MFBG cannot couple those modes. The other higher order HE modes, e.g. HE_{2M} and HE_{3M}, also have zero coupling coefficients between forward HE_{1M} modes. Therefore, they cannot be coupled to HE_{1M}. The second condition is that the mode coupling has to satisfy the phase matching condition. Since different modes have different propagation constants, the phase matching wavelength is different. In the general case, the Bragg wavelength of the mode coupling from mode A to mode B is given by the equation:

$$\lambda_{A\rightarrow B} = (n_A + n_B)\Lambda = 2n_{eff}\Lambda, \tag{4.3}$$

where n_A and n_B are the effective refractive indices of mode A and B, respectively, and Λ is the pitch of the grating.

4.5 Fibre Bragg grating in a few-mode microfibre

Figure 4.3 (a) illustrates the mechanism of the mode coupling in the taper from an FBG written in the microfibre. The taper length between the 125-μm diameter standard fibre and the 30-μm diameter microfibre is 5-mm. Figure 4.3 (b) shows the reflection spectrum of an FBG written in the 30-μm microfibre.

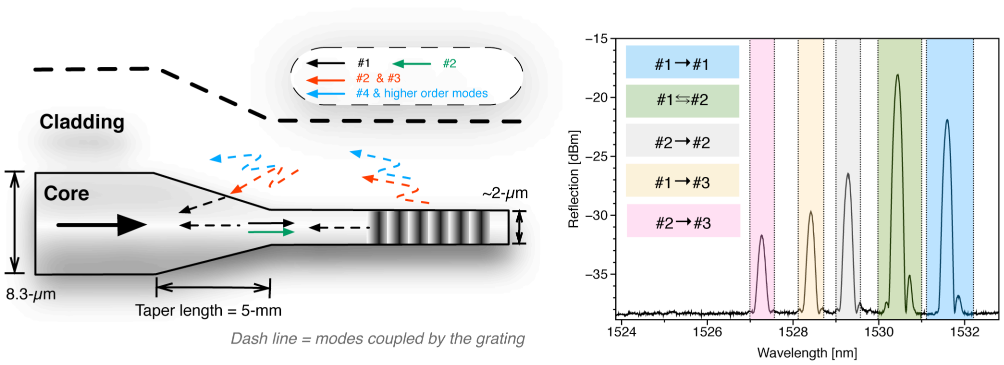

Label	Mode	n_{eff}
#1	HE_{11}	1.443618
#2	HE_{12}	1.441479
#3	EH_{12} & HE_{13}	1.437574 &1.437458
#4	EH_{13}	1.431801

(c)

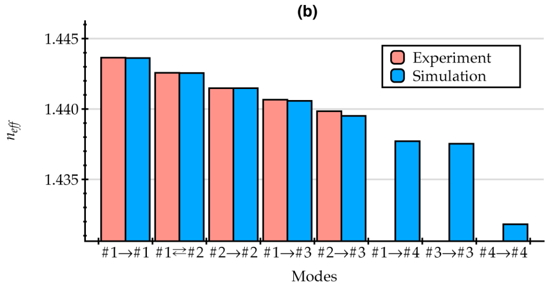

Fig. 4.3. (a) Illustration of the mode coupling of an FBG written in the waist of a taper. The dimensions of the fibre taper are also indicated. (b) Measured reflection spectrum of the grating. (c) A table listing the simulated n_{eff} of modes having power guided within the

core and the corresponding labels for the mode. (d) Simulated and experimental results of n_{eff} of modes coupling in the MFBG

Figure 4.3 (c) shows a table listing the labels, the corresponding modes which have power guided in the core and the simulated n_{eff} using COMSOL. It should be noted that EH_{11} mode (with n = 1.44161) has zero power guided within the core and thus it is not shown in the table. In addition, the n_{eff} of EH_{12} and HE_{13} are very close to each other and hence they are grouped as #3. The label of the modes in the table will be used throughout the paper for clarity. Figure 4.3 (a) illustrates the mode coupling mechanism of the grating device. The coupling of the modes can happen as follows. At first, fundamental mode is launched to the taper device (indicated by the big black arrow in Fig. 4.3 (a), and then higher order modes are excited in the taper region (illustrated by two small arrows). The modes are then coupled backwards by the MFBG. The coupling is not only limited by the self-coupling, e.g. #1 → #1, but also occurs mutually, e.g. #1→ #2 and #1 → #3. The resulted n_{eff} can be obtained by Eq. (4.3). At last, the reflected modes from the MFBG are re-coupled by the taper into the fundamental mode. Even if the modes are eventually re-coupled to the fundamental mode, they appear as several peaks because the n_{eff} of the modes are different as the result of the coupling in the MFBG.

Figure 4.3 (b) shows the reflection spectrum of an FBG written in the 30-μm microfiber. When the fundamental mode passes though the taper region, higher orders modes are also excited. The MFBG couples the forward #1 and #2 mode to backward #1, #2, and #3 modes, and then these three modes are re-coupled back to backward #1 via the linear shaped taper region. In addition to these three modes, other higher order modes (higher than #3) which are also coupled from forward #1 or #2 mode and annotated by blue arrow, are reflected and coupled to the cladding and eventually lost.

The length of the taper determines the number of modes recoupled into the single-mode fiber via the taper. From taper end, only #1 couples backwards to the single mode fiber.

There are five peaks in the reflection spectrum shown in Fig. 4.3 (b). The peaks are highlighted in different colors. The corresponding modes with same color are indicated on the left side of the spectrum. The first peak, located at the longest wavelength, was a result of forward #1 to backward #1. The second peak has the highest reflection power and it was a consequence of #1 and #2 mutual coupling, *i.e.* #1→#2 and #2 →#1. The third peak was the result of self-coupling of #2. The fourth and last peaks were the coupling result of #1→#3 and #2→#3, respectively. In the microfiber, only the modes from #1 and #2 were re-coupled to the core via the taper and therefore no reflection aroused from coupling of the other higher order modes. That is #3→#1, #3→#2, #3→#3, and etc.

Figure 4.3 (d) shows the comparison between the simulated mode refractive index and the n_{eff} obtained from experiment. A three layers model of the step index profile was used. The refractive indices of the core, cladding and air were set to 1.44998, 1.44402, and 1, respectively. The diameters of the core, cladding and air were 1.992 (converted from 8.3μm core diameter as in original fiber specification: 8.3*30/125 = 1.992-μm), 30 and 1000-μm (large enough to treat as infinity), respectively. The effective refractive indices resulted from the corresponding coupling modes in the MFBG were then calculated using Eq. (4.3). The results are in excellent agreement with each other. It should be noted that other higher order modes (EH_{1M} & HE_{1M} where $M \geq 3$) theoretically can also be coupled as they also have some power guided in the core; however, their mode refractive indices are far from 1.44 and therefore cannot be coupled to the taper.

4.6 Single reflective mode microfibre Bragg grating

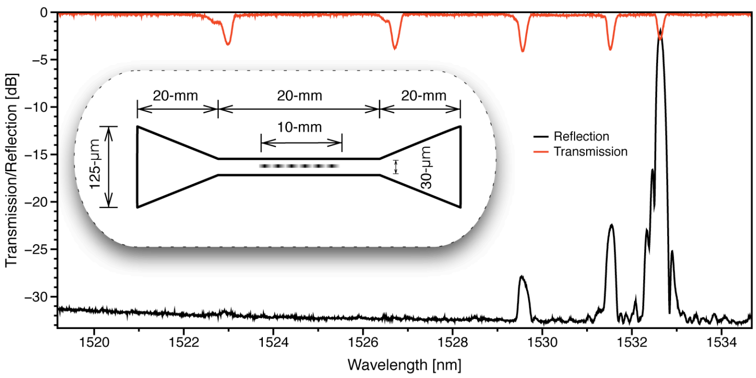

Fig. 4.4 Transmission and reflection spectra of an effectively single reflective mode taper FBG. The insert shows the dimensions of the taper and FBG.

Figure 4.4 shows the transmission and reflection spectra of an effectively single reflective mode MFBG. In the transmission spectrum, there are several notches that are the combined results of the LP_{0N} modes that reflect back to the core mode and LP_{0M} modes that reflect to the cladding modes. Therefore cladding modes are not present in the reflection spectrum.

Figure 4.5 shows the measured reflection spectra of a 20-mm long microfibre with taper lengths of 5, 10, 15, 20 and 25-mm. From the reflection spectra, it is clear that the taper length determines the numbers of peaks that can be re-coupled and propagate in the core of the standard 125-µm diameter fibre. For those with taper lengths of 5, 10, and 15-mm, the peaks that can be detected were 5, 4 and 2, respectively. For taper lengths longer than or equal to 20-mm, the result indicated that effectively one mode was obtained.

The experimental results demonstrated that fibre taper with sufficiently long taper length can effectively re-couple the fundamental mode reflected back to the core and filter out the undesirable higher order modes excited in the MFBG.

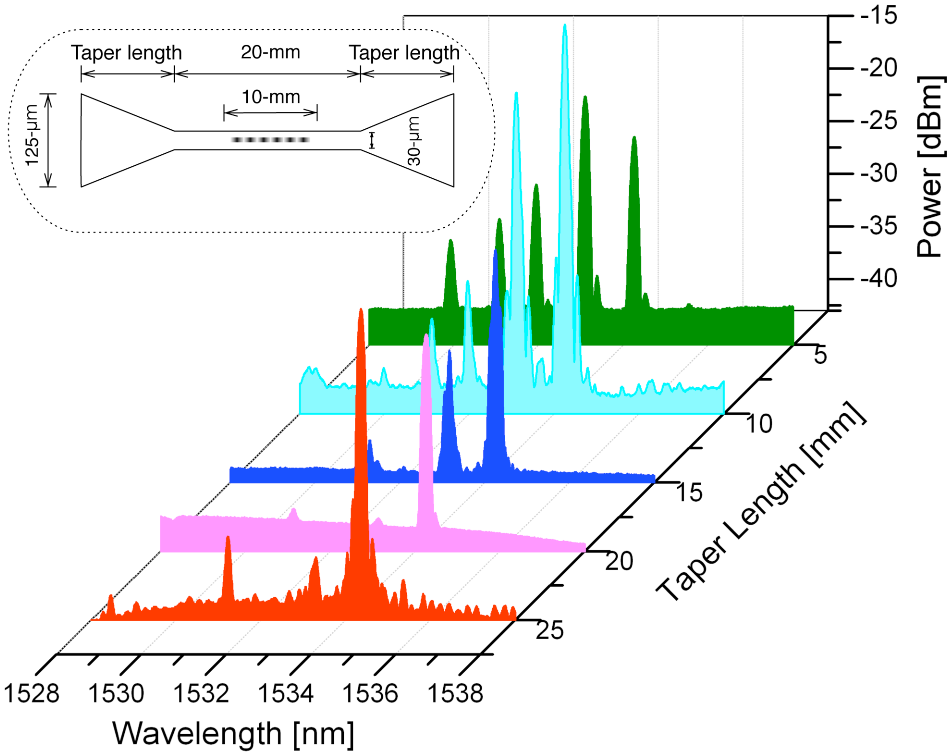

Fig. 4.5 Reflection spectra of MFBGs with different taper lengths. The inset shows the dimensions of the MFBGs.

4.7 Chapter Summary

A novel technique to obtain effective single reflective mode in MFBGs and their experimental results are reported. The study of reflection modes coupling via fibre tapers with different taper lengths were also conducted. The results demonstrated experimentally that the length of a linear taper can be used to achieve an effectively single reflective mode from the FBG written in a multi-mode microfibre. Single reflective mode MFBGs permit ease of multiplexing and demodulation and thus are highly desirable for sensing applications in particular.

Reference

[1] R. P. Kenny, T. A. Birks, and K. P. Oakley, “Control of optical fibre taper shape,” *Electronics Letters*, vol. 27, no. 18, pp. 1654–1656, 1991.

[2] A. C. Boucouvalas and G. Georgiou, “Tapering of single-mode optical fibres,” *IEE Proceedings-J Optoelectronic,*, vol. 133, no. 6, pp. 385–392, Dec. 1986.

[3] J. Love, W. Henry, W. Stewart, R. Black, S. Lacroix, and F. Gonthier, “Tapered Single-Mode Fibers and Devices .1. Adiabaticity Criteria,” *IEE Proceedings-J Optoelectronics*, vol. 138, no. 5, pp. 343–354, 1991.

[4] S. Lacroix, R. Bourbonnais, F. Gonthier, and J. Bures, “Tapered monomode optical fibers: understanding large power transfer,” *Applied Optics*, vol. 25, no. 23, pp. 4421–4425, 1986.

[5] J. D. Love and W. M. Henry, “Quantifying loss minimisation in single-mode fibre tapers,” *Electronics Letters*, vol. 22, no. 17, pp. 912–914, 1986.

[6] L. M. Tong et al., “Subwavelength-diameter silica wires for low-loss optical wave guiding,” *Nature*, vol. 426, no. 6968, pp. 816–819, Dec. 2003.

[7] L. Tong, J. Lou, and E. Mazur, “Single-mode guiding properties of subwavelength-diameter silica and silicon wire waveguides,” *Optics Express*, vol. 12, no. 6, pp. 1025–1035, 2004.

[8] A. J. Fielding, K. Edinger, and C. C. Davis, “Experimental observation of mode evolution in single-mode tapered optical fibers,” *Journal of Lightwave Technology*, vol. 17, no. 9, pp. 1649–1656, Sep. 1999.

[9] X. Fang, C. R. Liao, and D. N. Wang, “Femtosecond laser fabricated fiber Bragg grating in microfiber for refractive index sensing,” *Optics Letters*, vol. 35, no. 7, pp. 1007–1009, Apr. 2010.

[10] Y. Zhang et al., “Refractive index sensing based on higher-order mode reflection of a microfiber Bragg grating,” *Optics Express*, vol. 18, no. 25, pp. 26345–26350, 2010.

[11] Y. Ran et al., “193nm excimer laser inscribed Bragg gratings in microfibers for refractive index sensing,” *Optics Express*, vol. 19, no. 19, pp. 18577–18583, Jan. 2011.

[12] B. Lin, S. C. Tjin, Y. Zhang, B. Dong, and J. Hao, *Microfiber Bragg grating for liquid-level variation sensing*, *Processding of SPIE*, vol. 7753, no. 1, p. 77537K, 2011.

[13] T. A. Birks and Y. W. Li, “The Shape of Fiber Tapers,” *Journal of Lightwave Technology*, vol. 10, no. 4, pp. 432–438, Apr. 1992.

[14] M. Sumetsky, “Optical fiber microcoil resonator,” *Optics Express*, vol. 12, no. 10, pp. 2303–2316, May. 2004.

[15] G. Brambilla, E. Koizumi, X. Feng, and D. Richardson, “Compound-glass optical nanowires,” *Electronics Letters*, vol. 41, no. 7, pp. 400–402, 2005.

[16] C. G. Lu and Y. P. Cui, “Fiber Bragg grating spectra in multimode optical fibers,” *Journal of Lightwave Technology*, vol. 24, no. 1, pp. 598–604, Jan. 2006.

[17] M. L. V. Tse et al., “Observation of symmetrical reflection sidebands in a silica suspended-core fiber Bragg grating,” *Optics Express*, vol. 18, no. 16, pp. 17373–17381, Aug. 2010.

Chapter 5

Characterisitics of Microfibre Bragg gratings

5.1 Introduction

Microfibres are being studied intensively in recent years [1-6]. Microfiber is a kind of fiber tapered in microscopic diameter. It allows propagation in the evanescent field with low transmission loss. Its optical and mechanical characteristics have been studied [7]. The most significant application is used as a microcoil resonator [3], [4], [8-11]. The microresonator has a three-dimensional geometry and complements the well-known Fabry-Perot (one-dimensional geometry, standing wave) and ring (two-dimensional geometry, traveling wave) types of microresonators. In 2010, Microfibre Bragg gratings (MFBGs) combined with microstructured rod is proposed as an optical circuit [12]. Microfibres have attracted a great deal of attention because of its large evanescent fields, low loss through extreme bends, manageable large waveguide dispersion, high nonlinearity, and fully compatible to conventional fibres as well as compact and flexible structure. MFBGs inherent the characteristics of microfiber and add on grating's properties. The characteristics of MFBGs have been intensively studied and exploited for various applications [12-20]. In this chapter, various sensitivities including ambient refractive index, strain on microfibres and temperature of MFBGs will be studied.

5.2 Refractive index sensitivity

Fibre Bragg gratings (FBGs) have been used as various type of all-fibre optics sensing devices because of its advantages including compact size, wavelength encoding, and multiplexing and de-multiplexing capability. However, conventional FBG is unable to sense ambient refractive index (RI) because the optical field is completely guided in the fibre. Combining FBGs and microfibres provides a platform for the development of RI sensors which are easy to multiplex and demodulate. It can be used for evanescent field sensing as the resonant coupling between forward and backward core modes is influenced by the ambient RI. In the past, in order to exploit FBGs as a RI sensor, researchers made use of etched FBG [21-24]. With the aid of hydrofluoric acid, FBG can be etched to the core as small as several microns in diameter. The small core causes part of propagation field to spread outside the core and thus sensitive to the ambient refractive index. The sensitivity achieved can be as high as 1394-nm/riu. It is worth noting that etched fibre results in the degradation of the structure and mechanical property.

In the past two years, MFBGs have been demonstrated to be sensitive to RI. FBGs that were written in microfibre using 800-nm femtosecond laser [25], 248-nm pulsed KrF excimer laser [20], and 193-nm [13] were reported.

In our experiments, all the MFBGs were fabricated by the same method described in Section 5.2. The dimensions of the microfibre unless specified are given as shown in Fig. 5.1.

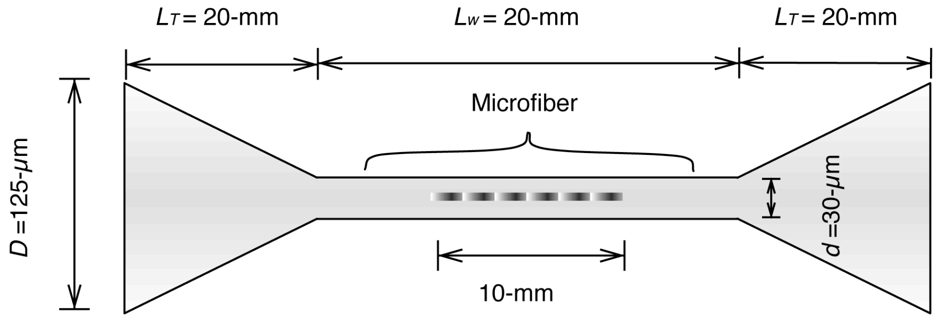

Fig. 5.1 The dimensions of the microfibre Bragg gratings.

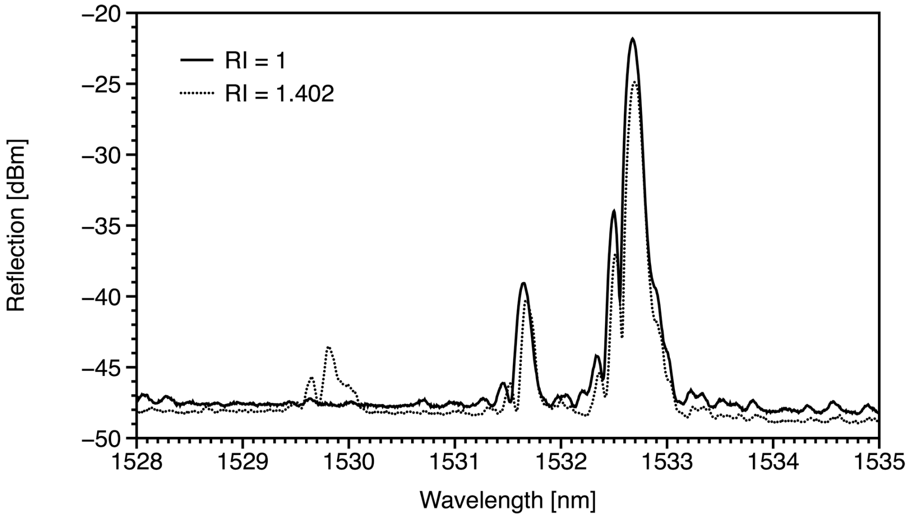

Fig. 5.2 Reflection spectra of MFBG with ambient refractive index of 1 and 1.402.

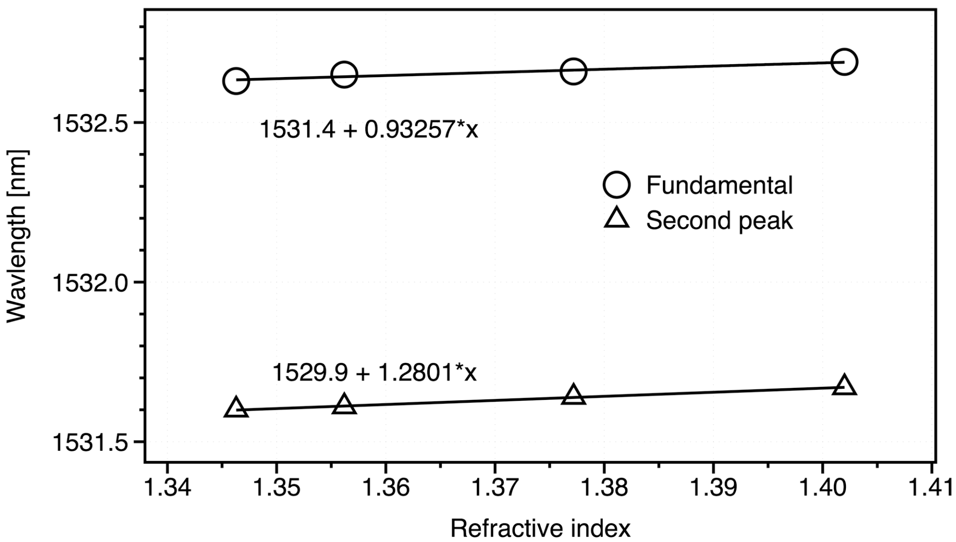

Fig. 5.3 Measurement result of wavelength of the fundamental and second peak as a function of ambient refractive index.

The reflection spectra measured by an FBG interrogator (SM125 from Micron Optics Inc.) with a resolution of 5-pm with ambient refractive indices of 1 and 1.402 were shown in Fig. 5.2. When the MFBG was moved from air (RI≈1) into the sucrose solution, the grating reflection peaks experienced an abrupt shift to longer wavelength and the strength of the resonance peaks decreased. This is due to the higher RI (~1.402) of the sucrose solution compared to air increases the effective refractive indices of the propagation modes of the microfibre because the effective refractive indices are partially determined by the ambient RI. In other word, some of the energy of the guided mode propagate via the evanescent field and therefore, the ambient RI affects the effective refractive indices of the modes. The resonant peaks of the MFBGs depends of the effective refractive indices of the corresponding modes and are given by:

$$\lambda_B = 2n_{eff}\Lambda, \tag{5.1}$$

where Λ is the pitch of the grating, and n_{eff} is the effective refractive index of the mode.

The wavelengths of the MFBG as function the ambient RI in the range from 1.34 to 1.4 was also measured and shown in Fig. 5.3. The experiment setup was that an MFBG was immersed into the sucrose solutions with different RI values. The solution was calibrated by a refractometer (Reichert Technologies).

Higher RI sensitivity was observed in the Bragg wavelength of higher order mode. They have larger energy fractions distributed to outside of the microfibre and therefore stronger interaction with the ambient RI.

5.3 Strain and force characteristics

The study of strain sensitivity of FBGs written in a tapered fibre was reported in [26], and sensor applications with FBGs in the taper transition region were discussed [27-29]. For strain measurement application, the FBGs are embedded into composites or bonded to the surface of the components by means of adhesives. In typical strain applications, the structures whose strain is to be measured have a larger stiffness (high Young's modulus, high cross-sectional area) compared to the bonding layer and the fibre that contains the Bragg grating. Therefore, fibre gratings with a diameter of 125-μm do not have a strong influence on the accuracy of the strain measurement. However, if Bragg gratings are used to measure strain on substrates that are very thin or made of materials with small Young's modulus (e.g. polymers), the stiffness of the fibre may become significant [30]. If FBGs based sensors are embedded into composite materials (e.g. thin thermoplastic laminates), the fibre can also induce perturbations and defects in the structure. Therefore, optical fibre with diameter significantly smaller than 125-μm is desirable. In 2004, Kojima et al [31] introduced a real-time health monitoring system based on FBGs inscribed in an optical fibre with a diameter of 40-μm (developed by Hitachi Cable Ltd). In some applications, a small diameter optical fibre is needed due to its higher force or tension sensitivity. However, the compatibility to the standard 125-μm fibre is also important for providing ease of handling and installation. These are the most important points that enable low-cost installation. To cope with this type of applications, MFBGs can be a good candidate that provides high-tension sensitivity and compatibility to standard single mode optical fibre.

5.3.1 Strain test

Figure 5.4 shows the reflection spectra of a MFBG with different applied strains. The grating spectra were measured by an MOI interrogator (Model SM-125) with resolution of 5-pm. The peak wavelength and 3-dB bandwidth were 1532.57-nm and 0.1-nm, respectively. The overall side mode suppression was ~14-dB. When ~1% or ~10000-με applied, the reflection is decreased by 1-dB.

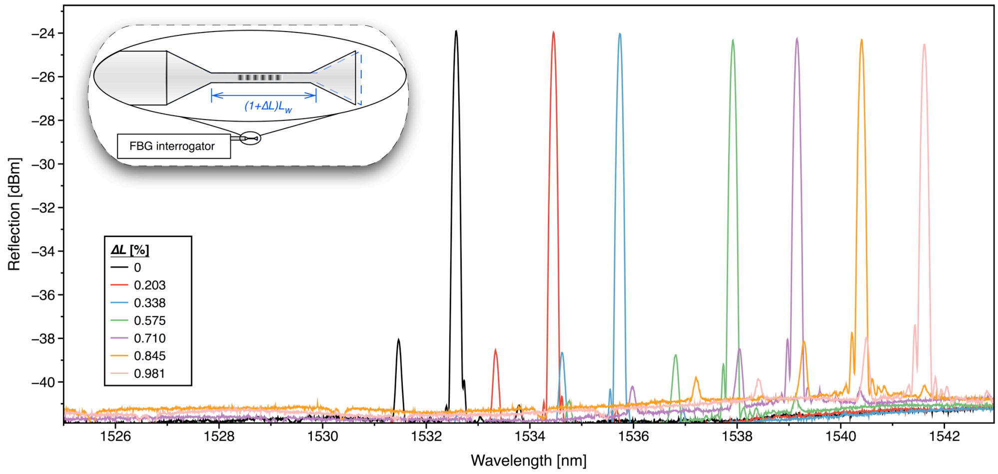

Fig. 5.4. Refection spectra of a MFBG with different strains were applied. The inset shows the schematic diagram.

5.3.2 Taper elongation

In this section, the elongation of the microfibre taper is investigated. When tension is applied to the microfibre, strains along the taper region are different because of diameter difference. The cross section area of the microfibre region has the smallest diameter. When strain is applied, the rate of its elongation along the longitudinal axis is dependent on its cross section.

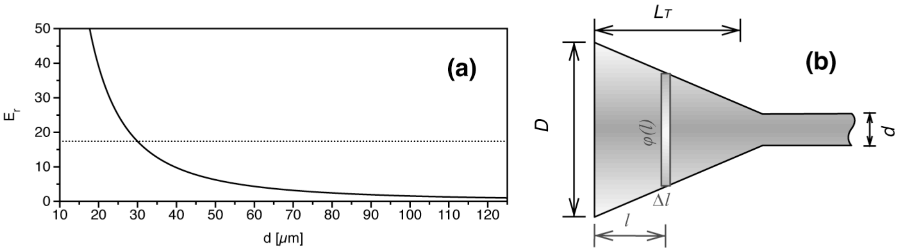

Fig. 5.5 (a) Elongation ratio with different waist diameters. (b) Illustration of a taper with symbols.

In the taper, the elongation ratio of a segment is defined as

$$E(\varphi) = \frac{D^2}{\varphi^2}. \tag{5.2}$$

where D is the initial diameter and φ is the diameter of a segment. The elongation ratio is proportional to its diameter. For microfibre with the diameter of 30-μm, $E(d)$ is greater than 17. It implies that the microfibre requires 17 times smaller force to tune the FBG than the conventional counterpart.

It was difficult to apply strain to just the microfibre section and strain was applied via the non-elongated fibres at both ends of the microfibre. When tension was applied, both the taper region and the microfibre were also elongated. Strain sensitivity for an FBG written on taper was reported in literature [26]. In our application, the strain at the waist region is of our interest. Assuming the taper is geometrically symmetrical in both sides, we have

$$\Delta L_{Total} = 2\Delta L_T + \Delta L_w. \tag{5.3}$$

Since the elongations of the taper and waist are proportional to its length and the effective elongation ratio of the parts, we have

$$\Delta L_{Total} = \left(\frac{2L_T E_{Taper}}{2L_T E_{Taper} + L_w E(d)} + \frac{L_w E(d)}{2L_T E_{Taper} + L_w E(d)} \right) \Delta L_{Total}. \tag{5.4}$$

By comparing Eq. (5.3) and (5.4), we then obtain,

$$\Delta L_w = \frac{L_w E(d)}{2L_T E_{Taper} + L_w E(d)} \Delta L_{Total} \tag{5.5}$$

The effective elongation ratio of the taper, E_{Taper}, can be evaluated by considering the integration of the taper, i.e.

$$E(\varphi)\Delta l = \frac{D^2}{(\frac{d-D}{L_T} l + D)^2} \Delta l \tag{5.6}$$

$$L_T E_{Taper} = \int_0^{L_T} E(\varphi) dl = \frac{L_T D}{d} \tag{5.7}$$

By substituting Eq. (5.7) into Eq. (5.5), we obtain

$$\Delta L_w = \frac{DL_w}{2dL_T + DL_w} \Delta L_{Total}. \tag{5.8}$$

By substituting D = 125-µm, L_T = L_W = 20-mm and d =30-µm into Eq. (5.8), the elongation of the microfibre, ΔL, then becomes

$$\Delta L = \frac{\Delta L_w}{L_w} = \frac{0.68 \Delta L_{Total}}{L_w}. \tag{5.9}$$

With Eq. (5.9), the total displacement measured in the experiment can be converted to strain.

5.3.3 Strain-optics coefficients

The shift in Bragg wavelength, $\Delta\lambda$, depends on the physical elongation of the grating and the change of n_{eff} due to photoelastic effect. Therefore, $\Delta\lambda$ can be expressed as [31]:

$$\frac{\Delta\lambda}{\lambda_B} = (1 - P_e)\varepsilon_{ax}, \tag{5.10}$$

where ε_{ax} is the axial tensile strain, which determines the elongation of the grating along the longitudinal axis of the optical fibre. The strain-optics coefficient, P_e, is affected by two factors [32]. The first factor is related to the material content and the second is waveguide properties.

For a standard step index single mode fibre, P_e is only determined by the material parameters because the propagation angle is closed to zero and is then governed by

$$P_e = -\frac{n_{core}^2}{2}[p_{12} - v(p_{11} + p_{12})], \tag{5.11}$$

where v is the Poisson ratio and $P_{i,j}$ is the Pockel's (piezo) coefficients of the stress-optics tensor. By substituting $v = 0.16$, $p_{11} = 0.113$ and $p_{12} = 0.252$, reported by [33], we can obtain $P_e \cong 0.22$ for conventional single mode optical fibre. The effective stress-optics coefficient is determined by the material stress-optics which is approximately equal to P_e and the waveguide factor. For an air-clad guiding microfibre, the waveguide factor has to be considered. Taking the waveguide property into account, P_e can then be evaluated by the expression [32]:

$$P_e = (1 - \sec\theta)\left(v + \frac{1+v}{\sec\theta}\right) - \frac{n_{core}^2 \sec\theta}{2}[(1-v)p_{12} - vp_{11}], \tag{5.12}$$

where the propagation angle of the guided fundamental mode, θ, is in the range of

$$0 \le \theta \le \cos^{-1}\left(\frac{n_{air}}{n_{core}}\right). \tag{5.13}$$

The guided modes of the microfibre are bounded by the air and microfibre. Since the difference between n_{air} and n_{core} is very large, Δn~0.444, resulting the value of θ as large as ~46˚.

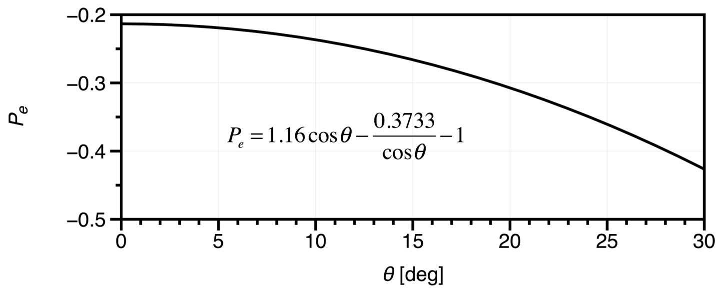

Fig. 5.6 The calculated result of P_e with different propagation angles.

Figure 5.6 shows the simulation result of the P_e for different propagation angles varying from 0 to 30˚. Using Eq. (5.12), we obtain P_e = -0.4 from our experimental result. The air-clad guided microfibre therefore has a propagation angle of 28˚. It implies that the big refractive indices differences between air and microfibre induces a large angle of propagation and thus increases the effective strain-optics coefficient by -0.18, comparing to the standard telecommunication fibre.

5.3.4 Applied force

The applied force to tune the microfibre Bragg grating with a diameter, *d*, is obtained by

$$F = \sigma A = \tfrac{\pi}{4} E \varepsilon_{ax} d^2, \tag{5.14}$$

where the modulus of elasticity $E \cong 72.5$-GPa. To reach 1% of strain for a microfibre FBG with diameter of 30-µm, the required force is only ~0.5-N according to Eq. (5.14). For a standard FBG, the required force is ~8.9-N.

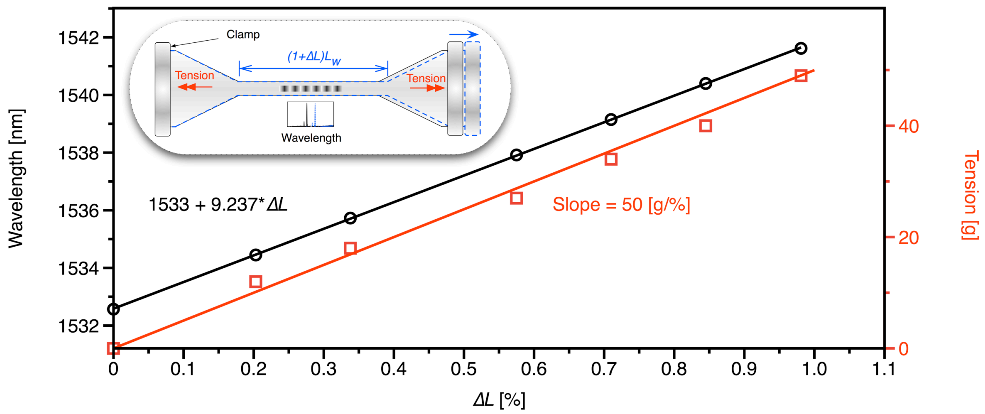

Fig. 5.7. Experiment result of the tunable filter. The black line shows the linear fit of the wavelength against the ΔL and the red dots shows the corresponding measured tension and the linear fit. The insert illustrates the overall schematic of the tunable filter.

Figure 5.7 shows the experimental result of wavelength shift and applied tension against strain. The maximum wavelength shift of MFBG tunable filter was 9.05-nm with 0.981% and 0.49-N of applied strain and applied tension, respectively. The sensitivity of the required force is 0.5-N per strain in percentage. The results are in good agreement with each other. There was some small measurement error of the load cell used for measuring the applied tension.

5.3.5 Maximum strain of microfibres with and without FBG inscription, hydrogen-loading and annealing

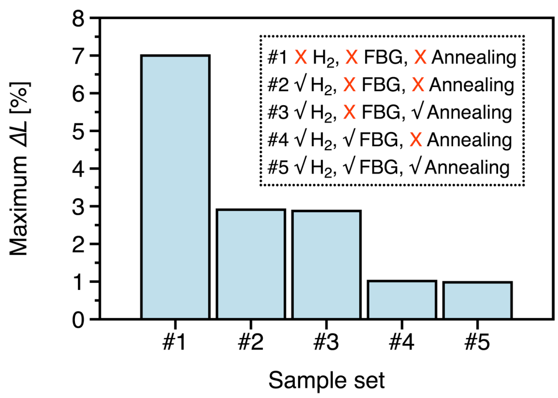

Fig. 5.8 Experimental results of maximum strain of microfibres fabricated under different conditions.

Carmen et al [35] reported that the typical maximum tensile strain of a conventional 125-µm diameter optical fibre before breaking is ~8% and after grating inscription, the maximum strain reduces to ~1%. In order to compare the tensile breaking strength of the microfibre before and after grating inscription, we conducted pulling test for five sets of samples sets that are the combination of three statuses. These statuses are of common processes of writing grating in a Ge-doped optical fibre. They are hydrogen-loading, FBG inscription and annealing, labeled as H_2, FBG and annealing in the Fig. 5.8, respectively.

The conditions of the hydrogen loading and FBG inscription were described in section 2.1. Annealing is a process to stabilize the grating characteristics, i.e. the Bragg wavelength and reflectivity. In the process, the large diameter microfibre FBGs were put in an oven with constant temperature of 100˚C for over 24 hours.

Figure 5.8 shows the experimental result. The number of samples used in each set is five. All the samples had the same dimensions and were fabricated on the same day. The sample set #1 is the pristine microfibre and achieved 7 % of maximum strain in the test. The maximum strain of #2 and #3 reduced to ~3%, and #4 and #5 further decrease to only ~1%. After the exposure to UV laser light, the grating strength was even weaker. The annealing process does not affect the maximum strain. The results are similar to the standard FBG. We believe that the microfibre has more or less the same strain as the standard optical fibre, even after grating inscription. The result also revealed that the microfibre after hydrogen loading weakened the strength of the microfiber. The weakness might be due to the handling during the hydrogen loading process or the hydrogen weakens the strength of the fibre.

5.3.6 MFBGs written in photosensitive fibres

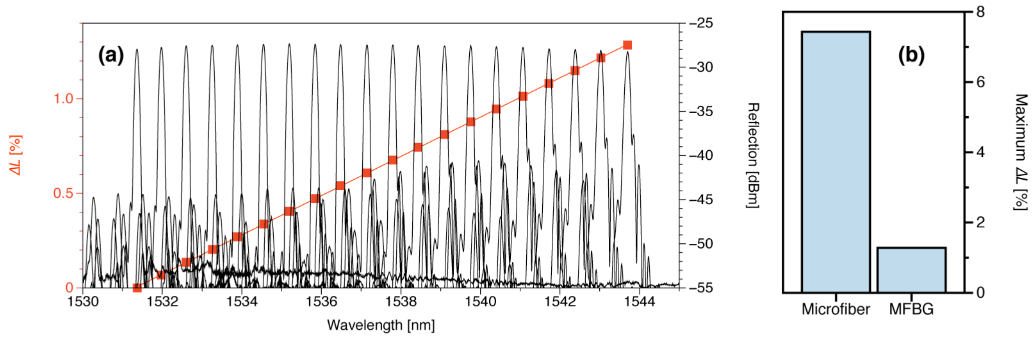

Fig. 5.9 (a) The measured result of the reflection spectrum with different ΔL (black color) and measured ΔL against different wavelengths (red color). (b) The maximum ΔL of pristine microfibre and MFBG.

In this section, a photosensitive fibre (manufactured by Fibercore) was used for writing gratings. Using this fibre, the hydrogen loading is not required. Microfibres made from this type of fibre have significantly higher photosensitivity. It would be interesting to see if the MFBGs will have higher tensile breaking point without the hydrogen loading process. Figure 5.9 (a) shows the test result. The black lines show the reflection spectra with different strains. The red line shows the corresponding strain in the microfibre. The sensitivity of the wavelength shift is 9.6-nm/%. The maximum wavelength shift is 12.33-nm with 1.28% strain. Figure 5.9 (b) shows the maximum strain of the pristine microfibre and MFBG using the FiberCore's photosensitive fibre. The microfibre without FBG inscription was tested and it has similar strength with the microfibre made from the bend-insensitive fibre. The sample sizes of microfiber and MFBG are six. The result also shows that the MFBG without hydrogen loading has a small improvement in strength.

5.4 Temperature sensitivity

Fibre Bragg gratings are commonly employed as temperature sensors [35-39]. Various techniques have been investigated to improve FBG-based temperature sensors [36], [40-48]. In 1992, Kersey demonstrated that FBGs could be used as differential-temperature sensor with a resolution better than 0.05˚C based on interferrometric technique for wavelength interrogation [48]. In the late 1990s, techniques for the strain discrimination of temperature sensors were introduced [44-45], [47]. Different materials were used to enhance the FBG based temperature sensors. Thermal behavior of a metal embedded FBG was studied [42]. Techniques for high temperature sensing [40-41], [49] and extreme low temperature [46] were also reported. Recently, temperature sensing based on tilted fibre Bragg grating written in a 6.5-μm diameter microfibre was demonstrated [18].

In this section, we will investigate the temperature sensitivity of the microfibre Bragg gratings.

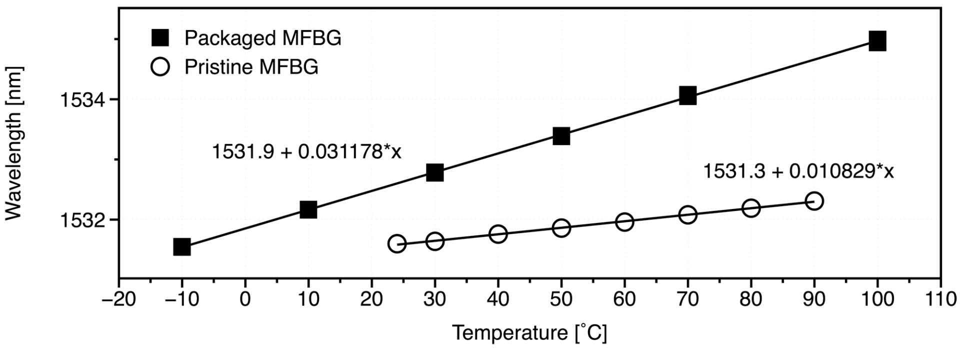

Fig. 5.10 Reflected wavelength versus temperature of the MFBG before and after packaging.

Figure 5.10 shows the reflected wavelength of the MFBGs with and without packaging as a function of the temperature. The temperature test of a bare MFBG was tested. The test was done by putting the grating inside a water tank. The wavelength of the grating was measured with different temperature of the water. The temperature sensitivity of the MFBG was 10-pm/℃, which is almost identical to that of conventional FBG. An MFBG embedded by an elastomer material was also tested. The MFBG was put into a programmable oven for testing the temperature ranged from -10 to 100℃. The wavelength was measured with the temperature for each step of 30℃. It took over half an hour for each temperature being stabilized. When packaged, the temperature response was three times more sensitive than that without the package. This is due to the fact that the embedded package is expanded and then apply strain on the microfibre.

5.5 Chapter summary

In this chapter, the ambient refractive index, strain and temperature sensitivity of a 30-μm diameter microfibre Bragg grating have been investigated. The sensitivity to the ambient refractive index in the different observed modes was studied. Strain and sensitivity to tension have been investigated. The tests of break failures of the MFBGs in conditions of pristine, hydrogen loaded, and exposure to UV have been conducted. Physical elongation of microfibres in the different regions has also analysed. Temperature sensitivities of the reflected wavelengths of MFBGs with and without packaging have been characterised. We believe that MFBG which inherits the combinations of advantages of the microfibre and Bragg gratings would find some optical sensing applications which require high sensitivity to force or tension, or extremely compact size, evanescent field propagation, or compatible to standard single mode fibre.

Reference

[1] L. Tong, “Microfiber and Nanofiber Optics: Principles and Applications,” *Asia Communications and Photonics Conference and Exhibition (2009), paper ThAA2*, Nov. 2009.

[2] Y. Jung and G. Brambilla, “Optical microfiber coupler for broadband single-mode operation,” *Optics Express*, 2009.

[3] G. Brambilla et al., “Optical fiber nanowires and microwires: fabrication and applications,” *Advances in Optics and Photonics*, vol. 1, no. 1, p. 107, 2009.

[4] F. Xu, P. Horak, and G. Brambilla, “Optical microfiber coil resonator refractometric sensor,” *Optics Express*, vol. 15, no. 12, pp. 7888–7893, Jun. 2007.

[5] G. Zhai and L. Tong, “Roughness-induced radiation losses in optical micro or nanofibers,” *Optics Express*, vol. 15, no. 21, pp. 13805–13816, 2007.

[6] J. W. Mu and W. P. Huang, “Complex coupled-mode theory for tapered optical waveguides,” *Optics Letters*, vol. 36, no. 6, pp. 1026–1028, Mar. 2011.

[7] G. Brambilla, F. Xu, and X. Feng, “Fabrication of optical fibre nanowires and their optical and mechanical characterisation,” *Electronics Letters*, vol. 42, no. 9, pp. 517–519, 2006.

[8] Y. Chen, F. Xu, and Y.-Q. Lu, “Teflon-coated microfiber resonator with weak temperature dependence,” *Optics Express*, vol. 19, no. 23, p. 22923, 2011.

[9] F. Xu and G. Brambilla, “Demonstration of a refractometric sensor based on optical microfiber coil resonator,” *Applied Physics Letters*, vol. 92, no. 10, pp. –, Mar. 2008.

[10] F. Xu, P. Horak, and G. Brambilla, "Conical and biconical ultra-high-Q optical-fiber nanowire microcoil resonator," *Applied Optics*, vol. 46, no. 4, pp. 570–573, Feb. 2007.

[11] M. Sumetsky, "Optical fiber microcoil resonator," *Optics Express*, vol. 12, no. 10, pp. 2303–2316, May. 2004.

[12] F. Xu, G. Brambilla, J. Feng, and Y.-Q. Lu, "A Microfiber Bragg Grating Based on a Microstructured Rod: A Proposal," *IEEE Photonics Technology Letters*, vol. 22, no. 4, pp. 218–220, 2010.

[13] Y. Ran et al., "193nm excimer laser inscribed Bragg gratings in microfibers for refractive index sensing," *Optics Express*, vol. 19, no. 19, pp. 18577–18583, Jan. 2011.

[14] M. Ding, M. N. Zervas, and G. Brambilla, "A compact broadband microfiber Bragg grating," *Opt. Express*, vol. 19, no. 16, pp. 15621–15626, 2011.

[15] T. Wieduwilt and et al, "High force measurement sensitivity with fiber Bragg gratings fabricated in uniform-waist fiber tapers," *Measurement Science and Technology*, vol. 22, no. 7, p. 075201, 2011.

[16] X. Yu, X. Li, Y. Zhang, L. Zhou, W. Jiang, and J. Chen, "Fabrication of Microfiber-Based Bragg Gratings with Ultraviolet-Light Exposure," *Optical Fiber Communication Conference*, p. OTuC2, 2011.

[17] Y. Liu, C. Meng, A. P. Zhang, Y. Xiao, H. Yu, and L. Tong, "Compact microfiber Bragg gratings with high-index contrast," *Optics Letters*, vol. 36, no. 16, pp. 3115–3117, 2011.

[18] J.-L. Kou, S.-J. Qiu, F. Xu, and Y.-Q. Lu, “Demonstration of a compact temperature sensor based on first-order Bragg grating in a tapered fiber probe,” *Optics Express*, vol. 19, no. 19, pp. 18452–18457, 2011.

[19] B. Lin, S. C. Tjin, Y. Zhang, B. Dong, and J. Hao, *Microfiber Bragg grating for liquid-level variation sensing*, *Proc. of SPIE*, vol. 7753, no. 1, 2011, p. 77537K.

[20] Y. Zhang et al., “Refractive index sensing based on higher-order mode reflection of a microfiber Bragg grating,” *Optics Express*, vol. 18, no. 25, pp. 26345–26350, 2010.

[21] A. N. Chryssis, S. S. Saini, S. M. Lee, Hyunmin Yi, W. E. Bentley, and M. Dagenais, “Detecting hybridization of DNA by highly sensitive evanescent field etched core fiber Bragg grating sensors,” *IEEE Journal of Selected Topics in Quantum Electronics*, vol. 11, no. 4, pp. 864–872, 2005.

[22] X. Sang, C. Yu, T. Mayteevarunyoo, and K. Wang, “Temperature-insensitive chemical sensor based on a fiber Bragg grating,” *Sensors and Actuators B: Chemical*, vol. 120, no. 2, pp. 754–757, 2007.

[23] A. N. Chryssis, S. M. Lee, S. B. Lee, S. S. Saini, and M. Dagenais, “High sensitivity evanescent field fiber Bragg grating sensor,” *IEEE Photonics Technology Letters*, vol. 17, no. 6, pp. 1253–1255, 2005.

[24] A. Iadicicco, S. Campopiano, A. Cutolo, M. Giordano, and A. Cusano, “Refractive index sensor based on micro structured fiber Bragg grating,” *IEEE Photonics Technology Letters*, vol. 17, no. 6, pp. 1250–1252, 2005.

[25] X. Fang, C. R. Liao, and D. N. Wang, “Femtosecond laser fabricated fiber Bragg grating in microfiber for refractive index sensing,” *Optics Letters*, vol. 35, no. 7, pp. 1007–1009, Apr. 2010.

[26] O. Frazao, S. F. O. Silva, A. Guerreiro, J. L. Santos, L. A. Ferreira, and F. M. Araujo, “Strain sensitivity control of fiber Bragg grating structures with fused tapers,” *Applied Optics*, vol. 46, no. 36, pp. 8578–8582, Dec. 2007.

[27] D. Monzo´n-Herna´ndez, J. Mora, P. Pe´rez-Milla´ n, A. Dı´ez, J. L. Cruz, and M. V. Andre´s, “Temperature Sensor Based on the Power Reflected by a Bragg Grating in a Tapered Fiber,” *Applied Optics*, vol. 43, no. 12, p. 2393, 2004.

[28] A. González-Segura, J. L. Cruz, M. V. AndrÈs, P. Barrios, and A. Rodríguez, “Fast response vibration sensor based on Bragg gratings written in tapered core fibres,” *Measurement Science and Technology*, vol. 18, no. 10, pp. 3139–3143, Sep. 2007.

[29] O. Frazao, M. Melo, P. V. S. Marques, and J. L. Santos, “Chirped Bragg grating fabricated in fused fibre taper for strain-temperature discrimination,” *Measurement Science and Technology*, vol. 16, no. 4, pp. 984–988, Apr. 2005.

[30] W. Li, C. Cheng, and Y. Lo, “Investigation of strain transmission of surface-bonded FBGs used as strain sensors,” *Sensors and Actuators A: Physical*, vol. 149, no. 2, pp. 201–207, Feb. 2009.

[31] S. Kojima, S. Komatsuzaki, and Y. Kurosawa, “The embedding type strain sensors using small-diameter fiber Bragg grating to composite laminate structures,” *Hitachi Cable review, no. 23*, 2004.

[32] S. M. Melle, K. Liu, and R. M. Measures, “Practical fiber-optic Bragg grating strain gauge system,” *Applied Optics*, vol. 32, no. 19, pp. 3601–3609, 1993.

[33] A. M. Vengsarkar, D. D. Thomas, B. D. Zimmermann, and R. O. Claus, “Modal dependence of the photoelastic coefficient in multimode, step-index optical fiber time

domain systems," *IEEE Photonics Technology Letters*, vol. 2, no. 11, pp. 812–814, 1990.

[34] A. Bertholds and R. Dandliker, "Determination of the individual strain-optic coefficients in single-mode optical fibres," *Journal of Lightwave Technology*, vol. 6, no. 1, pp. 17–20, 1988.

[35] G. P. Carman and G. P. Sendeckyj, "Review of the mechanics of embedded optical sensors," *Journal of Composites Technology and Research*, vol. 17, no. 3, pp. 183–193, 1995.

[36] K. O. Hill and G. Meltz, "Fiber Bragg grating technology fundamentals and overview," *Journal of Lightwave Technology*, vol. 15, no. 8, pp. 1263–1276, Aug. 1997.

[37] Y.-J. Rao, "In-fibre Bragg grating sensors," *Measurement Science and Technology*, vol. 8, no. 4, pp. 355–375, Jan. 1999.

[38] A. D. Kersey et al., "Fiber grating sensors," *Journal of Lightwave Technology*, vol. 15, no. 8, pp. 1442–1463, 1997.

[39] R. Kashyap, *Fiber Bragg Gratings*. Academic Press, 2009.

[40] A. Othonos and K. Kalli, *Fiber Bragg gratings*. Artech House Publishers, 1999.

[41] L. V. Nguyen, D. Hwang, S. Moon, D. S. Moon, and Y. Chung, "High temperature fiber sensor with high sensitivity based on core diameter mismatch," *Optics Express*, vol. 16, no. 15, pp. 11369–11375, 2008.

[42] B. W. Zhang and M. Kahrizi, "High-temperature resistance fiber Bragg grating temperature sensor fabrication," *IEEE Sensors Journal*, vol. 7, no. 3, pp. 586–591, Mar-Apr. 2007.

[43] X. Li and F. Prinz, “Thermal behavior of a metal embedded fiber Bragg grating sensor,” *Smart materials and structures*, 2001.

[44] J. Jung, N. Park, and B. Lee, “Simultaneous measurement of strain and temperature by use of a single fiber Bragg grating written in an erbium:ytterbium-doped fiber,” *Applied Optics*, vol. 39, no. 7, pp. 1118–1120, 2000.

[45] B.-O. Guan, H.-Y. Tam, S.-L. Ho, W.-H. Chung, and X.-Y. Dong, “Simultaneous strain and temperature measurement using a single fibre Bragg grating,” *Electronics Letters*, vol. 36, no. 12, pp. 1018–1019, 2000.

[46] Wei-Chong Du, Xiao-Ming Tao, and Hwa-Yaw Tam, “Fiber Bragg grating cavity sensor for simultaneous measurement of strain and temperature,” *IEEE Photonics Technology Letters*, vol. 11, no. 1, pp. 105–107, 1999.

[47] S. Gupta, T. Mizunami, T. Yamao, and T. Shimomura, “Fiber Bragg grating cryogenic temperature sensors,” *Applied Optics*, vol. 35, no. 25, pp. 5202–5205, 1996.

[48] S. W. James, M. L. Dockney, and R. P. Tatam, “Simultaneous independent temperature and strain measurement using in-fibre Bragg grating sensors,” *Electronics Letters*, vol. 32, no. 12, pp. 1133–1134, 1996.

[49] A. D. Kersey and T. A. Berkoff, “Fiber-optic Bragg-grating differential-temperature sensor,” *IEEE Photonics Technology Letters*, vol. 4, no. 10, pp. 1183–1185, 1992.

[50] E. Lindner et al., “Arrays of Regenerated Fiber Bragg Gratings in Non-Hydrogen-Loaded Photosensitive Fibers for High-Temperature Sensor Networks,” *Sensors*, vol. 9, no. 10, pp. 8377–8381, Oct. 2009.

Chapter 6

Microfibre Bragg grating based force sensor

6.1 Introduction

Microfibre Bragg gratings feature compact size, compatible to standard optical fibre and extremely high sensitivity to force or tension. It is a promising candidate for force sensing applications that require high compactness and sensitivity. FBG-based force sensors using standard telecoomunication fibres have limited sensitivity due to their larger diameter of 125-μm and Young's modulus of 70.3-Gpa. FBG inscripted in polymer optical fibres (POFs) which have more than 70 times smaller Young's modulus was proposed [1] but writing FBG in POFs is difficult [2], [3]. Mechanical transducers were employed to convert force to strain [4-11] to enhance the sensitivity of FBGs for force measurements. T. Guo et al [11] and L. M. Hu [7] employed mechanical transducers that induced chirp to the FBG when subjected to load/force. The induced bandwidth broadening and reflected optical power from the FBGs are temperature-insensitive and thus realizing temperature-insensitive force sensors using one FBG. L. F. Xue [8] attached two FBGs on the outer circumference of a tube to measure force based on the deformation of the tube when it was subjected to load. L. Y. Shao [9] applied Fourier analysis to the transmission spectrum of the cladding modes of a tilted FBG that was sandwiched between two elastomer materials. The contact surface area between the fiber and elastomer varied with lateral force and induced changes in the cladding modes which decreased with the applied force. Recently, Reck et al [10] demonstrated a microelectromechanical (MEMS) Bragg grating force sensor and achieved a very high sensitivity of -14 nm/N. The spectral width of the MEMS-FBG was rather broad (2.3 nm), making precise peak wavelength measurement difficult and that could be the reason for the large measurement uncertainly of ±10-mN.

There are many applications that require miniaturized force sensors with high sensitivity to measure contact force, especially in medical applications. One such application is in cardiac catheterization where it is important for physicians to know the contact force between the catheters and blood vessel walls in order to avoid damaging the delicate blood vessel networks of the patient during an interventional procedure.

Panagiotis et al [12] reviewed different kinds of fiber-optic force and pressure sensors for catheterization procedures in terms of their size, working range and measurement resolution. Fiber-optics sensors are promising candidates because of their compactness, easily manufacturable, potentially low cost, biocompatible and ability to tolerate sterilization procedures. Panagiotis et al [12] also explained that among all the various types of fiber-optics force sensors, sensors based on FBGs are, up to now, the best technology that features all the essential criteria such as miniaturized size (including packages), good sensitivity to minimal touch, high resolution, linear behavior, low hysteresis and most importantly magnetic resonance imaging (MRI) compatibility.

A force sensor based on FBGs for catheterization procedures was reported in 2008 [13]. The force sensor (TactiCath^{TM}), designed by Endosense SA in collaboration with Stanford University, was integrated inside a 7-Fr (equivalent to 2.2-mm) diameter cardiac catheter for measuring contact force. The operation principle of the sensor relies on the deformation of three optical fibers which were inscribed with FBGs. The fibers were held in place by a deformable elastic polymer material. When a force is applied to the sensor, the flexible inner body deformed and resulted in stretching or compressing the FBGs. By monitoring the wavelength shifts of the three FBGs arranged at 120° to each other in a circle, the magnitude and position of the applied force can be determined.

Wieduwilt et al [14] proposed to use an FBG written in a small diameter optical fiber to enhance its force sensitivity and demonstrate experimentally, by attaching different weights to the fiber, that the sensitivity increases when the fiber cross-sectional area gets smaller.

In this chapter, we propose and experimentally demonstrate a force sensor based on a 30-μm diameter microfiber Bragg grating (MFBG) embedded in a package suitable for use in minimally invasive surgery (MIS) devices. The use of the 30-μm diameter microfiber was found to be sufficient, in terms of sensitivity to contact force and fiber rigidity to prevent buckling over the measurement range, for such applications and at the same time it not too small to handle. There are two main challenges for employing the MFBG as a contact force sensor. The first is the multi-mode characteristics as the light guiding become air-clad. The second is the design of the deformation body to keep the MFBG in place when no force is applied and ensure that the MFBG is compressed axially when a small force is applied.

The most notable difference in the spectra between the FBG and MFBG is the multiple reflection peaks excited by the MFBG [15], [16]. Single reflection peak in normal FBG is desirable because it is easier for demodulation and demultiplexing. In this chapter, we demonstrated that the reflection from MFBG can be made effectively single mode by re-coupling the higher order modes to the cladding with a 20-mm long linear taper profile. The guiding mechanism of the microfiber to ensure the force sensor has a linear force-to-wavelength conversion characteristic will also be reported. The proposed miniaturized force sensor is potentially useful to provide real time contact force sensor in catheters.

6.2 Principle of the MFBG-based force sensor

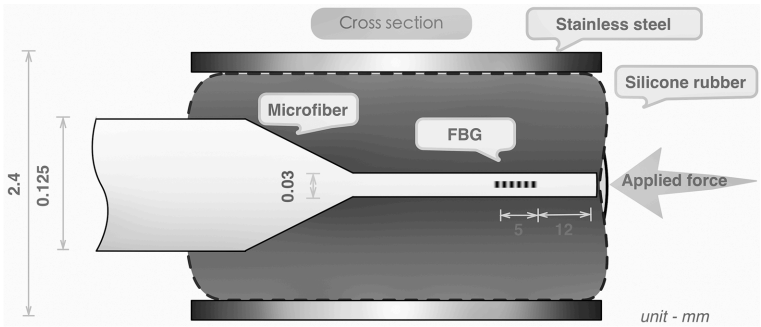

Fig. 6.1 Schematic diagram of the force sensor based on a microfiber Bragg grating.

Figure 6.1 shows the schematic diagram of the MFBG-based sensor to illustrate how it functions as a contact force sensor. A 30-μm diameter microfiber was embedded in the centre of a silicone rubber, an elastomer material, which was then placed inside a non-magnetized stainless steel tube. An FBG inscribed in the microfiber will be compressed when it comes in contact with an object such as blood vessels, resulting in the FBG's reflection wavelength shift. The microfiber was cleaved at a distance of 12-mm from the FBG as shown in Fig. 6.1. The other end of the microfiber is a standard single-mode fiber with a diameter of 125-μm and is connected to an FBG interrogator (Micron Optic Inc., model SM130). When a small force is applied to the sensor, the silicone rubber together with the grating is slightly compressed in the axial direction because the stainless tube restricts the side-way movement of the silicone rubber. Consequently, the compressive strain induced to the FBG is linearly proportional to the applied force. After calibration, the contact force can be determined by monitoring the reflected wavelength of the MFBG. The Bragg wavelength λ_B is given by the expression:

$$\lambda_B = 2n_{eff}\Lambda, \tag{6.1}$$

where n_{eff} and Λ are the effective refractive index and the pitch of the MFBG, respectively. When the grating is under compressive strain, these two parameters are changed. The change of Λ is due to physically shortening in the length of the grating and the change in microfiber's refractive index is due to photoelastic effect. The relationship of the wavelength shift and axial strain can be expressed as:

$$\frac{\Delta\lambda}{\lambda_B} = (1 - P_e)\varepsilon_{ax}, \tag{6.2}$$

where P_e is the constant of optic-strain coefficient and ε_{ax} is the axial strain. The proposed sensor has a linear response to compressive strain induced to the grating within the operation range. Ignoring the temperature effect, the shift of reflected wavelength can be simplified to:

$$\Delta\lambda = -\alpha F, \tag{6.3}$$

where F is the applied force in the linear region and α is the sensitivity of the sensor to axial force. The sensitivity was measured to be ~0.73-nmN^{-1} for our sensor.

6.3 Force sensor fabrication

The microfiber was fabricated by tapering a standard single-mode optical fiber. The fiber was fed into a heating filament and pulled from one end using a commercial glass-processing machine (Vytran's GPX-3400). The fabrication parameters for making the 30-μm fiber taper were as follows: pulling velocity = 1-mm/s, input power to filament =

29-W, feeding speed at pulling the waist = 57.6-μm/s, and taper and waist lengths are all 20-mm. The taper length of the microfiber was long enough to effectively re-couple only the fundamental mode back to the single mode fiber.

A bend-insensitive single-mode fiber (G.657B fiber from Silitec), which contains higher germanium concentration than standard single-mode fiber, was tapered down from 125-μm to 30-μm. In order to enhance its photosensitivity, the taper was hydrogen loaded at 25℃ for over 60 hours. Since the core (~2-μm diameter) was very small, the hydrogen diffused out rapidly [17], FBG inscription thus has to be made immediately after the microfiber was withdrawn from the hydrogen chamber.

The 5-mm long FBG was fabricated using standard phase mask technique with a 1061.5-nm pitch phase mask manufactured by Ibsen. A pulsed KrF excimer laser with wavelength of 248-nm was used as the writing bream. The pulse energy and pulse rate were 13-mJ and 200-Hz, respectively. The apodisation profile was realized by scanning the writing beam at the microfiber with a hamming profile at maximum velocity of 5-mm/s over 10 times. The corresponding inverse hamming profile for flattening the DC exposure of the grating was also used. During this process, the phase mask was taken out before scanning the writing beam to the grating again.

It is a challenge to directly transduce the contact force being sensed to compressive strain in the microfiber. When a certain amount of applied force is exceeded, the MFBG will bend or buckle [18]. The buckling condition is mainly determined by the diameter of the fiber and the compliance of the silicone rubber. The smaller the diameter, the easier it is to buckle. In order to avoid buckling, the MFBG's side-way movement must be restricted.

Silicone rubber (Rhodorsil RTV-573) inside a 0.3-mm thick stainless steel tube with a square cross-section of 2.4 mm x 2.4 mm was used to restrict the deformation of the microfiber in the axial direction for small contact force. Consequently, linear contact force-to-wavelength conversion in the MFBG can be obtained. Rhodorsil RTV-573 is a low viscosity liquid silicone that cured at room temperature by adding a curing agent to form a strong flexible silicone rubber. The liquid silicone with 2% weighted catalyst was first filled into a stainless steel mold. After 24-hour, the silicone rubber turned into a solid form. The MFBG was aligned in the center of the tube, with the aid of two fiber holders. The properties of the silicone rubber are tabulated in Table 6.1.

Table 6.1. The properties of Rhodorsil RTV-573

Properties	Value	Unit
Measured refractive index	1.415	
Base Viscosity	13,000	cps
Durometer	65	Shore OO
Tensile	247	psi
Elongation	262	%
Modulus@100%	63	

6.4 Characterisation

6.4.1 Force test

Figure 6.2 shows the experimental result of the wavelength shift as a function of contact force. The reflected wavelength was measured by an FBG interrogator with a resolution of 1-pm. It is clear that the wavelength shift against contact force was linear up to 0.65-N. Exceeding that amount of force, the sensor start to buckle. The sensitivity, maximum and minimum forces of this sensor measured in the linear region are -0.73-nm/N, 0.65-N and 1.37-mN, respectively. It was experimentally demonstrated that the sensor was fairly linear with R^2 of 0.99414.

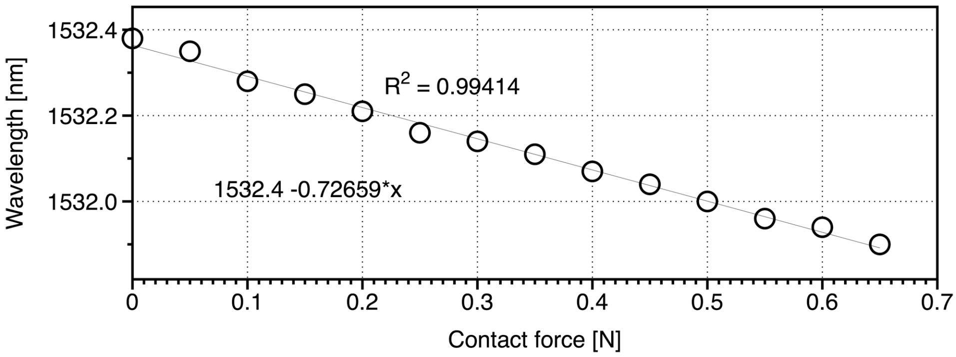

Fig. 6.2. Measured wavelength shift versus contact force of the MFBG force sensor. The solid black line shows the linear fit.

It should be noted that the 12-mm distance between the MFBG and the end of microfiber ensures a good balance of sensitivity and linearity. If the MFBG is located too close (far), the maximum contact force that can be measured in the linear range is smaller (larger) but the sensitivity is higher (lower). We found that 12-mm is an adequate separation for this particular application.

6.4.2 Reflection spectra investigation

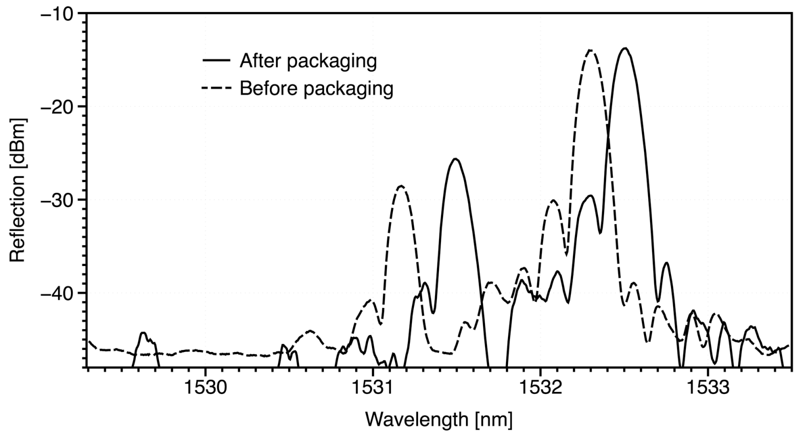

Fig. 6.3 The reflection spectra of the MFBG before and after packaging.

Figure 6.3 shows the reflection spectra of the MFBG before and after embedded into the silicone rubber. The grating spectrum was measured using another interrogator from Micron Optic, Inc. (model SM-125) with a resolution of 5-pm. The MFBG is an air-clad waveguide before packaging. Its reflection spectrum is therefore changed after packaged in Rhodorsil RTV-573 that has a refractive index of 1.415. The effective refractive index is thus larger after it is packaged and results in a spectral shift toward the longer wavelength. It was also observed that the reflected wavelength was broadened after it was embedded into silicone rubber. It implied that the grating experienced a differential strain profile along its length. This might be due to the formation of air bubbles during the de-gassing phase of the silicone rubber. However, the spectrum broadening does not affect the sensor's performance because peak wavelength detection technique was used.

The side peak located at shorter wavelength was a consequence that the LP02 excited by the MFBG was re-coupled to the core via the taper. The taper length (20-mm) was designed to couple most of the power of the modes other than LP01 into the cladding and eventually lost. The remaining reflection power from LP02 was slightly stronger after packaging because of the higher value of the refractive index of the silicone rubber. However, the reflection of this side peak is 90% less than that of the main peak. Therefore, the force sensor effectively reflects a single peak.

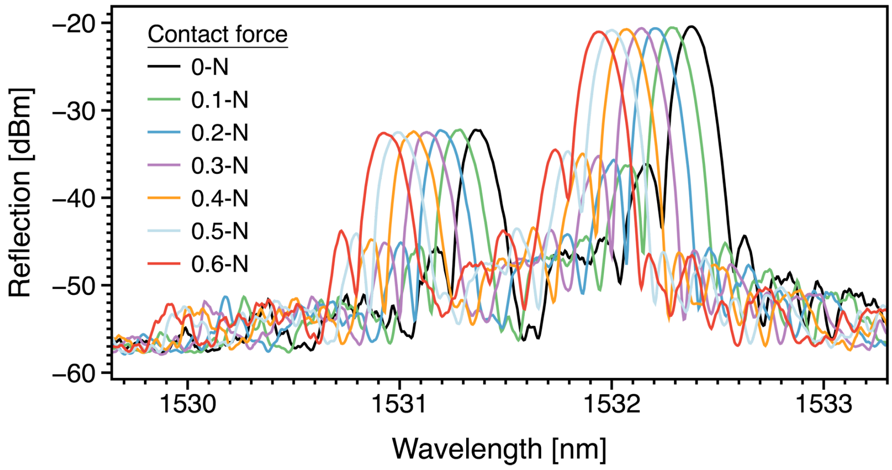

Fig. 6.4 Reflection spectra of the force sensor with different axial contact forces.

Figure 6.4 shows the reflection spectra of the force sensor with different contact forces. It is worth noting that the spectrum kept its shape even with larger applied forces. It was due to the contribution of the combination of the short grating length and the adequate separation between the MFBG and the contact point. These two design parameters minimize the differential strain field caused by the applied force along the grating.

6.4.3 Step Response

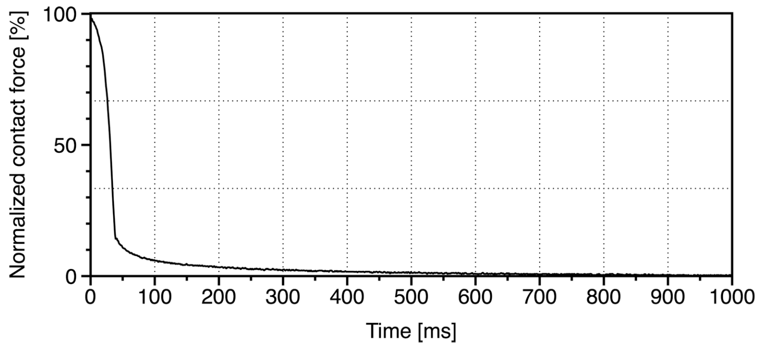

Fig. 6.5. The experimental result of step response.

To be capable of measuring contact forces in real time, the response time is crucial in most applications. The step response time was measured and shown in Fig. 6.5. A 0.6-N force was applied to the sensor and then released. The result shows that it took about 40-ms to recover over 80% and 600-ms for the sensor to be completely stabilized. In actual application, force sensors are required to continuously but gradually measure the contact force in real time. The response time of the sensor is sufficiently fast for the use in MIS devices.

6.5 Comparison to other force sensor specifications

The proposed force sensor is compact and has the favorable MIS features as listed in Table 6.2 which summarized the essential ideal force sensor specifications for catheters [12].

Table 6.2. Comparison of specifications

Characteristics	Targeted specifications [12]	FBGs based [13]	Our sensors
Working range	0-0.5 N	0-0.5 N	0-0.65 N
Sensitivity	High sensitivity to minimal touch	High sensitivity to minimal touch	High sensitivity to minimal touch
Resolution	0.005-0.01 N	0.01 N	0.00137 N
Linearity	Linear behavior	Linear behavior	Linear, with R^2 = 0.99646
Hysteresis	Low hysteresis	Low hysteresis	Low hysteresis
MRI compatibility	Essential	Yes	Yes
Size	<2.5-mm in diameter	2.3-mm in diameter	2.4x2.4-mm^2

It is worth noting that the working range of our sensor is slightly larger than the other two. The resolution of our sensor is about 7 times higher than that based on FBGs inscribed in standard fibers. Regarding the MRI compatibility, the microfiber is made of germanium-doped silica and therefore inherently is MRI compatible. The silicone rubber and the outer package are made of non-magnetized materials that are also MRI compatible. The size of the proposed packaged force sensor is 2.4-mm^2. With linear behavior and low hysteresis, our proposed force sensor is a promising device that meets the highly demanding requirements in catheter application.

6.6 Chapter Summary

A novel miniaturized high-performed force sensor based on a MFBG packaged in silicone rubber and stainless steel tube was experimentally demonstrated. Sensor fabrications and its operation principle were described. The spectra characteristics of the MFBG before and after packaged and under different applied forces were studied. The force sensitivity and response time of the sensor were measured. The performance of the proposed force sensor compares favorably with all reported force sensors and meets all the essential specifications of a force sensor for use in catheters.

References

[1] Z. Xiong, G. D. Peng, B. Wu, and P. L. Chu, "Highly tunable Bragg gratings in single-mode polymer optical fibers," *IEEE Photonics Technology Letters*, vol. 11, no. 3, pp. 352–354.

[2] G. D. Peng, Z. Xiong, and P. L. Chu, "Photosensitivity and Gratings in Dye-Doped Polymer Optical Fibers," *Optical Fiber Technology*, vol. 5, no. 2, pp. 242–251, 1999.

[3] Z. Xiong, G. D. Peng, B. Wu, and P. L. Chu, "Highly tunable Bragg gratings in single-mode polymer optical fibers," *IEEE Photonics Technology Letters*, vol. 11, no. 3, pp. 352–354.

[4] Y. Yu, H. Tam, W. Chung, and M. Demokan, "Fiber Bragg grating sensor for simultaneous measurement of displacement and temperature," *Optics Letters*, vol. 25, no. 16, pp. 1141–1143, 2000.

[5] Z. Weigang, D. Xiaoyi, Z. Qida, K. Guiyun, and Y. Shuzhong, "FBG-type sensor for simultaneous measurement of force (or displacement) and temperature based on bilateral cantilever beam," *IEEE Photonics Technology Letters*, vol. 13, no. 12, pp. 1340–1342, 2001.

[6] T. Guo et al., "Temperature-Insensitive Fiber Bragg Grating Force Sensor via a Bandwidth Modulation and Optical-Power Detection Technique," *Journal of Lightwave Technology*, vol. 24, no. 10, pp. 3797–3802, 2006.

[7] L. Hu, X. Dong, C. Zhao, S. Zhang, and S. Jin, "Temperature-insensitive Load Sensor with a single Fiber Bragg Grating," *Proc. of SPIE,* vol. 7853, p. 78532W, 2010.

[8] L. Xue, Q. Zhao, J. Liu, G. Huang, T. Guo, and X. Dong, "Force sensing with temperature self-compensated based on a loop thin-wall section beam," *IEEE Photonics Technology Letters,* vol. 18, no. 1, pp. 271–273, 2006.

[9] L.-Y. Shao, Q. Jiang, and J. Albert, "Fiber optic pressure sensing with conforming elastomers," *Applied Optics*, vol. 49, no. 35, pp. 6784–6788, 2010.

[10] K. Reck, E. V. Thomsen, and O. Hansen, "MEMS Bragg grating force sensor," *Optics Express*, vol. 19, no. 20, pp. 19190–19198, Jan. 2011.

[11] T. Guo, A. Ivanov, C. Chen, and J. Albert, "Temperature-independent tilted fiber grating vibration sensor based on cladding-core recoupling," *Optics Letters*, vol. 33, no. 9, pp. 1004–1006, 2008.

[12] P. Polygerinos, D. Zbyszewski, T. Schaeffter, R. Razavi, L. D. Seneviratne, and K. Althoefer, "MRI-Compatible Fiber-Optic Force Sensors for Catheterization Procedures," *IEEE Sensors Journal*, vol. 10, no. 10, pp. 1598–1608, Oct. 2010.

[13] K. Yokoyama et al., "Novel Contact Force Sensor Incorporated in Irrigated Radiofrequency Ablation Catheter Predicts Lesion Size and Incidence of Steam Pop and Thrombus," *Circulation-Arrhythmia and Electrophysiology*, vol. 1, no. 5, pp. 354–362, 2008.

[14] T. Wieduwilt, S. Brückner, and H. Bartelt, “High force measurement sensitivity with fiber Bragg gratings fabricated in uniform-waist fiber tapers,” *Measurement Science and Technology*, vol. 22, no. 7, p. 075201, May. 2011.

[15] Y. Zhang et al., “Refractive index sensing based on higher-order mode reflection of a microfiber Bragg grating,” *Optics Express*, vol. 18, no. 25, pp. 26345–26350, 2010.

[16] Y. Ran et al., “193nm excimer laser inscribed Bragg gratings in microfibers for refractive index sensing,” *Optics Express*, vol. 19, no. 19, pp. 18577–18583, Jan. 2011.

[17] M. L. V. Tse et al., “Observation of symmetrical reflection sidebands in a silica suspended-core fiber Bragg grating,” *Optics Express*, vol. 18, no. 16, pp. 17373–17381, Aug. 2010.

[18] N. Mohammad et al., “Analysis and development of a tunable fiber Bragg grating filter based on axial tension/compression,” *Journal of Lightwave Technology*, vol. 22, no. 8, pp. 2001–2013, Aug. 200

Chapter 7

Conclusion

7.1 Research summary

The fundamental theory and fabrication of fibre Bragg gratings (FBGs) have been reviewed. The research on the FBGs' theory, fabrication and applications have been going for many years. The grating devices have become critical elements in both telecommunication systems and optical sensing systems. Although FBGs have found enormous applications, advanced FBGs providing unique features would pave the way for applications that demand very high or sophiscated spectral specifications.

To fabricate advanced FBGs, two major aspects need to be enhanced. First, it is the grating profile design. We have proposed a highly flexible FBG fabrication technique that can fabricate FBGs with any apodisation and local phase. The key feature of the system is that the grating parameters including long grating lengths, apodisation profile and chirp rate can be controlled by employing linear translation stages, which provide accurate and reliable nano-scale motion. The principle, implementation, software design and experimental results were demonstrated.

Fibre gratings possess all the important characteristics of the optical fibre in which the grating is written. To advance the grating device, apart from exploiting the grating design, the using special fibre is another approach. FBG inscribed in microfibre is one of the best potential candidates for sensing applications. It is fabricated by tapering a standard optical fibre into micron scale waveguide. The taper consists the waist region and two transition regions. Microfibres exhibit many advantages, namely, (1) compact in size, (2) much higher sensitivity to tension/applied force due to the reduction in fibre diameter, (3) extremely flexible in bending, and (4) sensitive to ambient refractive index due to its evanescent field guiding characteristic. In this thesis, the fabrications of microfibre and microfibre Bragg grating (MFBG) have been reported. MFBG is an air-clad waveguide. For cladding diameters larger than one micron, the optical guiding typically become multi-mode which is undesirable in sensing applications. In other words, to take advantage of MFBGs, coupling from multi-mode to single-mode operation is necessary in practice. In our work, we demonstrated a simple technique that filters out the reflected higher order modes from the grating written in the microfibre via the linear taper region of an appropriate length. The principle, fabrication, and experimental results were presented. The single reflective mode MFBG was characterised for the sensitivity to the ambient refractive index, strain, temperature with and without packaged. The strain distribution of the taper was also analysed theoretically and experimentally. One of the main advantages of the MFBGs is that it is highly sensitive to the force applied to the grating. We proposed and demonstrated that the MFBG embedded in a package can be used as a force sensor for the use in minimally invasive surgery devices for catheterization procedures. The performance of the sensor was examined and compared to the ideal specifications of the application and one of the best commercial products in that field. The results revealed that the proposed sensor come out on top.

7.2 Difficulties

Many difficulties were encountered during the development of the advanced FBG fabrication system. One of them is the requirement of precise optical alignments. This difficulty of aligning optical components is proportional to the length of the overall optical path. The longest optical path in our system is over 2-m (measured from the laser to the optical fibre). With this long path, a slight misalignment of any optical component would result in the beams not to incident on the targeted fibre's core has a 9-μm diameter.

The most challenging adjustment of the optical alignments is the pair of cylindrical lenses. The focal length of the lenses is 270-mm. With this long focal length, the overall optical path is also lengthened. The use of such long focal length is to minimize the unwanted effect called spherical aberration, which would degrade the quality of the focusing beams. In addition to the long optical path, the angles of the lenses also need to be precisely aligned. In the configuration, the lenses are placed parallel to its optical axis (~13.2° normal to vertical axis) when the phase mask is positioned in the middle of the travel length of the Y-axis translation stage. It is very difficult to tune the lenses to the desired angle if it is not set in orthogonal to longitudinal axis of the optical fibre.. The long focal length, desired angular degree, typically ~13.2° normal to the targeted fibre, and the symmetric design are the main constraints to align the lenses.

Another difficulty found in the advanced FBG fabrication system was that the stability of the translation stage is affected by its input airflow rate. For writing a grating, typically longer than 50-mm, a manual adjustment to the airflow rate is needed. As a result, a longer time is needed for stabilizing the stage. To resolve this problem, the software is written to provide a feature that it is capable of sensing the current stability of the stage and then halt and wait for the user to fine-tune the airflow rate to continue the writing. This problem leads to the drawbacks that the fabrication system cannot be fully automatic and the total writing time is increased considerably.

Different challenges have been discussed. The problems aroused from the long optical path, the spherical aberration effect and non-orthogonal positioned cylindrical lenses, as well as the adjustment of airflow rate to translation stage have been reported. Future work is required to address the problems.

7.3 Future work

There are two main aspects will be addressed. The first is to resolve the problems found in developing the advanced fibre Bragg gratings fabrication system. The roots of the problems have been identified and discussed in previous subsection. To further improve the system, changes of configuration will be required. The future work for improving the system is summarized as follows:

1. Using a pair of aspheric lenses with shorter focal length, the overall optical path can be shortened and at the same time the spherical aberration can be minimized. Shortening the optical path can significantly increase the tolerance of the alignment and therefore make the alignment easier.
2. To align the lenses with desired angle and distance to the optical fibre, some tools are needed. Mechanical tools should be invented by getting more experience in handling the optics.
3. One of the factors affecting the performance of the air-bearing translation stage is the weight unbalance of the loads. Optimized performance can be achieved with the overall central gravity positioned at the centre of the platform. The weights of the components mounted on the platform will be analysed and additional weights will be added for balancing the stage.
4. Stability of the air-bearing translation stage is a key for the advanced FBG fabrication system. To achieve sufficient stability, airflow rate control is needed. Tuning the airflow rate manually is an inefficient approach. A programmable flow rate regular is able to be integrated into the system and make the whole system be fully automatic.

Apart from perfecting the fabrication system, some research directions have been identified but cannot be conducted due to insufficient time and unavailability of equipment. The arousing research projects for the future work are summarized as follows:

1. Microfibre Bragg gratings would have found more applications requiring high standard specifications. The work on exploiting this newly developed grating can be a promising research direction.
2. Sensing applications based on Microfibre Bragg gratings are still a new research direction. There are some potential applications, for example, accelerometers and curvature sensors.
3. The taper region of the MFBG is an important parameter that affects the reflected modes. Movements to the taper region would vary the power of modes re-coupled to the fiber. Using this characteristic, the MFBG is possible to detect the acceleration.
4. The re-coupled power is affected by the curvature of taper region. The curvature sensor based on MFBG could be realized.
5. The MFBG is sensitive to temperature. To be employed to other sensing applications, temperature is needed to be compensated. Using our proposed contact force sensor as an example, a scheme of temperature insensitive design can be implemented in such a way that an extra FBG is added in the 125-μm diameter region before the contact force sensor. The operation principle is that the MFBG and FBG are also sensitive to temperature and therefore demodulating the two peaks, the temperature effect can be compensated by referencing.

6. We have the advanced FBG fabrication system and microfibre fabrication technique. Combining both of them together, the characteristics of the newly high standard MFBG might have a large impact to the optical sensing field. In the literature, there are, up to date, no specially made grating written in the microfibre for applications.